

Four-dimensional magnetic resonance imaging-based system for radiotherapy of lung cancer

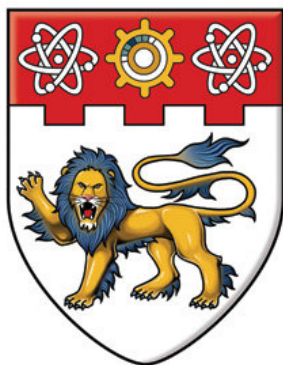
Yang, Yuxin

2014

Yang, Y. (2014). Four-dimensional magnetic resonance imaging-based system for radiotherapy of lung cancer. Doctoral thesis, Nanyang Technological University, Singapore.

<https://hdl.handle.net/10356/61606>

<https://doi.org/10.32657/10356/61606>



NANYANG
TECHNOLOGICAL
UNIVERSITY

**FOUR-DIMENSIONAL MAGNETIC
RESONANCE IMAGING-BASED
SYSTEM FOR RADIOTHERAPY OF
LUNG CANCER**

YANG YUXIN

SCHOOL OF CHEMICAL AND BIOMEDICAL
ENGINEERING

2014

FOUR-DIMENSIONAL MAGNETIC RESONANCE IMAGING-BASED SYSTEM FOR RADIOTHERAPY OF LUNG CANCER

YANG YUXIN

School of Chemical and Biomedical Engineering

A thesis submitted to the Nanyang Technological
University in fulfillment of the requirement for the degree
of Doctor of Philosophy

2014

Acknowledgement

This work was supported by Singapore National Medical Research Council (NMRC) under Grant NMRC/NIG/1033/2010.

This thesis would not have been possible without the support from many sides. First and foremost, I would like to express my sincerest gratitude to my supervisor, Assistant Professor Poh Chueh Loo, for his patience, enthusiasm, motivation, and enormous knowledge in this area. His continuous support helped me greatly in all the time of my Ph.D. study and research, and writing this thesis. His guidance has not only given me the knowledge in scientific area but also made me a better researcher and person, with patience, confidence, and responsibilities. I could not have imagined having a better supervisor and mentor for my Ph.D. study.

Besides my supervisor, I would like to thank Dr. Tan Cher Heng, Dr. Ivan Tham, and Dr. Teo Soo Kng for their cooperation, insightful advices, supports, and passion for this research work.

I am very grateful to my colleagues, Dr. Eric Van Reeth, Dr. Chuah Tong Kuan, Dr. Yu Peicong, Mr. Darwin Tay, Mr. Ho Jiahui, and Ms. Chilla Venkata Naga Geetha Soujanya, for the stimulating discussions, and for all the fun we have had together.

Special thanks go to Ms. Evelyn Quah and Ms. Yvonne Tay for their help on MR image acquisition. I would also like to thank Ms. Shi Xin Mei for her help on patient recruitment.

I would not forget the help from all the undergraduate students who worked with me: Mr. Bai Zhong Yang, Ms. Mary Stanislaws, Ms. Chuah Pei Jun, Ms. He Shuai, Ms. Samiksha Sultania, Ms. Hotchandani Ruchi, and Mr. Yu Yang. All of them have helped me in one way or another, such as stimulating my thinking and decreasing my workload.

I would also like to thank all my friends for their accompany and all the joys we had together.

Last but not least, I am very grateful to my family, especially my mother Mrs. Gao Ping and my father Mr. Yang Zhidong for raising me up and everything they have done for me. I would like to thank my aunts, Mrs. Gao Limin and Mrs. Gao Chuan, for their guidance and personal support. I would also like to thank my wonderful wife, Mrs. Fu Yuqing, for her endless supporting, encouraging, and bringing me much joy at difficult times.

Abstract

Lung cancer has been the most common and the most deadly cancer in the world for several decades. For current 3D-radiotherapy (RT) especially for lung cancer patients, respiration motion poses a major challenge. Consequently, four-dimensional (3D + time) RT, which involves the use of 4D imaging modalities, is developed to address this problem. The overall objective of this project is to significantly improve the efficiency and efficacy of RT. Currently, the 4D-RT planning of lung cancer is only based on 4D computed tomography (CT). However, 4D-CT involves high ionizing radiation and is only able to provide an averaged breathing cycle to study respiratory motion. As compared to 4D CT, magnetic resonance imaging (MRI) is able to produce images with excellent soft tissue contrast. In addition, there is no ionizing radiation involved during MRI scanning. Consequently, 4D-MRI is able to continuously scan in ‘real-time’ for several breathing cycles, which makes 4D-MRI able to cover individual changes in breathing. This thesis proposes the development of a novel 4D-MRI based system for 4D-RT of lung cancer patients as a complement of current 4D-CT based system. The specific aims of this thesis are (i) determining suitable 4D-MRI sequences for lung cancer imaging; (ii) developing automatic target structure delineation; and (iii) the fusion of 4D-MRI and 3D-CT for dose calculation.

Ten healthy subjects and six lung cancer patients were recruited and studied in this thesis. 4D-MRI sequence TWIST was found to be suitable for dynamic lung imaging as it showed good image quality at a faster temporal resolution, which is capable of showing the motion path of tumor. A novel automatic registration-based segmentation scheme was successfully developed which was shown to greatly reduce computation amount/time while maintaining good segmentation accuracy. To address the problem of ionizing radiation and dose calculation, a novel technique was developed to fuse 4D-MRI and 3D-CT to generate simulated 4D-CT datasets. The simulated 4D-CT images were shown to be accurate in terms of landmark positions.

In summary, the evaluation of 4D-MRI sequence, and the developed methods for target delineation of 4D datasets and fusion of temporal and spatial information from different modalities, provide a basis for the use of 4D-MRI as an alternative imaging modality to 4D-CT for 4D-RT of lung cancer patients.

TABLE OF CONTENTS

Acknowledgement	i
Abstract	iii
Statement of originality	xiv
Chapter 1	
Introduction	1
1.1 Background.....	1
1.1.1 Lung cancer	1
1.1.2 Radiotherapy	2
1.1.3 Medical image processing and radiotherapy	10
1.2 Motivation.....	13
1.3 Objectives	15
1.4 Organization of the thesis.....	18
Chapter 2	
Literature review	21
2.1 Chapter overview	21
2.2 The Lungs and Its Respiratory Motion.....	22
2.3 Lung cancer.....	26
2.4 4D imaging: continuous dynamic 3D images over time.....	27
2.4.1 Computed tomography	28
2.4.2 Magnetic resonance imaging	34
2.4.3 Comparison of 4D-CT and 4D-MRI	40
2.5 Automated segmentation of 4D medical images for RT planning	42
2.5.1 4D Segmentation.....	43
2.5.2 Registration-based segmentation	45
2.5.3 Deformable registration.....	48
Chapter 3	
Evaluation of 4D-MRI sequences at 3T for lung cancer imaging	55
3.1 Chapter overview	55
3.2 Comparison of 3D dynamic MR sequences at 3T for imaging of lung cancer	56
3.2.1 Materials and Methodology	58
3.2.2 Study results	67
3.2.3 Study discussion	76
3.2.4 Study conclusion.....	80
3.3 4D-imaging of lung cancer: comparison of 4D-MRI and 4D-CT based on tumor volume and motion	81

3.3.1	Materials and methodology	82
3.3.2	Study results	86
3.3.3	Study discussion	91
3.3.4	Study conclusion	92
3.4	Chapter discussion and summary	93
Chapter 4		
	Automated segmentation of multi-structures on 4D-MRI thoracic dataset	95
4.1	Chapter overview	95
4.2	Registration-based segmentation of 4D-MRI thoracic dataset	97
4.2.1	Materials and method	97
4.2.2	Study results	101
4.2.3	Study discussion	104
4.2.4	Study conclusion	105
4.3	Adapting registration-based segmentation for efficient segmentation of thoracic 4D-MRI	106
4.3.1	Materials and methodology	107
4.3.2	Study results and discussion	112
4.3.3	Study conclusion	113
4.4	A Spatio-temporal based scheme for efficient registration-based segmentation of thoracic 4D-MRI	117
4.4.1	Materials and methodology	121
4.4.2	Study results	129
4.4.3	Study discussion	135
4.4.4	Study conclusion	138
4.5	Chapter summary	139
Chapter 5		
	Fusion of 4D-MRI and static 3D-CT: creating simulated 4D-CT dataset	140
5.1	Chapter overview	140
5.2	Introduction	141
5.2.1	Motivation	141
5.2.2	Finite Element Method	144
5.3	Objective	148
5.4	Materials and methodology	149
5.4.1	Proposed scheme	149
5.4.2	Data	156
5.4.3	Evaluation	157
5.5	Results	160
5.6	Discussion	167

5.7	Conclusion	171
Chapter 6		
	Summary and future work	172
6.1	Chapter overview	172
6.2	Integration of the 4D-MRI based system for 4D-RT of lung cancer patients.....	173
6.3	Significance of this thesis	177
6.4	Future work	180
6.5	Thesis conclusion	182
	Bibliography	184

List of Figures and Tables

Chapter 1

Figure 1-1 Major steps involved in RT	2
Figure 1-2 An example of the target delineation of a tumor and other organs at risk (e.g. lungs, spinal cords, esophagus). The CTV and PTV are added to the GTV.....	4
Figure 1-3 The volume of the skin is close to the volume of the core of an orange (adapted from [16]). This is to illustrate that a small reduction (e.g. 5 mm) of the safety margin could decrease the PTV by half.	6
Figure 1-4 Comparison between the workflow of 3D-RT (left) and 4D-RT (right)	8
Figure 1-5 A linear accelerator that incorporates on-board imaging devices. A kilovoltage X-ray source and a flatpanel imaging device is used for cone-beam CT acquisition. A flat-panel megavoltage imaging device that is opposite the radiation beam enables real-time imaging during treatment [24]. (Permission to reproduce has been granted by the American Association of Physicists in Medicine)	9
Figure 1-6 Comparison of thoracic image of MRI (left) and CT (right) of the same lung cancer patient. The image of MRI has better soft tissue contrast, given the fact that the window /level of the CT image is already adjusted for better visualization of soft tissue..	15
Figure 1-7 The scheme of the proposed 4D-MRI based system for 4D-RT of lung cancer. The words in various chapters are included.	19

Chapter 2

Figure 2-1 The anatomy of the lung, the bronchi tree, and the alveolar sacs [60] (permission to reproduce is granted by Wikimedia Commons.).....	24
Figure 2-2 Illustrations of the movement of the diaphragm and the rib cage during breathing [61]. (Copyright(C) 2013 Yuxin Yang. Permission is granted to copy, distribute and/or modify this document under the terms of the GNU Free Documentation License, Version 1.3or any later version published by the Free Software Foundation.).....	25
Figure 2-3 Measured position of diaphragm in fluoroscopic images (triangles) and mathematical fitted model (solid line) [59]. (Permission to reproduce is granted by American Association of Physicists in Medicine.).....	25
Figure 2-4 Generating a series of 1D projections of a 2D axial cross-sectional CT image with a fan-beam X-ray tube.....	29
Figure 2-5 Iso-surface renderings of a spherical object scanned by 3D-CT (top) and 4D-CT (bottom) at different positions of the motion cycle. Three dimensional CT showed a severe motion artifact, and the artifact changed at different positions of the motion cycle [68]. (Permission to reproduce has been granted by the American Association of Physicists in Medicine.)	30
Figure 2-6 An example of a 4D-CT scanner (Brilliance CT Big Bore, Philips, Eindhoven, The Netherlands). This 4D-CT scanner was used to acquire the 4D-CT dataset of patients who were studied in this thesis.	31

Figure 2-7 Retrospective acquisition of 4D-CT dataset. Two-dimensional slices are continuously imaged from all respiratory phases and are then sorted into appropriate phases to form corresponding individual 3D images based on the respiratory signal.....	32
Figure 2-8 A respiratory belt senses the abdomen movement to generate a respiratory signal ...	33
Figure 2-9 Illustration of MRI sequences (a) spin-echo and (b) gradient-echo	36
Figure 2-10 An example of the 3T MRI scanner (Siemens Trio MRI scanner, Siemens Healthcare, Erlangen, Germany). This scanner was used in the studies presented in this thesis.	37
Figure 2-11 Severe motion artifact at the dome of the diaphragm (white arrow) due to irregular breathing during 4D-CT acquisition.....	41
Figure 2-12 An illustration of the overall basic registration-based segmentation scheme.....	47
Figure 2-13 Registration framework showing the key steps in registration.....	48
Table 2-1 4D-MRI sequences for lung imaging that has been applied in the literature.....	39
Table 2-2 Comparison of 4D-CT and 4D-MRI.....	41

Chapter 3

Figure 3-1 Tumor location of each patient. Tumors are marked with yellow circles. Patient 6 is with scoliosis.	61
Figure 3-2 Positions that evaluation of edge sharpness took places for different structures of interests (indicated by yellow lines). Structures of interests include tumor, heart, liver, chest wall, and lungs.	64
Figure 3-3 Examples of positions that local tissue contrast measurements took places for different organs: (a) chest wall-to-liver; (b) tumor-to-lung	65
Figure 3-4 Segmented images of tumor during breathing including all the phases are added to form the combined segmented image. Dashed circle in the illustration on the left shows all the tumor position and the grey area presents the accumulated tumor volume.	67
Figure 3-5 4D-MRI lung imaging of normal subject (upper row) and lung cancer patient (lower row) using three different sequences: TWIST, FLASH 3D, and VIBE. VIBE was not acquired for the patients to reduce scan time.....	69
Figure 3-6 Diaphragm dome trajectory of left and right lungs presented by TWIST, FLASH 3D (FL3D in short), and VIBE in CC direction of four healthy subjects.	72
Figure 3-7 Diaphragm dome trajectory of left and right lungs presented by TWIST, FLASH 3D (FL3D in short), and VIBE in CC direction of six lung cancer patients. VIBE was not acquired for the patients to reduce scan time.....	73
Figure 3-8 Tumor trajectory presented by FLASH 3D and TWIST in CC direction of six lung cancer patients.....	74
Figure 3-9 k-space is divided into two sectors: the central sector (A) and the peripheral sector (B).	79

Figure 3-10 Conventionally, the temporal resolution is A+B. Keyhole technique improves the temporal resolution by sampling B half as frequently thus the improved temporal resolution is A+B/2.	79
Figure 3-11 Illustration of the measurement of lung height using 4D-CT images. The lung height is measured from the apex of the lung to the diaphragmatic dome in CC direction in the coronal slice that crosses the trachea.	84
Figure 3-12 Illustration of sorting a 4D-MRI volume into corresponding breathing phase.....	85
Figure 3-13 Sample images of 4D-MRI and 4D-CT of 6 patients.....	87
Figure 3-14 Comparison of tumor trajectories in CC direction between sorted 4D-MRI volumes and 4D-CT volumes over one breathing cycle.	90
Table 3-1 Sequence parameters for 3D dynamic lung MRI.....	59
Table 3-2 Criteria for visualization of structures of interest	62
Table 3-3 Criteria for delineation of anatomical structures.....	63
Table 3-4 Qualitative ranking (mean/mode)	68
Table 3-5 Edge width (mm/pixels) measurements.....	69
Table 3-6 Local tissue contrast measurements	70
Table 3-7 Accumulated left lung volume of four healthy subjects and six lung cancer patients over 3 to 5 breathing cycles. V_{TWIST} , V_{FLASH} , and V_{VIBE} represent the accumulated volume for TWIST, FLASH 3D, and VIBE respectively. The unit for all the volumes is mL. ΔV_{FLASH} and ΔV_{VIBE} are calculated as $V_{TWIST} - V_{FLASH}$ and $V_{TWIST} - V_{VIBE}$ respectively. $\% \Delta V_{FLASH}$ and $\% \Delta V_{VIBE}$ are calculated as $\Delta V_{FLASH} / V_{TWIST}$ and $\Delta V_{VIBE} / V_{TWIST}$ respectively.....	75
Table 3-8 Accumulated right lung volume of four healthy subjects and six lung cancer patients over 3 to 5 breathing cycles.	75
Table 3-9 Accumulated tumor volume of six lung cancer patients over 3 to 6 breathing cycles. .	76
Table 3-10 Specifications of the 4D-CT dataset for each patient.....	82
Table 3-11 Tumor volumes of sorted MRI volume and 4D-CT volume at maximum exhalation phase of six lung cancer patients. V_{ME}^{CT} and V_{ME}^{MRI} represent the tumor volume for CT and MRI respectively. ΔV_{ME}^{MRI-CT} is calculated as $V_{ME}^{MRI} - V_{ME}^{CT}$. $\% \Delta V_{ME}^{MRI-CT}$ is calculated as $\Delta V_{ME}^{MRI-CT} / V_{ME}^{CT}$. Negative value means MRI has underestimated the tumor volume.....	88
Table 3-12 Accumulated tumor volumes of sorted MRI volumes and 4D-CT volumes over one breathing cycle. V_{Acc}^{CT} and V_{Acc}^{MRI} represent the accumulated tumor volume for CT and MRI respectively. ΔV_{Acc}^{MRI-CT} is calculated as $V_{Acc}^{MRI} - V_{Acc}^{CT}$. $\% \Delta V_{Acc}^{MRI-CT}$ is calculated as $\Delta V_{Acc}^{MRI-CT} / V_{Acc}^{CT}$. Negative value means MRI has underestimated the accumulated tumor volume.....	88
Table 3-13 Tumor motion coverage of sorted MRI volumes and 4D-CT volumes in CC direction over one breathing cycle. S^{CT} and S^{MRI} represent the tumor moving range for CT and MRI respectively. ΔS^{MRI-CT} is calculated as $S^{MRI} - S^{CT}$. $\% \Delta S^{MRI-CT}$ is calculated as $\Delta S^{MRI-CT} / S^{CT}$. Negative value means MRI has underestimated the tumor motion coverage.	89

Table 3-14 Equivalent sequences used by different manufactures	94
--	----

Chapter 4

Figure 4-1 Schematic of the registration based segmentation method. Inputs to the scheme are: the reference volume (v_{ref}), the target volumes (v_t), and the template (m). Intermediate results are the transformation warping ($\mathbf{r}(v_{ref} \rightarrow v_t)$). The output of the scheme is the deformed binary segmentations of the target scans (m_t).	99
Figure 4-2 Coronal slices of (a) original volumes: reference volume and target volume 1 and 2; (b) registered reference volume corresponding to target volume 1 and 2; (c) Manual segmentation of reference volume and automated segmentations of target volume 1 and 2; (d) volumes with segmented contours.	103
Figure 4-3 Three-dimensional model and volume calculated for reference volume, target volume 1, target volume 2, and target volume 3.	104
Figure 4-4 Generation of 2DST image	108
Figure 4-5 Sample plot of DSC and tolerance number against the iterations	112
Figure 4-6 Samples of automatically segmented images of Patient 1 and Patient 2. Contours in red: left lung; Contours in green: right lung; Contours in blue: tumor; Contours in yellow: ground truth.	113
Figure 4-7 Plots of optimal tolerance number against (a) relative diaphragm displacement; (b) cross-correlation; (c) sum of squared difference; and (d) mutual information for demons registration.....	115
Figure 4-8 Plots of optimal tolerance number against (a) relative diaphragm displacement; (b) cross-correlation; (c) sum of squared difference; and (d) mutual information for B-spline registration.....	116
Figure 4-9 Different registration strategies: (a) Registrations are performed from the reference volume (v_{ref}) to every other target volume; (b) Registrations are performed sequentially between adjacent volumes; (c) Similar volumes are grouped into N sets s^i . The reference volume (v_{ref}) is registered to each representative v_{med}^i of volume set s^i and to each volume within the reference set s^{ref} . Each representative v_{med}^i is registered to each volume with the corresponding volume set s^i	119
Figure 4-10 Basic registration-based-segmentation scheme.....	120
Figure 4-11 Overall illustration of proposed scheme.....	122
Figure 4-12 Detailed steps of grouping similar volumes based on relative diaphragm position.	125
Figure 4-13 Representative sample segmented images using proposed scheme. (a) 2D slices and corresponding 3D models. Contours in red: left lung; Contours in green: right lung; Contours in blue: tumor; Contours in yellow: ground truth. (b) Representative sample 3D models constructed by automated segmented images of Patient 1 showing the movement of lungs and tumor over time.	131

Figure 4-14 Accuracy results (average Dice's coefficient) of target structure segmentations for schemes using (a) demons registration and (b) B-spline registration.....	132
Figure 4-15 Percentage reduction of computation amounts (addition and multiplication) between proposed scheme and basic scheme (both cases) using demons registration and B-spline registration	133
Figure 4-16 Plot of maximum diaphragm displacement of each subject against the reduction of total computation amount for proposed scheme using (a) demons registration and (b) B-spline registration	134
Table 4-1 Evaluation Results of Automated Segmentation.....	103

Chapter 5

Figure 5-1 Typical simple finite elements defined for one-, two-, and three-dimensional problems. The elements showed here are low-order ones with nodal points only located at corners. For high-order finite elements, there are intermediate nodal points along edges.....	146
Figure 5-2 Overall scheme of proposed FEM approach to simulate 4D-CT volumes using static 3D-CT volume and 4D-MRI volumes.....	150
Figure 5-3 An example of the initial lung surface mesh and the smooth and decimated mesh after processing	154
Figure 5-4 An example of the landmark points selected in the right lung of one patient. Landmarks are projected onto a single maximum intensity image for visualization. The landmarks are selected to be evenly distributed throughout the whole lung.....	158
Figure 5-5 Overall scheme of simulating 4D-CT volumes using the displacement fields from registration directly. This is to benchmark the accuracy of the proposed FEM approach.	159
Figure 5-6 A comparison between the ground truth volume and simulated volumes deformed from the reference volume (v_{ref}) with the FEM method (v_{FEM}) and with the displacement fields generated from registration (v_{Reg}) of two patients. The window and level of the images are adjusted to enhance the visualization of small structures inside the lungs. The visible differences are marked by white arrows.	161
Figure 5-7 A comparison between the displacement fields generated by FEM and registration approaches. Magnitude of the displacements is color-coded: blue: small displacement; red: large displacement up to 15 mm.	162
Figure 5-8 An example of a landmark in ground truth (white), CT volume simulated by proposed FEM approach (red), and CT volume simulated by directly applying displacement field generated from registration between MRI volumes (blue).....	163
Table 5-1 Magnitude of the landmark displacement from v_{CT}^{ref} to v_{CT}^t ($\ P\ $), and simulation errors using FEM approach ($\ E_{FEM}\ $) and registration method ($\ E_{Reg}\ $) for v_{CT}^t at EI/EE. Values are averaged over all the landmarks with standard deviation shown in bracket.	163

Table 5-2 Magnitude of the landmark displacement from v_{CT}^{ref} to v_{CT}^t ($\ P\ $), and simulation errors using FEM approach ($\ E_{FEM}\ $) and registration method ($\ E_{Reg}\ $) for v_{CT}^t at MI/ME. Values are averaged over all the landmarks with standard deviation shown in bracket.	164
Table 5-3 Simulation errors using FEM approach at EI/EE in difference directions. Values are averaged over all the landmarks with standard deviation shown in bracket. Negative values of error in CC, RL, and AP direction mean the motion overestimation for the FEM approach in caudal direction, anterior direction, and leftwards respectively.....	165
Table 5-4 Simulation errors using FEM approach at MI/ME in difference directions. Values are averaged over all the landmarks with standard deviation shown in bracket. Negative values of error in CC, RL, and AP direction mean the motion overestimation for the FEM approach in caudal direction, anterior direction, and leftwards respectively.....	165
Table 5-5 Simulation errors using FEM approach for lungs with and without tumor for target volumes at EI/EE. Values are averaged over landmarks in different regions with standard deviation shown in bracket.	166
Table 5-6 Simulation errors using FEM approach for lungs with and without tumor for target volumes at MI/ME. Values are averaged over landmarks in different regions with standard deviation shown in bracket.	167

Chapter 6

Figure 6-1 Overall schematic of the 4D-MRI based system proposed in this thesis	175
---	-----

Statement of originality

This thesis is fully based on the author's original work. All the works from others were properly cited and acknowledged. Part of this thesis has resulted in original publications including peer-reviewed journals and proceedings.

Published journal article

Y. Yang, E. Van Reeth, C.L. Poh, C.H. Tan, and I. W.K. Tham. 'A spatio-temporal based scheme for efficient registration-based segmentation of thoracic 4D MRI' *Biomedical and Health Informatics, IEEE Journal of*, 2013

Published conference proceedings

Y. Yang, C.H. Tan, C.L. Poh. 'Visualization of lung using 4D magnetic resonance imaging.' *Proceedings of the 1st International Symposium on Bioengineering (ISOB 2011)*. pp. 49-55. 2011.

Y. Yang, E. Van Reeth, and C.L. Poh. ‘Adapting registration-based-segmentation for efficient segmentation of thoracic 4D MRI.’ *Computational Intelligence in Healthcare and e-health (CICARE), 2013 IEEE Symposium on*. pp. 42-45. IEEE, 2013.

S.-K. Teo, **Y. Yang**, E. Van Reeth, S. He, P. Chua, and C.L. Poh. ‘Tracking of tumor motion in lung cancer using patient specific finite element modeling and 4d-mri image data." *Biomedical Engineering (BioMed 2013)*. 2013

Submitted journal article

Y. Yang, S.-K. Teo, E. Van Reeth, C.H. Tan, I.W.K. Tham, and C.L. Poh, ‘A hybrid approach for fusing 4D-MRI temporal information with 3D-CT for the visualization of lung and lung tumor motion.’ *Biomedical and Health Informatics, IEEE Journal of*

Chapter 1 Introduction

1.1 Background

1.1.1 Lung cancer

Cancer is a worldwide killer. According to statistics from the International Agency for Research on Cancer (IARC), nearly 12.7 million new cancer cases and 7.6 million cancer deaths occurred worldwide in 2008. Among the numerous kinds of cancer that exist, lung cancer has been the most common and most deadly cancer in the world for several decades. About 1.61 million new cases occurred in 2008, representing 12.7% of all new cancers, with 1.38 million deaths (18.2% of the total) [1]. Most lung cancer patients are diagnosed when they have symptoms such as coughing, breathing changes, and pain in the chest. Instruments such as a chest radiograph need to be used in order to determine whether one has lung cancer. Once cancer is confirmed, surgery may be performed if the tumor is in its early stages; the purpose of the surgery is to remove a part of or the entire lobe of the lung where the tumor is located [2]. When surgery is not appropriate for a patient, radiotherapy (RT) and chemotherapy are the usual treatment methods. These treatment methods are

also usually executed following surgery so as to ensure the complete removal of cancerous cells. The focus of this thesis is on RT for lung cancer patients.

1.1.2 Radiotherapy

Radiotherapy (RT) is one of the most important and standard methods of cancer treatment. It uses high-energy ionizing radiation to destroy the deoxyribonucleic acid (DNA) of cancer cells, causing them to die or to reproduce more slowly. A typical RT process involves five major steps: image acquisition, target delineation, therapy planning, treatment delivery, and follow-up (Figure 1-1).

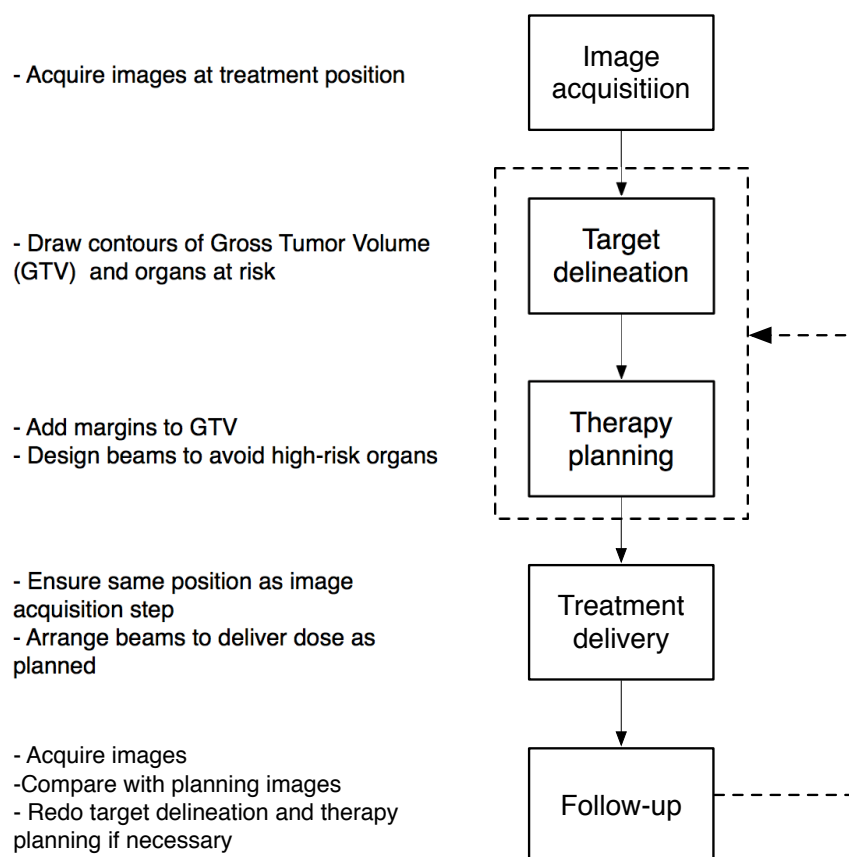


Figure 1-1 Major steps involved in RT

Conventional RT first acquires images of a patient that show three-dimensional (3D) anatomic structures. This involves placing the patient in the treatment position that provides the best access to the area requiring treatment. An immobilization device, such as a mold or mask, may be used to help the patient to maintain his/her same position during the treatment. For target delineation, the gross tumor volumes (GTV) and the organs that are at risk are defined in three dimensions by drawing contours on the 3D images acquired during the first step. This is generally performed in a slice-by-slice manner. In order to include regions of subclinical tumor spread adjacent and other locations of suspected tumor manifestations, a margin is added to the GTV to form the clinical target volume (CTV) [3]. Finally, using the CTV, the planning target volume (PTV) is defined. This involves the addition of the internal margin and the setup of the uncertainty margin to account for intra-fractional and inter-fractional patient motion. An example of GTV, CTV, PTV, and organs at risk delineated is shown in Figure 1-2. During treatment planning, the PTV together with the prescribed target dose and dose restrictions for the risk organs are used to find the treatment beams' optimal treatment angles and positions. Based on the patient's anatomy and individual treatment plan, the calculation of the amount of radiation is then performed in order to reach the prescribed dose [4]. The radiation beams have to be planned carefully in order to avoid high-risk organs. Once treatment planning is completed, the next step is treatment delivery. The treatment session is painless and non-invasive. The patient is placed in the linear accelerator coordinate system in the same position chosen during the image acquisition step, using the same immobilization system. A custom-tailored 3D radiation dose is achieved using different beam directions as defined during treatment planning. Based on the tumor's size and location, the patient's overall health condition, and other

medical treatments that the patient has received, 20 to 40 RT treatments may be arranged for the patient over a period of 4 to 8 weeks. During the RT period, if significant changes such as significant weight loss occur in the patient, which causes the initial planning to be inaccurate, re-planning might be necessary. Following the entire RT session, follow-up checks are executed regularly in order to evaluate the treatment. Patient images are acquired and studied. A set of criteria (Response Evaluation Criteria in Solid Tumors (RECIST) [5]) is used to evaluate patients' response to treatment.

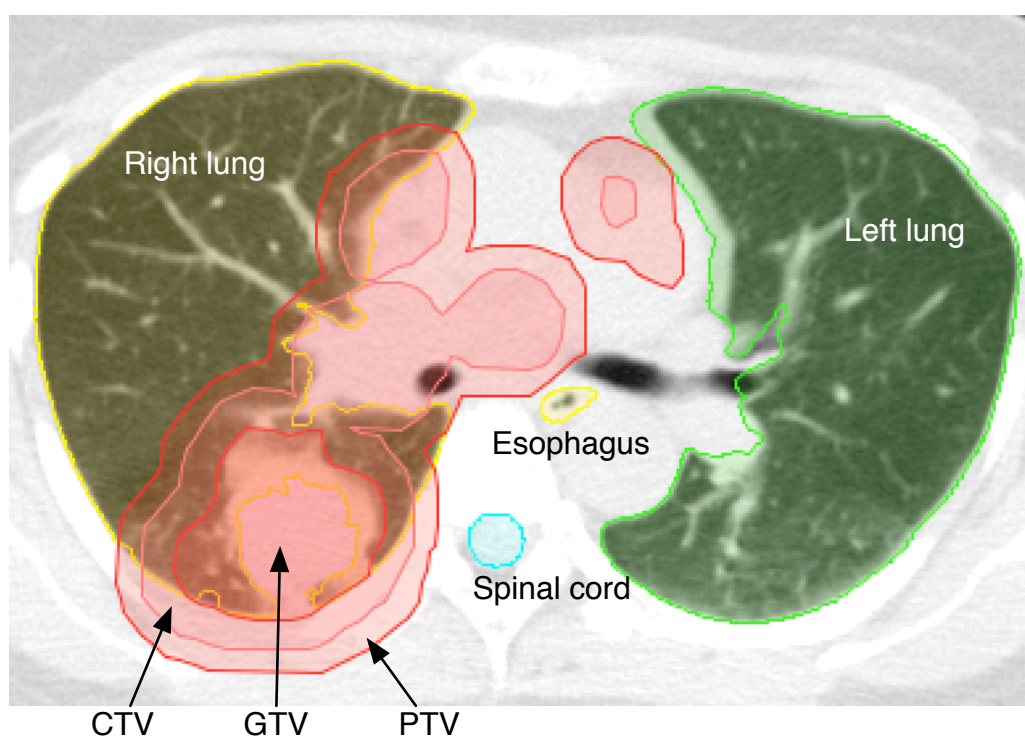


Figure 1-2 An example of the target delineation of a tumor and other organs at risk (e.g. lungs, spinal cords, esophagus). The CTV and PTV are added to the GTV.

RT's greatest challenge is to achieve the highest probability of a cure while simultaneously decreasing the morbidity rate [6]. A major problem that RT management faces today is the error that occurs as a result of internal organ motion, which can occur either inter-fractionally or intra-fractionally [7].

Inter-fractional motion is said to occur when the CTV changes daily due to the changes in the tumor size or changes in the patient's weight. This motion can be corrected with bony anatomy and/or internal fiducial markers used to align the patient. On the other hand, intra-fractional motion occurs during the irradiation process itself. Respiration-induced motion is the most common cause of this type of motion and can lead to large errors during RT, especially for lung cancer patients. The motion amplitude of lung tumors has been found to potentially be larger than 1.0 cm for those located in the lower lobes [8].

In order to overcome the problem stemming from respiration-induced motion, the breath-hold technique has been commonly used [9]. However, it is difficult for a patient to maintain the same breathing position. It can also be uncomfortable and difficult for a lung cancer patient with poor lung function to hold his/her breath for a long time. Another way to overcome the problem would be to add geometric margins that are usually population-based or experience-based [10]. Such margins are generally not patient-specific. It has been reported that lung tumor mobility cannot be reliably predicted based only on tumor locations [11]. As a result, normal tissues near the tumor are included in the PTV and are exposed to high radiation during treatment delivery. Increasing the average lung dose would result in increasing lung complications [12]. The sizes of these margins are critical when the tumor is located near high-risk organs, such as the spinal cord, heart, or kidneys [7, 13-15]. Restricted by the dose allowed for normal tissues, the RT dose that is necessary for controlling a tumor is often not delivered [16]. Studies have shown that higher tumor doses result in a survival advantage for lung cancer patients [17-19]. This problem can be tackled by reducing the safety margin that tightly matches the tumor so that less normal tissues are included in the PTV. If we consider a

tumor to be the core of an orange and the safety margin to be the skin of the orange, one can see that even if the orange skin is not thick, the volume of the skin almost equals the volume of the core of the orange (Figure 1-3) [16]. This is because the volume of a sphere is the third-power related to its radius ($V = \frac{4}{3}\pi r^3$). Consider a PTV that is a sphere and that has a radius of 25 mm; the volume of this PTV is 65.4 ml. A small reduction of 5 mm in the safety margin would reduce the PTV volume by more than a half, to a high value of 33.5 ml. The smaller PTV precisely does cover tumor creation geometry that would enable higher tumor doses to be applied.



Figure 1-3 The volume of the skin is close to the volume of the core of an orange (adapted from [16]). This is to illustrate that a small reduction (e.g. 5 mm) of the safety margin could decrease the PTV by half.

Accurate measurement and quantification of the tumor motion is the key to reducing the PTV for lung tumor. With fast acquisition of high resolution and multi-dimensional image data, advances in four-dimensional, or 4D (3D + time), medical imaging technology (e.g. computed tomography [CT], medical

resonance imaging [MRI]) have allowed patients to breathe during image acquisition in which the tumor drift during a typical respiratory cycle is captured. Recent studies have shown that a lung tumor not only shifts in positions but also deforms and rotates during normal respiration [20, 21]. Only using 4D imaging techniques, such as tumor movement and deformation during respiration, can be visualized and quantified, as 4D imaging not only captures the 3D anatomy but also the 3D evolution of organs and tumors overtime. Three-dimensional static imaging or two-dimensional (2D) dynamic imaging methods cannot provide such information.

Based on the tumor geometry and motion information that 4D imaging provides, the relationship between tumor motion and the respiratory cycle for an individual patient can be studied. Further, the development of image-guided radiotherapy (IGRT) allows for frequent imaging in the treatment room so that the tumor position can be monitored during the delivery of radiation, and treatment decisions can be made on the basis of these images [16]. Thus, four-dimensional radiotherapy (4D-RT) becomes possible. According to the definition from *Keall et al.* [22], 4D-RT is “*the explicit inclusion of the temporal changes in anatomy during the imaging, planning and delivery of radiotherapy,*” which indicates that the 3D geometry evolution of organs and tumors over time should be integrated into every step of 3D-RT.

As shown in Figure 1-4, fundamentally, the major workflow of 4D-RT is the same as that of conventional 3D-RT: image acquisition, target delineation, treatment planning, treatment delivery, and follow-up. However, the process of 4D-RT is much more complicated detail-wise. Image acquisition is more complex, as a sequence of 3D scans is now required over time. Audio- or visual-guided breathing during patient image acquisition is generally used to

ensure a regular and reproducible breathing pattern for further treatment delivery [23].

3D-RT	4D-RT
Image acquisition <ul style="list-style-type: none"> - Single 3D scan - Breath-hold / gated 	Image acquisition <ul style="list-style-type: none"> - 4D scan - Free breathing under respiratory guidance
Target delineation <ul style="list-style-type: none"> - Slice-by-slice delineation of single 3D scan 	Target delineation <ul style="list-style-type: none"> - Slice-by-slice delineation of every 3D scans of entire 4D dataset
Treatment planning <ul style="list-style-type: none"> - Standard population based planning margins to compensate tumor motion (may excessive or inadequate for individual patients) - Dose prescription/constraints based on single position 	Treatment planning <ul style="list-style-type: none"> - Individualised margins based on motion of tumor - Dose prescription/constraints based on multiple positions
Treatment delivery <ul style="list-style-type: none"> - Setup using skin marks - Stationary beams - Require patients to hold breath 	Treatment delivery <ul style="list-style-type: none"> - Image guided positioning of patients - Real-time monitoring of patient position using on-board imaging device - Continuous delivery of the designed 4D treatment plan throughout the entire breathing cycle or gating the beam to turn on/off at certain respiratory phases
Follow-up <ul style="list-style-type: none"> - 3D scan - Compare the geometry of tumor with the planning 3D image 	Follow-up <ul style="list-style-type: none"> - 4D scan - Compare not only the geometry but also the motion pattern of the tumor with the planning 4D image

Figure 1-4 Comparison between the workflow of 3D-RT (left) and 4D-RT (right)

For target delineation and treatment planning in 4D-RT, because at least 10 times more image data are to be dealt with, a significantly greater workload is introduced. Segmentation, dose calculation, and beam planning need to be done for each phase of breathing cycles. Currently, RT planning using 4D images considers the tumor and other organs' positions at all phases between maximum inhalation and exhalation. All of the positions are combined to include all tumor and organ motion [24].

Before treatment delivery, the on-board imaging device, such as cone-beam CT (Figure 1-5) used in IGRT, allows for better positioning of the patient by comparing the on-board images with planning images. Also, thanks to on-board imaging, the patient and tumor position can be monitored in real-time. Thus, by adapting planning from 4D images to on-board images, it is possible to either track the motion of the target tumor with the beam or to gate the beam to turn on/off at certain respiratory phases at the linear accelerator in the treatment delivery system [25].

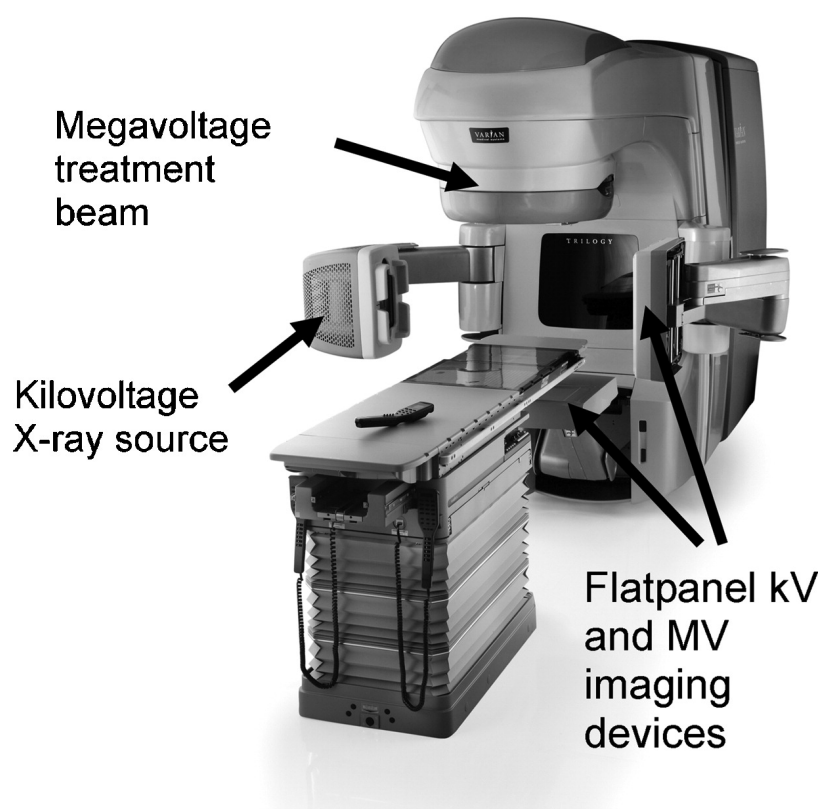


Figure 1-5 A linear accelerator that incorporates on-board imaging devices. A kilovoltage X-ray source and a flatpanel imaging device is used for cone-beam CT acquisition. A flat-panel megavoltage imaging device that is opposite the radiation beam enables real-time imaging during treatment [24]. (Permission to reproduce has been granted by the American Association of Physicists in Medicine)

For follow-up, 4D scans have to be performed to check whether any changes exist in not only the geometry but also the moving pattern of the tumor. Target delineation and therapy planning have to be re-done if the changes are large, which will render the initial plan inaccurate.

Advanced RT techniques, such as intensity-modulated radiotherapy (IMRT) and Cyberknife, can be combined with 4D-RT to further improve treatment. The IMRT technique varies intensities across the radiation beam to produce sharp dose gradients at the transition between the tumor and adjacent normal tissues. As a result, an increased radiation dose can be applied to the tumor without increasing the irradiation of nearby normal tissues [3, 26]. The Cyberknife approach mounts the linear accelerator on a robotic arm with six degrees of freedom, thus enabling the radiation beam to be positioned according to the on-board images. Hence, real-time RT delivery that corrects tumor motion can be achieved [27].

1.1.3 Medical image processing and radiotherapy

Today, image processing impacts almost every area and plays an important role in our daily life. As previously discussed in Section 1.1.2, medical images are the basis of the entire RT process. Clearly, advances in image processing can greatly improve RT in many areas.

Medical imaging's main goal can be considered the clear visualization of specific organs or structures inside the human body. To this purpose, many efforts have been made to enhance the quality of medical images. For example, algorithms have been developed to remove noise without changing or losing

valuable clinical information [28, 29]. Super resolution techniques [30, 31] have been employed to improve the images' spatial resolution. Also, a number of algorithms are used in an effort to improve the contrast of medical images [32-34]. These processes are often referred to as the pre-processing of the images.

Image segmentation is another fundamental technique in image processing. Image segmentation technique separates an image into different regions with respect to some characteristic such as gray tone or texture [35]. With the development of medical imaging, the delineation of anatomical structures and other regions of interest in an automated and accurate manner using computer algorithms is becoming increasingly important in assisting with numerous clinical applications, such as the quantification of tissue volumes, the study of anatomical structure, target delineation in RT, and computer-integrated surgery [36]. Automated segmentation improves reproducibility and helps to reduce the workload. Many types of segmentation techniques exist, ranging from simple ones, such as thresholding, to more advanced methods, such as deformable models [37-39]. For a detailed review on image segmentation of the 4D dataset, one can refer to Section 2.5.1.

Image registration is also a fundamental image processing technique that aims to align two or more images—for example, at different times, from different sensors, or from different viewpoints [40]. This technique is very useful when aligning on-board images in the treatment room with the planning images in the RT process so that the treatment planning can be adapted based on the patient's treatment position and movement.

Another interesting application of image registration is the fusion of multiple image modalities [41]. A variety of medical imaging modalities have been developed based on different energy sources and focus on different aspects of diseases. For example, CT and MRI primarily focus on the anatomical structures, while positron emission tomography (PET) focuses on the functional processes in the body. These different modalities can be fused together. The resulting fused images offer a correlation of anatomical structure and functional information, thus providing help in many areas, such as diagnosing, tumor staging, and target delineation. For example, MRI and CT are fused together for the visualization and delineation of prostate cancer, as a tumor can be better visualized in MRI due to its excellent soft tissue contrast [42]. Image registration techniques need to be used to align the two image sets from different modalities that usually have some differences, either differences in patient positioning between the different scans at different times, or differences due to the movement of internal organs [43, 44]. A detailed review on image registration can be found in Section 2.5.3.

We can see that medical image processing techniques play a vital role in many areas of clinical applications. Almost every step in the RT process can benefit from advances in medical imaging processing. As a result, this thesis will focus on developing advanced image processing techniques in order to develop a 4D-MRI-based system for lung cancer RT.

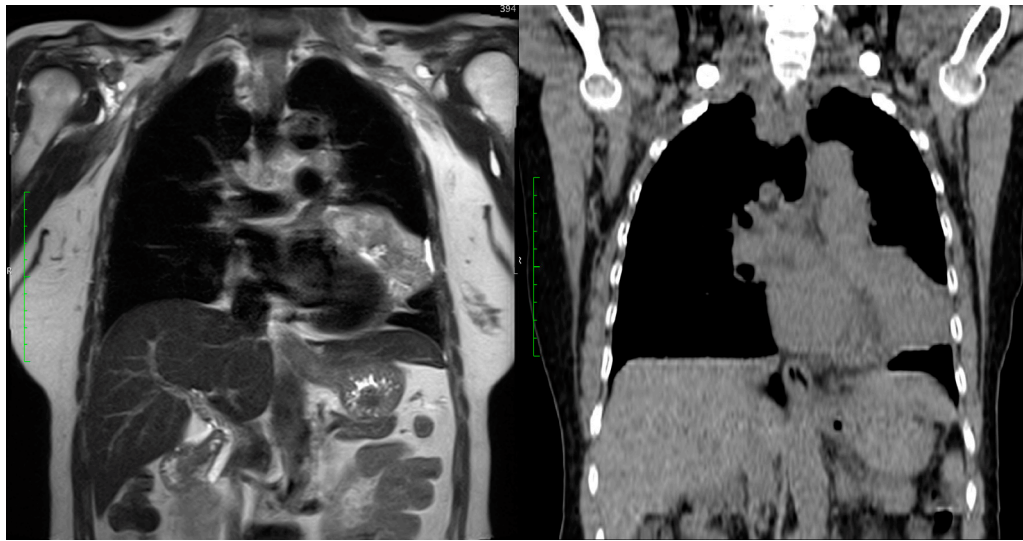
1.2 Motivation

Lagerwaard et al. have shown that lung tumors demonstrate significant mobility in all directions, which did not closely correlate with anatomic location [45]. Furthermore, the actual tumor motion could vary greatly against expected directions during inspiration and expiration [46]. Consequently, it is not possible to predict the tumors' mobility and to establish reliable tumor motion models based only on their locations. The individualized assessment of tumor mobility is needed.

Four-dimensional imaging techniques have enabled the individualized assessment of tumor mobility. With high spatial resolution and its ability to directly provide the electron density for dose calculation, CT is generally accepted as the radiological gold standard for visualization of the morphology of lung parenchyma [47]. However, CT involves radiation exposure, which is undesirable for prolonged imaging such as 4D imaging, particularly when applied for frequent follow-up examinations, during pregnancy, in children, and in clinical trials. The estimated equivalent dose for a full-body 3D-CT scan is about 1–10 mSv [48]. For 4D-CT, the radiation exposure is even larger, with a value of 30–40 mSv (average individual background radiation dose: 0.23 μ Sv/h [0.00023 mSv/h]) [49]. Due to its high radiation dose, current 4D-CT is not acquired continuously in real-time. It sorts images into respiratory phases within a single respiratory cycle based on an external motion indicator, such as using a respiratory belt that measures chest or abdomen motion. Thus, 4D-CT cannot compensate for interruptions due to coughing and cannot assess individual changes in respiration frequency and depth [49].

This thesis investigates the use of 4D-MRI for lung tumor imaging as a radiation-free alternative to 4D-CT. With recent developments in MRI, such as high-field 3 Tesla (3T) MRI and fast parallel imaging, MRI is able to acquire time-resolved volumetric images in order to capture the behavior of the lung in motion and has the potential to simultaneously provide different aspects of lung function data (e.g. perfusion, respiratory motion, ventilation, gas exchange) [50, 51]. As compared with CT, MRI is capable of producing image data sets in any orientations [52]. Due to its excellent soft tissue contrast (Figure 1-6), better visualization of tumor can be achieved, and pathologies, such as the fixation of a tumor mass to the heart, along with vessels, edema, or infiltrates of the lung can be detected [49]. Importantly, MRI does not involve any ionizing radiation, which enables the technique to be applicable to scientific work and to a wider group of patients, such as young children and pregnant women [47]. Without radiation, 4D-MRI can image for a longer period of time so as to cover individual changes in respiration depth and frequency, thus providing valuable additional information for therapy planning [49].

Currently, full 4D-MRI image-based RT is not yet practiced clinically but has potential. On-board MRI imaging together with accelerator for treatment delivery is under construction [53]. To fully use 4D-MRI to perform 4D-RT, a lack of validated, standardized planning tools exists, including accurate and automated multiple target structure segmentation, adaptive dose calculation, and a motion control delivery mechanism [49, 54].



MRI

CT

Figure 1-6 Comparison of thoracic image of MRI (left) and CT (right) of the same lung cancer patient. The image of MRI has better soft tissue contrast, given the fact that the window/level of the CT image is already adjusted for better visualization of soft tissue.

1.3 Objectives

This thesis focuses on the development of a 4D-MRI-based system for 4D-RT of lung cancer without excess exposure to radiation. Special attention is given to the 4D-MRI image acquisition; automated segmentation; visualization of multiple target structures using 4D-MRI; derivation of the respiratory motions of tumors and surrounding organs; and dose calculation. To achieve these objectives, this project's specific aims are:

(1) Compare and study several 4D-MRI sequences at 3T without the use of a contrast agent.

The acquisition of 4D MR images is the first and important step in the proposed system for 4D-RT. A recently developed MRI scanner with 3T field strength is believed to have upgraded capabilities in terms of temporal and spatial resolution, as compared with 1.5T MRI. Though a few 4D-MRI sequences are available for volumetric imaging over time, it is not clear which one(s) is suitable for thoracic imaging at 3T. This study's aim is to compare several 4D-MRI sequences at 3T without the use of a contrast agent via qualitative and quantitative assessments. Images of 4D-MRI are also compared with 4D-CT in order to fully evaluate the performance of 4D-MRI on lung cancer.

The original contribution of this study is that the suitable MRI sequence for dynamic thoracic imaging at 3T is determined to be TWIST. The study gains insights to the TWIST sequence, discusses the reason why it is capable of fast acquisition, which allows further development of MRI sequences. Through comparison between 4D-MRI and 4D-CT images, this study confirms that 4D-MRI is comparable to 4D-CT in both spatial and temporal domain, which provides a basis for the application of 4D-MRI as a complementary or replacement of 4D-CT.

(2) Develop techniques that enable the automated and more efficient segmentation of multiple target structures from 4D-MRI images.

One of the central challenges in processing 4D-MRI images is to extract the 3D shape of the lungs, tumors, and other organs at risk from each 3D image. The accuracy of segmentation determines the final success or failure of the entire application of RT. The workload of segmentation increases enormously when moving from a 3D image to a 4D dataset. Consequently, it is important to automatically segment multiple structures in an efficient manner. This study's aim is to develop an automated, accurate, efficient, and reproducible technique for the multi-structure segmentation of 4D-MRI images. This will contribute to the second step of 4D-RT: target delineation.

The original contribution of this study is that a novel spatio-temporal based registration-based segmentation scheme is developed. This scheme enables fast segmentation of 4D thoracic dataset without compromise of segmentation accuracy, which makes the quantitative study of large 4D dataset and detailed 4D-RT planning possible. In this study, we showed that it is possible to use repetitive motion (e.g. lung motion) to improve the efficiency of registration-based segmentation of large number of 3D datasets.

(3) Fusion of 4D-MRI images and static 3D-CT images

Compared with 4D-CT, the images of 4D-MRI have a relatively low spatial resolution. There is also a lack of a direct way to calculate radiation dose from MRI images. In order to overcome these drawbacks, it is proposed in this thesis to simulate 4D-CT images using static 3D-CT and 4D-MRI images. This will bring the advantages of MRI and CT together, which include high spatial resolution and the ability to provide the electron density for the dose calculation

of CT as well as the ability to continuously acquire volumetric images over a long period of time with MRI. This study's aim is to develop a novel method for transferring motion information in 4D-MRI to static 3D-CT.

The original contribution of this study is that a novel technique is developed that enables generation of simulated 4D-CT datasets without the access of high radiation. The simulated 4D-CT dataset is able to provide continuous motion information for better motion study and simulation, high spatial resolution for better segmentation accuracy, and electron density for the dose calculation. In this study, we showed that using lung surface deformation with a FEM lung model, it is possible to obtain a reasonably accurate deformation of the internal of the lung, even when tumor is present.

1.4 Organization of the thesis

This thesis aims to develop a 4D-MRI-based system for 4D-RT of lung cancer, which includes acquisition of 4D-MRI images, automated segmentation and visualization of target structures, and fusion of 4D-MRI and static 3D-CT images to aid in visualization and dose calculation. A schematic illustration of the proposed system is shown in Figure 1-7.

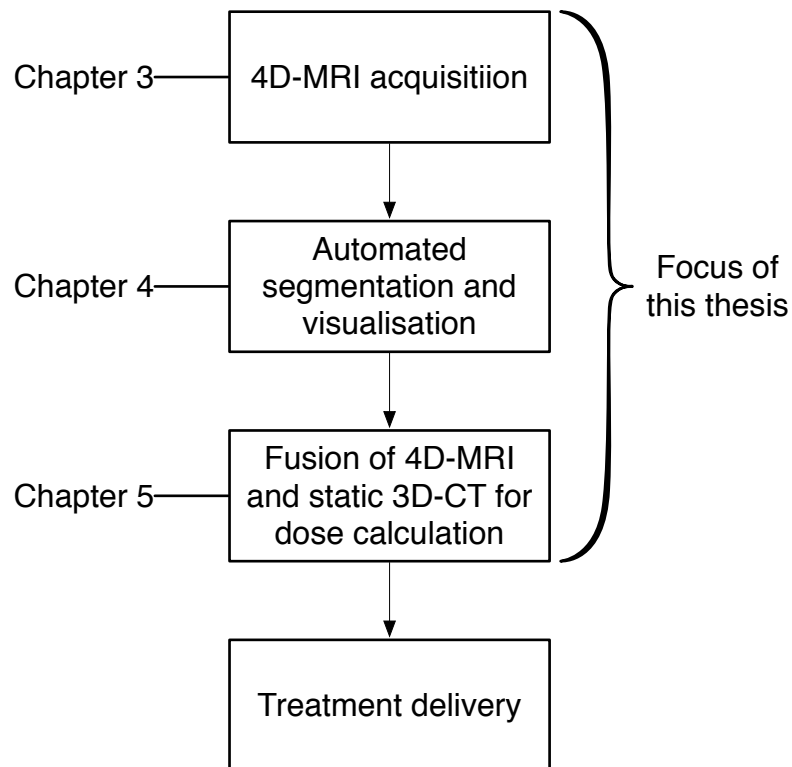


Figure 1-7 The scheme of the proposed 4D-MRI based system for 4D-RT of lung cancer. The words in various chapters are included.

Chapter 2 gives a detailed review of the literature that are closely related to this thesis, which includes the anatomy of the lungs and the mechanics of the respiratory motion, the causes of the lung cancer and different types of lung cancers as well as the treatments, the principals and the state of the arts of 4D imaging techniques (i.e. 4D-CT and 4D-MRI), the automated segmentation techniques that can be used to segment 4D dataset, and the deformable registration technique that is a key technique used in several works in this thesis.

Chapter 3 provides details on the evaluation of 4D-MRI sequences for imaging lung cancer patients. The main contributions in this field are the identification of a suitable 4D-MRI sequence for lung cancer imaging and proving that the information extracted from 4D-MRI images correlates well

with that from 4D-CT images, which is the current standard modality for 4D-RT of lung cancer.

Chapter 4 describes the development of an automated, accurate, and efficient registration-based segmentation scheme for the target delineation in a 4D-MRI dataset. This scheme saves the computational efforts without the expenses of segmentation accuracy.

Chapter 5 presents the development of a novel method for fusing 4D-MRI and static 3D-CT images. This provides new insights into the combination of the advantages of multiple modalities.

Finally, in Chapter 6, the integrated 4D-MRI-based system for 4D-RT of lung cancer patients is presented. The significance of the thesis is stated. The future research direction is also discussed.

Chapter 2 Literature review

2.1 Chapter overview

This chapter presents the review of the literature that are closely related to this thesis, which focuses on the development of a 4D-MRI-based 4D-RT system for lung cancer. The anatomy of the lungs, the mechanics of respiratory motion, the causes of lung cancer, and the different types of lung cancer as well as the treatment methods are first reviewed. The principals and the state of the arts of 4D imaging techniques (i.e. 4D-CT and 4D-MRI) are then introduced, and the pros and cons of the 4D-CT and 4D-MRI are discussed. Because automated segmentation techniques are critical for improved target delineation in 4D-RT, different automated segmentation techniques that can be used to segment a 4D dataset are reviewed. Special attention is given to the registration-based segmentation approach, as it has been shown to be a suitable technique for the segmentation of a 4D dataset. Deformable registration, which is a key technique for registration-based segmentation, is reviewed.

2.2 The Lungs and Its Respiratory Motion

The lungs are the essential respiratory organs in the thoracic cavity. Their main function is to bring oxygen from the atmosphere into the low-oxygen blood and to expel carbon dioxide from the blood to the atmosphere. The lungs reside in the thoracic cavity formed by the thoracic wall and the diaphragm and are separated by the mediastinum into the left lung and the right lung. Fissures divide the lungs into lobes, with two lobes in the left lung and three lobes in the right lung. Generally, the right lung is larger, heavier, and wider than the left one is because the heart bulges more to the left and forms a deep cardiac notch in the left lung. The right lung is also shorter because the right dome of the diaphragm is higher [55].

The trachea divides into the two primary bronchi (right and left primary bronchus) that enter the lungs. The primary bronchi continue to divide within the lung several times, forming the bronchioles, which lead to alveolar sacs. An alveolar sac consists of many alveoli that are tightly wrapped in blood vessels, and it is here that gas exchange actually occurs [56]. One pulmonary artery transports low-oxygen blood into each lung. Two pulmonary veins for each lung are responsible for draining oxygen-rich blood from it once the gas exchange has been completed. Figure 2-1 shows the anatomy of the lungs, the bronchi tree, and a zoom-in view of alveolar sacs.

Pulmonary ventilation, also known as breathing, includes the inhalation (inflow) and the exhalation (outflow) of air between the lungs and the atmosphere. Pressure changes during pulmonary ventilation stem from changes in lung volume and force air to flow into and out of the lungs. Expansion and

contraction of lungs change the lung volume and are controlled by the diaphragm and external intercostals. For inhalation, the contraction of the diaphragm causes the diaphragm to flatten itself, which increases the vertical diameter of the thoracic cavity. At the same time, the expanding of external intercostals elevates the ribs and increases the anteroposterior and lateral diameters of the chest cavity. For exhalation, the diaphragm and the external intercostals relax, causing the dome of the diaphragm to move superiorly and the ribs to be depressed. Thereby, the vertical, lateral, and anteroposterior diameters of the thoracic cavity decrease. The diaphragm and rib cage movement during inhalation and exhalation is illustrated in Figure 2-2.

On average, a healthy adult breathes 12 times a minute (five seconds per breathing cycle) at rest, with 500 mL of air moved during each inhalation and exhalation [56]. Many different breathing patterns have been observed in inter- and intra-subjects [57]. However, a more reproducible breathing pattern can be achieved when patients are aurally or visually guided to breathe shallowly [58].

The respiratory motion of the diaphragm, which is assumed to be one-dimensional in the cranial-caudal direction, has been proposed to be modeled with a periodic yet asymmetric function, with the majority of time spent at the exhale position, as shown in Figure 2-3 [59].

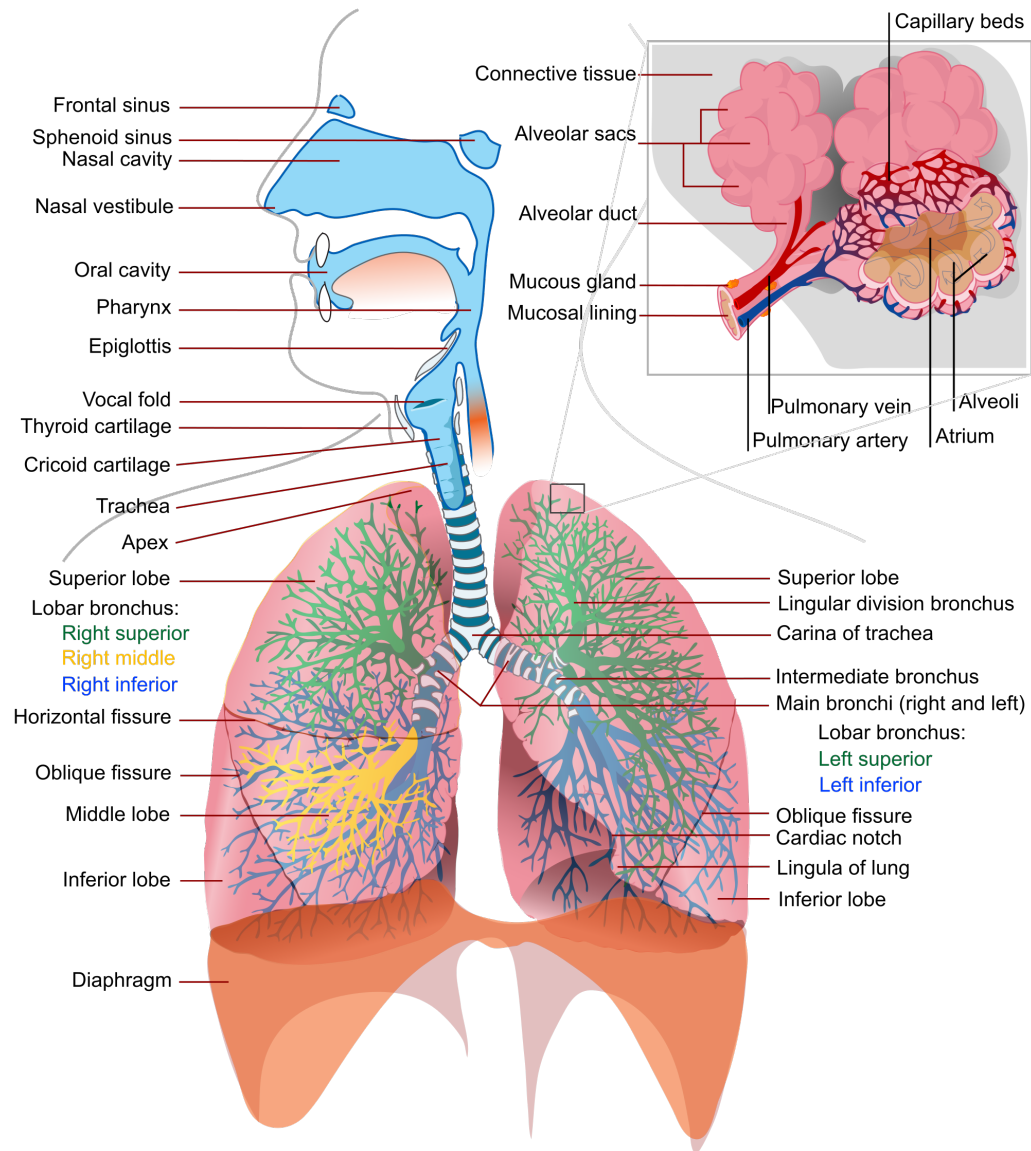
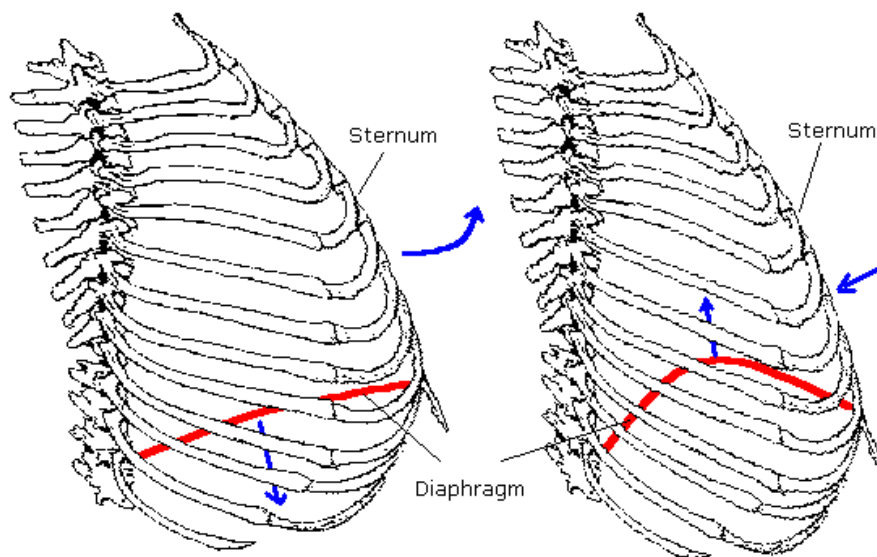


Figure 2-1 The anatomy of the lung, the bronchi tree, and the alveolar sacs [60]
 (permission to reproduce is granted by Wikimedia Commons.)

Breathing in and out



Breathing in:

Sternum rotated upwards as intercostals contract. Diaphragm descends

Breathing out:

Sternum rotates downwards as intercostals relax. Diaphragm ascends.

Figure 2-2 Illustrations of the movement of the diaphragm and the rib cage during breathing [61]. (Copyright(C) 2013 Yuxin Yang. Permission is granted to copy, distribute and/or modify this document under the terms of the GNU Free Documentation License, Version 1.3 or any later version published by the Free Software Foundation.)

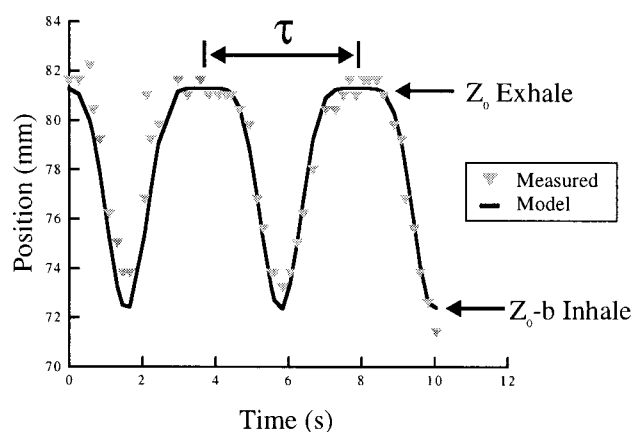


Figure 2-3 Measured position of diaphragm in fluoroscopic images (triangles) and mathematical fitted model (solid line) [59]. (Permission to reproduce is granted by American Association of Physicists in Medicine.)

Assuming a fixed period for the motion, the position of the diaphragm as a function of time can be modeled with a sinusoidal function:

$$Z(t) = Z_0 - b \cos^{2n} \left(\frac{\pi t}{\tau} - \phi \right) \quad (2.1)$$

where Z_0 is the position at exhale, b is the extent or amplitude of the motion, $Z_0 - b$ is the position at inhale, τ is the period of breathing cycle, n is a parameter that determines the general shape of the model in terms of steepness and flatness, and ϕ is the starting phase of the breathing cycle.

2.3 Lung cancer

As mentioned in Section 1.1.1, lung cancer is the leading cause of cancer death for both males and females in many countries. The long-term smoking of tobacco is the most common cause of lung cancer, directly linked to lung cancer in 90% of women and 79% of men [62]. For those never-smokers who experience lung cancer occurrence, second-hand smoke exposure is a major risk factor. Other common risk factors include exposure to other carcinogens, such as asbestos, radon, radiation, and combustion products [63]. Preexisting lung diseases, such as chronic obstructive pulmonary disease (COPD), could also lead to lung cancer if not properly treated [2].

Almost all lung cancers begin at the bronchial epithelium, with uncontrolled cells growing into lesions, which are mixtures of mature cartilage, fat, fibrous,

and blood vessels in varying proportions. The tumor can also spread into nearby tissues and even beyond the thoracic cavity.

Two main types of lung cancer exist, namely small-cell lung cancer (SCLC) and non-small-cell lung cancer (NSCLC). The SCLC is named for the small size of cancer cells. SCLCs tend to spread widely at an early stage and hence are not curable via surgery. They are best treated with chemotherapy and RT. NSCLCs contribute to 85% to 90% of lung cancers. Based on the size of the tumor and how it spreads (if any), NSCLC can be classified from stages I to IV [64]. They usually respond poorly to chemotherapy. Consequently, they are better treated by cutting a part of or the entire affected lung lobe if surgery is appropriate for the patient. RT is usually applied after surgery as well as to patients who are not surgical candidates due to medical conditions [65]. This thesis focuses on the RT of NSCLC patients.

2.4 4D imaging: continuous dynamic 3D images over time

The development of dynamic volume imaging is mainly motivated by RT for organs with respiratory motion. As discussed in Section 1.1.2, safety margins are currently estimated from population patients. By using 4D-imaging techniques, the assessment of patient-specific breathing motion and movement of organs and tumors are possible. This allows for the individual, personalized definition of safety margins. The generated images can then be correlated with

4D therapy planning. Currently, the available options are 4D-CT and 4D-MRI [49].

2.4.1 Computed tomography

X-ray computed tomography (CT) produces images that show different structures of the body based on the structures' ability to block the X-ray beam. When an X-ray beam passes through the body, its energy is lost due to scattering and absorption. The X-ray detector can record transmission of beams, displaying different intensities on the image. Consider a 2D fan-beam coming from a single X-ray tube that covers the entire body (Figure 2-4); when the tube rotates, a series of one-dimensional (1D) lines generated at different angles are acquired [66]. Different information will be captured in each 1D line because each 1D line is exposed at a different angle. Thus, each 1D line is a 1D projection of the 2D axial cross-section of the body at each angle. This collection of 1D projections can then be transformed using the inverse Radon transform [67] to reconstruct the 2D cross-sectional CT image. By moving the patient table in the cranial-caudal direction, different 2D axial images can be acquired and stacked to form a 3D CT image.

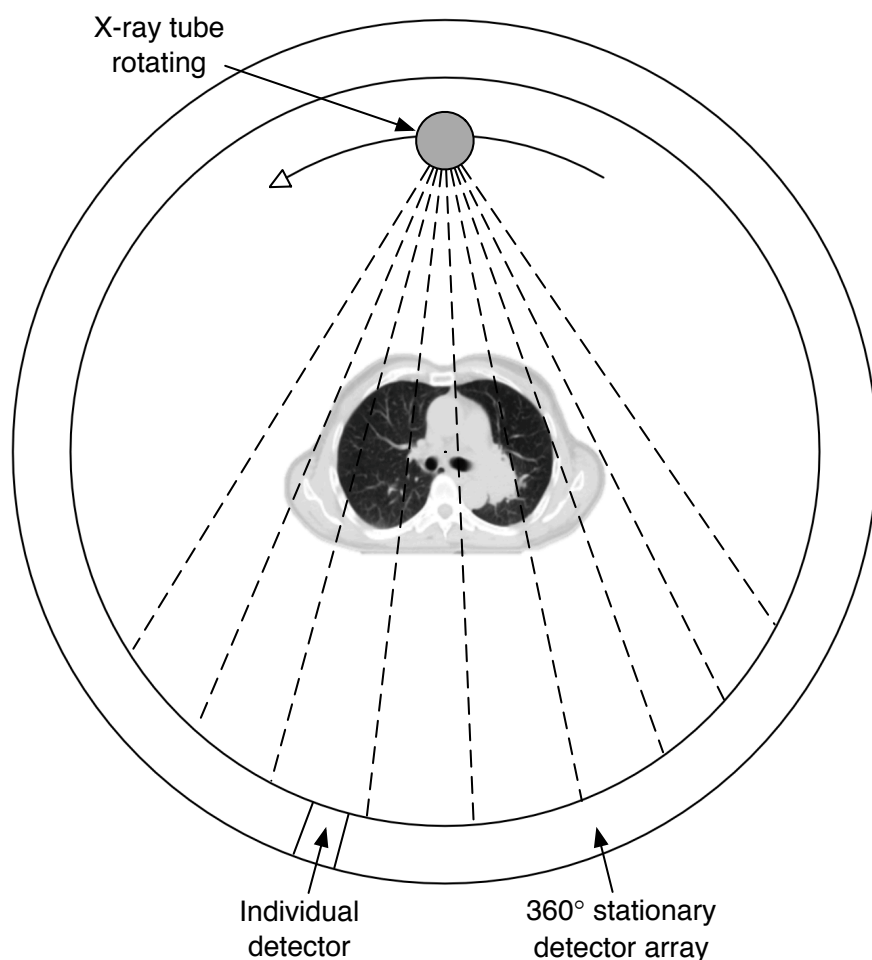


Figure 2-4 Generating a series of 1D projections of a 2D axial cross-sectional CT image with a fan-beam X-ray tube

However, when scanning patients under free breathing using conventional 3D CT, severe artifacts can be introduced via tumor and organ motion and can cause serious problems for the therapy planning of RT. Such artifacts appear due to the dynamic interaction between trans-axial image acquisition and the asynchronous motion of tumor and normal organs [68]. The motion artifact is often observed at the dome of the liver by showing a distorted structure. Slices of a tumor with large movement may be imaged in mixed order (Figure 2-5). Different artifacts may be obtained when CT data acquisition starts at different

positions of the breathing cycle and the variations in artifacts turn out to be unpredictable [68].

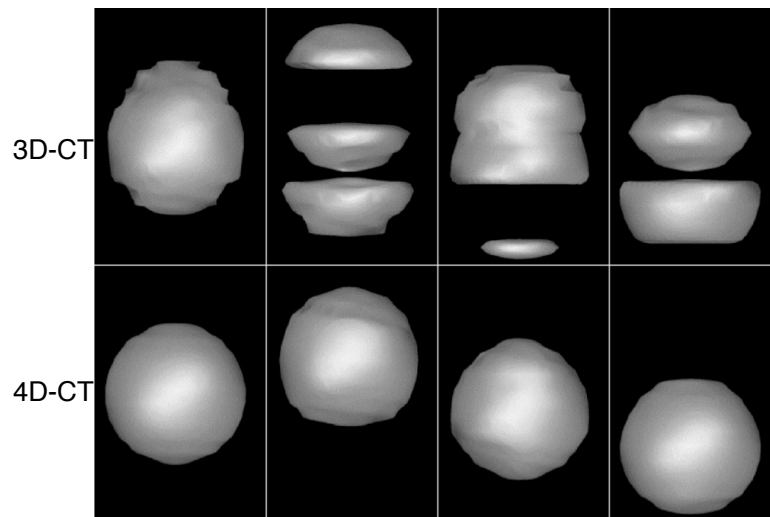


Figure 2-5 Iso-surface renderings of a spherical object scanned by 3D-CT (top) and 4D-CT (bottom) at different positions of the motion cycle. Three dimensional CT showed a severe motion artifact, and the artifact changed at different positions of the motion cycle [68]. (Permission to reproduce has been granted by the American Association of Physicists in Medicine.)

Taking scans under breath-hold can significantly reduce artifacts induced by respiratory motion. However, the motion information of a tumor and normal organs is lost in this case. As discussed in Section 1.1.2, motion information is crucial to carrying out 4D-RT. Thus, the time-resolved 3D-CT, i.e. 4D-CT, was introduced. An example of a 4D-CT scanner is shown in Figure 2-6.



Figure 2-6 An example of a 4D-CT scanner (Brilliance CT Big Bore, Philips, Eindhoven, The Netherlands). This 4D-CT scanner was used to acquire the 4D-CT dataset of patients who were studied in this thesis.

Four-dimensional CT images are usually taken using two different methods (i.e. prospective and retrospective). Prospective 4D-CT [69, 70] produces a single 3D image at the selected respiratory phase by using respiratory-gated image acquisition. The process has to be repeated several times in order to complete an entire respiratory cycle that covers all of the respiratory phases. On the other hand, retrospective 4D-CT [71, 72] continuously acquires 2D slices from all respiratory phases and then sorts them into appropriate phases so as to form corresponding individual 3D images, as illustrated in Figure 2-7. Both approaches need an external motion indicator (Figure 2-8) as the reference of the respiratory phases.

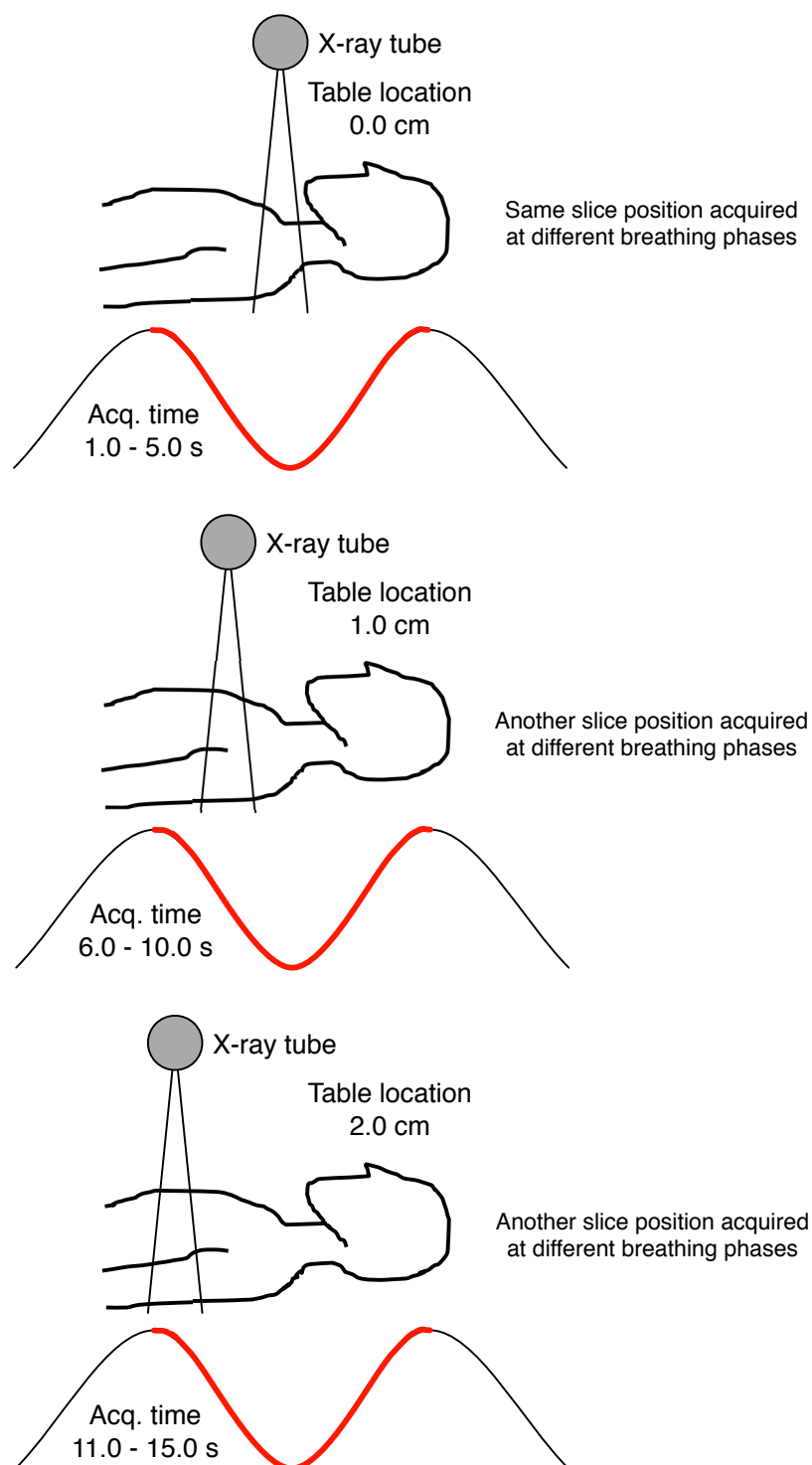


Figure 2-7 Retrospective acquisition of 4D-CT dataset. Two-dimensional slices are continuously imaged from all respiratory phases and are then sorted into appropriate phases to form corresponding individual 3D images based on the respiratory signal.



Figure 2-8 A respiratory belt senses the abdomen movement to generate a respiratory signal

Another approach is the use of cone-beam technology for fast image acquisition [73-75]. Instead of a fan-beam and a linear detector, a cone beam and an area detector are used. In this case, cone-beam CT is capable of rotating the cone-beam source and recording 2D projection images on the area detector at different angles. Those 2D projections can then be reconstructed to create a 3D volumetric image, just as 1D projections can be reconstructed to form 2D images. Although cone-beam CT can generate fast 3D images, the quality of those images is poor, with lots of artifacts. Currently, cone-beam CT is mainly used for on-board imaging during RT so as to position the patient and to synchronize planning with the patient's position.

Due to the high radiation dose involved, 4D-CT usually covers only one averaged full respiratory cycle. Thus, 4D-CT is not capable of examining the individual changes during respiration. However, CT is still the current gold

standard in pulmonary imaging due to its high spatial resolution. CT is also the standard modality for treatment planning in RT because the electron density can be directly provided in Hounsfield units through CT images. This allows for the calculation of the radiological path length to each voxel for treatment planning [76, 77].

2.4.2 Magnetic resonance imaging

MRI visualizes the detailed internal structures of an object by constructing pictures of the nuclear magnetic resonance (NMR) signals from the hydrogen atoms. In medical MRI, NMR signals mainly come from water and fat because water and fat are the human body's major hydrogen-containing components [78]. To perform a MRI scan, a high magnetic field is first placed around the patient. An oscillating electromagnetic field called radiofrequency (RF) pulse is supplied to provide the required energy [79]. Hydrogen atoms are then excited by the RF pulse and emit signals to be detected forming a MRI image.

2.4.2.1 Imaging sequences

Many MRI sequences are used for different clinical applications. All of these sequences can be categorized into either a spin-echo or gradient-echo-based acquisition method.

Spin-echo Imaging Sequences

The spin-echo imaging sequence, shown in Figure 2-9 (a), is often used to measure T_2 values. The spin-echo sequence involves two RF pulses: The first 90° pulse creates the component of transverse magnetization, and the 180° pulse refocuses the T_2^+ relaxation and produces a signal called an echo [80]. T_1 - and T_2 -contrast weighting can be introduced in the image by adjusting echo time (TE) and repetition time (TR) of the RF pulse [79].

Gradient-echo Imaging Sequences

Spin-echo sequences generally generate high contrast-to-noise ratio (CNR) and signal-to-noise ratio (SNR) images. However, the acquisition time of spin-echo sequences is long. Gradient-echo (GRE) sequences, shown in Figure 2-9(b), do not have the T_2^+ refocusing pulse. This allows shorter TR and TE to be used [78, 81].

Commonly used GRE sequences include a fast low-angle shot (FLASH), fast imaging with steady precession (FISP), gradient-refocused acquisition in the steady state (GRASS), and steady-state free precession (SSFP).

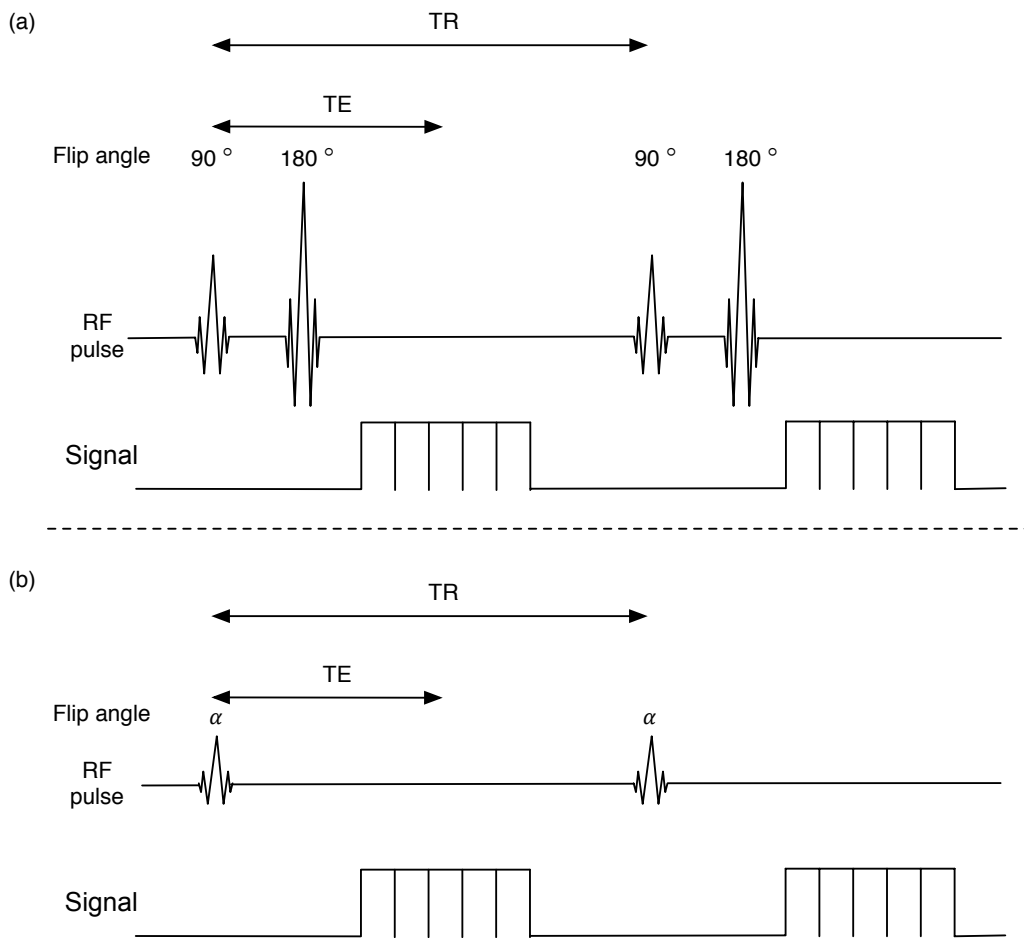


Figure 2-9 Illustration of MRI sequences (a) spin-echo and (b) gradient-echo

2.4.2.2 Dynamic MRI

Dynamic MRI is the repeated acquisition of images at the same slice or volume location. Compared with 4D-CT, dynamic MRI (Figure 2-10) can image respiratory motion over a longer period of time. Thus, the individual changes in respiration can be obtained. Acquisition time is an important factor in dynamic imaging because fast acquisition of datasets allows for a detailed study of motion.



Figure 2-10 An example of the 3T MRI scanner (Siemens Trio MRI scanner, Siemens Healthcare, Erlangen, Germany). This scanner was used in the studies presented in this thesis.

In order to speed up the acquisition of a volume, a short TR value has to be applied, which limits the sequences to be T_1 -weighted. One simple way to reduce the acquisition time is to reduce the spatial resolution of a volume. Consequently, the visual quality of the volume is dropped. Thus, the spatial and temporal resolutions need to be balanced. A need exists to achieve fast acquisition of 3D-MR volumes while maintaining the spatial resolution at a relatively high level.

Several methods have been developed to speed up the acquisition time of the dynamic MRI imaging without reducing the spatial resolution. One method is called parallel imaging. Parallel imaging skips some of the phase-encoding steps but reconstructs the missing signals from combinations of the separate coil signals [82]. The speed-up factor R is the number of phase-encoding lines

that have been omitted, but it is usually limited to between 2 and 4. This is due to the trade-off in terms of decreased signal-to-noise ratio (SNR)s given by:

$$SNR' = \frac{SNR}{\sqrt{R}} \quad (2.2)$$

Another method for reducing the acquisition time is called echo-sharing or view-sharing (TREAT/TWIST/TRICKS sequence). It reconstructs a new image with the timing being exactly in between two original images. The reconstructed image uses the second half of the k -lines from the previous original image and the first half of the k -lines from the next original image [83]. Fast parallel imaging for 2D dynamic MRI (2D + time) has been achieved using sequences of 2D GRE and SSFP on both 1.5T and 3T systems [84]. Similar to 2D dynamic MRI, 3D dynamic (4D) MRI is acquired by using fast 3D-GRE or SSFP sequences. Echo sharing and parallel imaging techniques have achieved a fast acquisition time of up to 1 volume per second. A list of representative 4D-MRI imaging applied for lung imaging in the literature is summarized in Table 2-1.

Recently, new techniques have been developed for the purpose of achieving fast acquisition. Compressed sensing is one of them. Compressed sensing aims to acquire significantly fewer measurements of the signal values (k -space data points) and non-linearly reconstructs them to form a complete k -space with good accuracy [85]. However, although the new techniques are promising, many unsettled crucial issues exist. Thus, these techniques are yet to be used in clinical applications.

Table 2-1 4D-MRI sequences for lung imaging that has been applied in the literature

Sequence	Tesla	Spatial res. (mm ³)	Temp. res. (s/volume)	Literature
FLASH 3D	1.5	3.8×3.8×3.8	1.0	<i>Plathow et al. 2006 [20]</i>
TREAT	1.5	2.7×2.7×4	1.4	<i>Biederer et al. 2009 [86]</i>
TREAT	1.5	3.1×3.1×4	1.4	<i>Dinkel et al. 2009 [87]</i>
TRICKS	1.5	4.9×3.1×3.8	1.0	<i>Plathow et al. 2009 [88]</i>

FLASH 3D: Fast Low-angle SnapsHot 3D imaging; **TREAT:** Time-resolved Echo-shared Angiographic Technique; **TRICKS:** Time-resolved Imaging of Contrast KineticS, equivalent to TWIST from Siemens

Another way to generate 4D MRI is retrospectively gated with 2D-GRE sequences, which are sorted by respiratory phases [89]. This method is similar to the 4D-CT acquisition techniques described in Section 2.4.1. Image quality is improved via this method, but it is not a “real-time” acquisition. Thus, 4D-CT is unable to cover individual changes in respiration frequency.

Most of the 4D-MRI applications use 1.5T magnetic field strength (Table 2-2). In recent years, three Tesla (3T) high-field MRI scanners have been available for clinical use. With improved signal-to-noise ratios (SNR) due to higher magnetic field strength, MRI scanner with 3T field strength has been found to have upgraded capabilities in terms of temporal and spatial resolution, as compared with 1.5T MRI [90-92], thus allowing a shortened examination time and resulting in an improved image quality [93]. However, few studies have been done to evaluate the performance of 4D-MRI imaging at 3T. This will be discussed in Section 3.2.

2.4.3 Comparison of 4D-CT and 4D-MRI

Generally, 4D-MRI has lower spatial resolution than does 4D-CT, with a typical spatial resolution of $3 \times 3 \times 4$ mm for 4D-MRI and $(0.5-1.5) \times (0.5-1.5) \times (1-5)$ mm for 4D-CT. 4D-CT also has a faster acquisition time than 4D-MRI does. It takes about 200 ms to 500 ms to acquire a single 3D image of a 4D-CT dataset, while 4D-MRI takes about 1 s to scan a single 3D image. With a faster acquisition time, 4D-CT can image more positions within a breathing cycle. Usually, 4D-CT captures 10 breathing phases.

However, 4D-CT uses a fixed acquisition scheme, and only acquisition in axial-plane is possible. Furthermore, 4D-CT averages multiple breathing cycles to form images that represent a single breathing cycle, which makes it unable to cover the individual changes in respiration frequency and depth. If patients experience irregular breathing patterns, a severe motion artifact will appear on the images (as shown in Figure 2-11). Due to its high radiation dose, multiple repetition of the scan is also prohibited. Four-dimensional MRI, on the other hand, is more flexible. One can freely choose the imaging plane (axial, coronal, and sagittal) and various breathing maneuvers (e.g. free-breathing, deep breathing). Without any radiation involved, 4D-MRI is capable of imaging for a prolonged time and of capturing the “real-time” motion. However, due to its long acquisition time, current 4D-MRI is more suitable for slow controlled breathing.

In the context of RT, 4D-CT is preferred; as it provides valid radiation transmission data directly, while for 4D-MRI, this information needs to be estimated. The pros and cons of 4D-CT and 4D-MRI are summarized in Table 2-2.

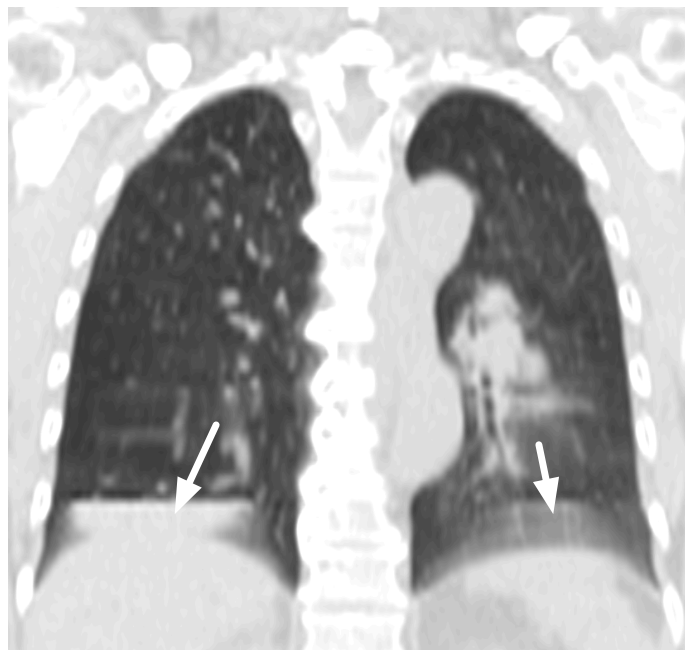


Figure 2-11 Severe motion artifact at the dome of the diaphragm (white arrow) due to irregular breathing during 4D-CT acquisition

Table 2-2 Comparison of 4D-CT and 4D-MRI

	4D-CT	4D-MRI
Spatial res. (mm ³)	(0.5-1.5)×(0.5-1.5)×(1-5)	3×3×4
Temporal res. (s/volume)	0.2-0.5	1
Effective dose (mSv)	30-40	None
Choice of imaging plane	Axial	Axial, Coronal, Sagittal, Oblique
Multiple repetition	Prohibited	Allowed
Breathing maneuver	Fixed scheme	Instructed breathing maneuvers possible
Able to cover individual changes in respiration frequency and depth	No	Yes

2.5 Automated segmentation of 4D medical images for RT planning

Precise segmentation of the structures of interests is required in many applications, such as the derivation the volumetric measurements for quantitative analysis and the delineation of the target structure in RT planning. With 4D images, it is now possible to visualize the displacement and deformation of a tumor during respiration, which is central in 4D-RT. However, the manual segmentation of a 4D dataset that typically contains many 3D volumes is extremely tedious and time-consuming. Further, manual segmentation could also result in large intra- and inter-user variability. Automating the segmentation could reduce the workload largely and decrease both intra- and inter-user variability. Consequently, automated segmentation techniques for 4D dataset are needed.

Simple methods such as thresholding, region-growing, watersheds, clustering, and classification [94-96] can be useful for the segmentation of synthetic images and some real images with well-defined contrast. However, they have a number of limitations. Medical images usually are of low contrast and tend to be very noisy. It is difficult to choose the correct threshold value for thresholding techniques. It is also very hard for the user to define the homogeneity criteria in medical images with low contrast when using the region-growing approach. All of these methods are sensitive to noise and intensity inhomogeneity, especially for the watershed and clustering algorithms, which may cause the segmented regions to have holes or to become

disconnected and thus result in over-segmentation. As a result, more sophisticated methods are needed.

2.5.1 4D Segmentation

In this thesis, 4D segmentation is defined as the segmentation of a 4D dataset (3D volumes of the same subject acquired over time). Hence, 4D segmentation techniques refer to segmentation techniques that can be applied to segmenting 4D datasets. A few segmentation techniques have been proposed for segmenting 4D-CT/MRI cardiac and thoracic images in a more automated manner. These techniques include the use of a deformable model, statistical shape model, graph/watersheds cuts, and image registration.

The deformable model method moves surfaces that deform to match any kind of shape and detect the surfaces of target objects [97]. The first deformable model was proposed by *Kass et al.* [98] and is generally known as the “snake.” The surface can be represented either explicitly [37-39] by listing all of the coordinates of surface points or implicitly [99, 100] by representing the surface with some functions. The method usually iteratively deforms the surface by minimization of the total energy or by using the level set method to search for the desired location. The deformable model method can be accurate if the model is designed properly. However, it is often difficult to choose appropriate parameters. The deformable model method requires manual interaction to place an initial model in each 3D volume within a 4D dataset and does not fully use the prior information contained in a 4D dataset.

The statistical shape model method [101, 102] constructs the prior segmented 3D target structures as well as the motion information between them into a statistical model. This model is then used to segment structures that have the “typical” shape and moving pattern of new datasets. *O’Brien et al.* [101] and *Leiner et al.* [102] used this technique to segment the left ventricle. A limitation of this method is that additional time and interactions are needed to accumulate enough segmented target structures and motion information for training. The training process can be very tedious because the segmented 3D structures are usually acquired manually.

For the graph/watershed cuts method [103, 104], seeds inside the object phase and background phase are first placed. The images are then separated into three kinds of nodes: object, background, and image nodes. Then, a 4D graph can be constructed to link the object, background, and image nodes spatially and temporally in the 4D dataset. Weights of these links are based on image intensity as well as spatial and temporal position. Severed links classify each image node into either object or background. The cost of a cut is the sum of weights of all severed edges. Thus, segmentation is achieved by finding a minimum cut. *Cousty et al.* [104] developed the watershed cut technique to segment the left ventricle, and *Lombaert et al.* [103, 104] employed the graph cut method to segment the entire heart. Similar to the statistical shape model method, the graph/watershed cuts method also requires many data training processes. Also, the training process and the calculation of weights are very computational-intensive.

Other than the techniques discussed above, the registration-based segmentation approach has been a popular choice for segmenting the 4D dataset because it does not require a training phase and works well for images with

similar structures. Using this method, good segmentation results have been achieved. Hence, this is the main approach on which this thesis will focus. This method is explained in Section 2.5.2.

2.5.2 Registration-based segmentation

The registration-based segmentation approach uses registration techniques to solve the segmentation problem. Registration plays the most crucial role in this method, as the registration technique transforms an image in order to spatially align the corresponding parts with respect to the target image. The basic scheme [105] for performing registration-based segmentation of a 4D dataset is illustrated in Figure 2-12. A reference volume (v_{ref}) is chosen and segmented separately. The segmented reference volume will serve as the template (m) for propagation. Three dimensional registration is then applied between target volumes (v_t , $t = 1, 2, 3, \dots, n$) and the reference volume to get the displacement fields from the reference volume to the target volumes ($\mathbf{r}_{(v_{ref} \rightarrow v_t)}$), together with the registered reference volumes. The corresponding displacement fields are then used to deform the template into the corresponding segmented target volumes.

The registration-based segmentation method has been widely used for the 3D segmentation of structures that are stable in the population being studied, such as the brain [106-108]. This is because even with deformable registration methods, it is sometimes difficult to find accurate segmentations of complex structures due to anatomical variability [36]. In the context of 4D image segmentation, registration-based segmentation seems to be the ideal tool

compared with other segmentation techniques. For 4D images, the time spacing between two 3D scans is generally very small. Consequently, the structures are very similar between the scans, with only some minor differences. The registration-based segmentation technique can fully exploit this property of 4D images because accurate registration can be easily performed with such a small difference between two images. Moreover, the registration-based segmentation algorithm delineates its deformation of reference segmentation based not only on the reference segmentation itself but also on its surrounding structures and global transformations [109]. Hence, the registration-based segmentation approach can handle complex segmentation problems and also work for images with low contrast or with regions where no clear boundaries exist between target structures. Unlike segmentation approaches that use statistical prior knowledge, the registration-based framework does not require a training phase using large dataset; rather, it only requires the prior segmentation of the template image/volume for subsequent propagation [110].

Registration-based segmentation has been employed in a number of 4D segmentation problems. For 4D-CT thoracic data, approaches including B-spline registration [21, 111-113], calculus of variations method [114], and demons registration [115] have been reported. Several works have evaluated registration methods including demons and B-spline registration with regard to segmentation results and the alignment of anatomical landmarks [116-119]. They found that the demons method generated slightly more accurate results and can handle local deformations of the lung. Gu et al. implemented demons registration and five of its variations on a graphic processing unit (GPU) to accelerate the segmentation process [120]. They evaluated the six demons algorithms and reported that the original demons algorithm outperformed other

variants based on accuracy, efficiency, and ease of implementation. Other works implemented the registration-based segmentation of a 4D dataset, including 4D cardiac segmentation in MRI [121, 122] and CT [123, 124] as well as the segmentation of liver and kidney in a 4D-CT dataset [125].

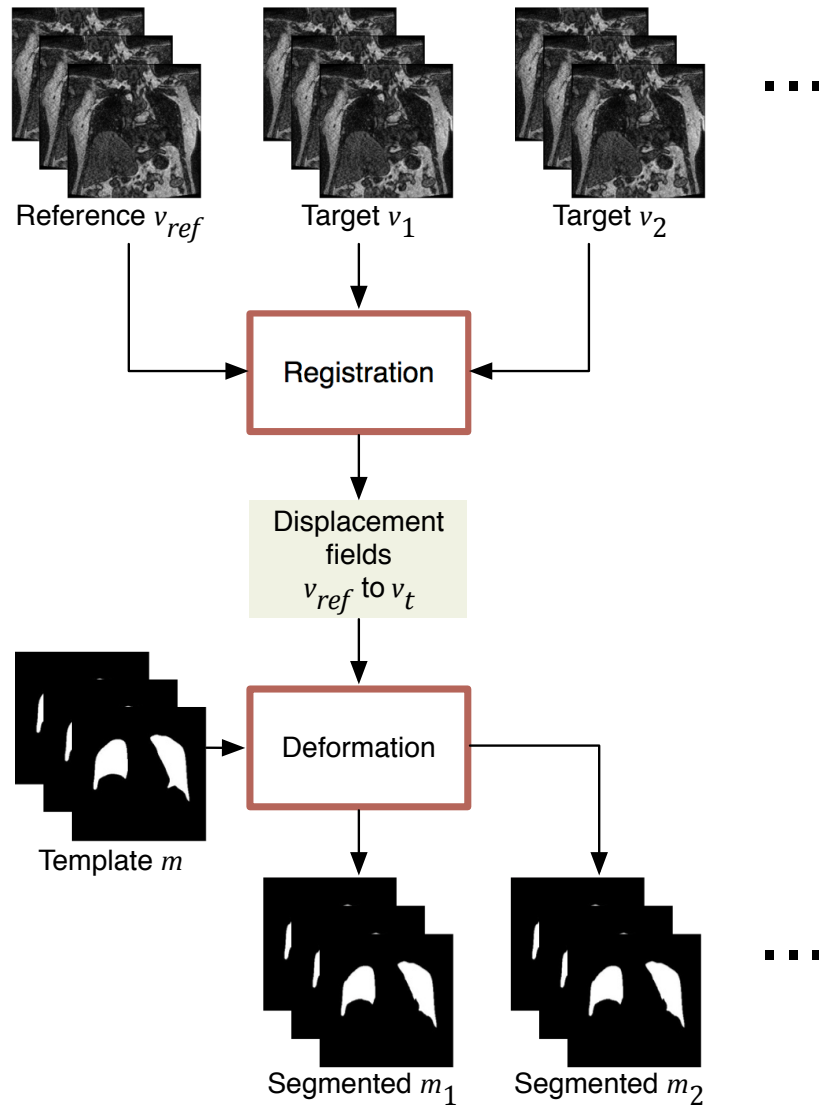


Figure 2-12 An illustration of the overall basic registration-based segmentation scheme

2.5.3 Deformable registration

Registration is a fundamental tool in image processing used to match two or more images [126]. It is also the most important step in registration-based segmentation. In general, registration can be divided into two main types: rigid and deformable. The main difference lies in the transformation. The transformation of rigid registration is linear, including rotation, scaling, and translation. Deformable registration, also known as non-rigid registration, transforms an image in a non-linear manner, such as shape change and warping. In the application of 4D medical images, the transformation involved is mainly non-linear. Hence, the focus here is on the deformable registration.

The flowchart of a typical image registration framework is shown in Figure 2-13. The aim is to transform the moving image by optimizing a cost function that embeds a similarity measure and regularization terms. The multi-resolution approach is usually performed in order to achieve accurate and fast registration.

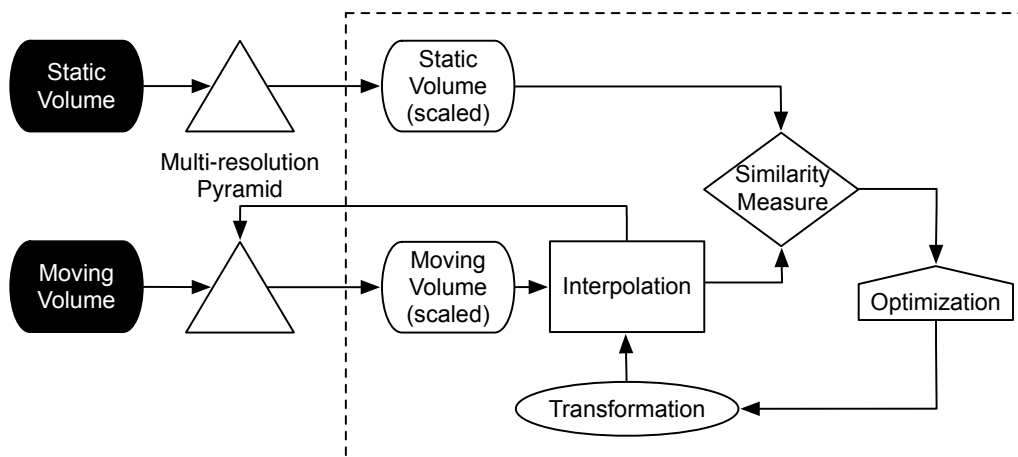


Figure 2-13 Registration framework showing the key steps in registration

2.5.3.1 Similarity measure

Similarity measure is used to quantify how similar the two images are. Generally, two kinds of similarity measure are commonly used, namely the surface-based and intensity-based methods.

Surface-based, also called geometry-based, similarity measure compares the spatial information extracted from images, such as anatomical landmarks, curves, and surfaces [127]. With clear features extracted, this measure can lead to a precise registration result. However, user intervention is often required to get spatial information from images beforehand. The manual intervention would incur variability. It is also not suitable for the automated registration-based segmentation of 4D images.

The intensity-based approach measures the degree of similarity between intensity patterns of two volumes v_1 and v_2 . The simplest method is to use the sum of square distance (SSD) manner:

$$SSD = \sum_x \sum_y \sum_z [v_1(x, y, z) - v_2(x, y, z)]^2 \quad (2.3)$$

It is fast but very sensitive to noise. Also, it can only be used with mono-modal images.

A more tolerant measure is cross-correlation (XCOR):

$$XCOR = \frac{\sum_x \sum_y \sum_z v_1(x, y, z) v_2(x, y, z)}{[\sum_x \sum_y \sum_z v_1(x, y, z)^2 \sum_x \sum_y \sum_z v_2(x, y, z)^2]^{\frac{1}{2}}} \quad (2.4)$$

It can work on images with multi-modality but also is sensitive to noise. The volume of summation in Equation (2.3) and (2.4) is defined as the union of both datasets.

Another method for multi-modality images is called mutual information (MI) [128]:

$$MI = H(v_1) + H(v_2) - H(v_1, v_2) \quad (2.5)$$

where $H(v_1)$ and $H(v_2)$ are the marginal entropies and $H(v_1, v_2)$ is the joint entropy of the two volumes. It has been widely used to register images from multiple modalities [128-130]. However, it is computation-intensive compared with other methods.

Other than the three commonly used similarity measures discussed above, some new similarity measures have been introduced recently, such as phase mutual information [131] and Gaussian-windowed similarity measure [132].

2.5.3.2 Transformation

Transformation determines how the moving image is being deformed. Different transformation methods can be applied with respect to the type of applications and the nature of the target images. These methods can be generally categorized into two types, namely parametric transformation and non-parametric transformation.

Parametric Transformation

Deformable registration can be solved using parametric algorithms, including affine transformation, polynomial transformation, and spline-based transformation.

Affine transformation involves translation, rotation, scaling, and shearing and can be characterized by affine transformation matrix [126]:

$$\begin{bmatrix} x_B \\ y_B \\ 1 \end{bmatrix} = \begin{bmatrix} a_{11} & a_{12} & a_{13} \\ a_{21} & a_{22} & a_{23} \\ 0 & 0 & 1 \end{bmatrix} \begin{bmatrix} x_A \\ y_A \\ 1 \end{bmatrix} \quad (2.6)$$

where x_A and y_A are the coordinates before transformation; x_B and y_B are the coordinates after transformation. Equation (2.6) is in homogeneous coordinate system. For the simplicity of illustration, only 2D situation is shown. (Same for Equation (2.7) and (2.8).)

Affine transformation has seven degrees of freedom (DOF) for 2D images and 12 DOF in 3D volumes. It is computation-efficient and is easy to implement. However, it cannot accommodate local deformations because the same transformation is applied consistently to all pixels in the image.

Another representation of parametric transformation is a polynomial function. The polynomial transformation has the form:

$$x_B = \sum_i \sum_j a_{ij} x_A^i y_A^j \quad y_B = \sum_i \sum_j b_{ij} x_A^i y_A^j \quad (2.7)$$

where a_{ij} and b_{ij} are the constant polynomial coefficients to be determined [133]. Polynomial transformation can deform an image more than affine

transformation can. However, it is still only useful when accounting for low-frequency distortions because of its unpredictable behavior [126].

Spline-based transformation uses a set of basis functions that represent the transformation function:

$$x_B = \sum_k a_k h_k(x_A, y_A) \quad y_B = \sum_k b_k h_k(x_A, y_A) \quad (2.8)$$

where $h_k(x_A, y_A)$ is the basis function. The advantage of spline-based transformation is that it can handle some local deformations. Frequently used algorithms include thin-plate spline [134] and B-spline [135].

Non-parametric Transformation

Non-parametric transformation is an advanced type of transformation. It is not restricted to a finite dimensional space, compared with parametric approach. In general, the transformation function \mathbf{r} of the moving image v_{ref} is represented as the displacement of each point in v_{ref} . The aim is to find the \mathbf{r} that minimizes the cost function C [136]:

$$\arg \min_{\mathbf{r}} C = D[v_t, \mathbf{r}(v_{ref})] + \alpha R(\mathbf{r}) \quad (2.9)$$

where v_t is the fixed target image, D is the dissimilarity between the two images, R is the regularizing term, and α is a regularizing parameter.

Non-parametric transformation can be divided into four categories, depending on the smoother R used: elastic registration, fluid registration, diffusion registration, and curvature registration.

Elastic registration considers the images as an elastic body [137]. It is characterized by a spatial smoothing of the displacement field. Elastic registration is easy to understand and implement, but it only works for linear elastic deformations with only small changes of displacement. This is due to its restricted regularizer [136].

Compared with elastic registration, fluid registration can be characterized by the smoothing of the velocity field [138]. Fluid registration is powerful, and it is possible to align any target image to any reference image with the same gray-scale range. However, unrealistic solutions are often observed for medical images because this method is based on fluid-like bodies, and anatomical objects do not deform fully fluid-like in general [136].

Unlike elastic and fluid registration, which is based on spatial properties of images, diffusion registration is based on the first derivatives of the displacement. One special type of diffusion registration is called demons registration [139]. It places “demons” at certain locations in the reference image, and the “demons” decide the diffusion of the target image by minimizing the difference between the two images. The calculation of the displacement of “demons” were inspired from the optical flow method [140].

Variations of the original demons registration have been proposed to utilize information from both the moving and reference images [141-144]. Diffusion

registration performs best with images with small changes, but it can be combined with the fluid registration to allow for larger deformations.

Curvature registration is based on second-order derivatives. The deformation field is calculated by minimizing a suitable similarity measure to a curvature-based constraint [145]. Compared with elastic, fluid, and diffusion registration, curvature registration is more sensitive to initial affine linear displacements but is less dependent on the initial position of the reference and moving images [136].

2.5.3.3 Optimization

Optimization determines the final deformation through minimizing the similarity score. Popular methods include gradient descent and Newton's method. Gradient descent is a first-order optimization algorithm that finds a local minimum through the negative of the gradient of the function at a current point. Newton's method is a second-order iterative method used to find critical points of differentiable functions [146].

In parametric registration, a numerical solution of parameters can be obtained by using higher-order methods, such as Newton's method. In non-parametric registration, Equation (2.9) can be solved using the gradient descent method [136] or can involve the use of the scheme of demons method, which is also based on the gradient. Higher-order schemes, such as Newton's method, are not suitable because they require intensive computations.

Chapter 3 Evaluation of 4D-MRI sequences at 3T for lung cancer imaging

3.1 Chapter overview

As discussed in Section 2.4, CT images are generally accepted as the radiological gold standard for visualization of the morphology of the lung parenchyma but the high radiation involved in CT prohibits continuous scanning to generate ‘real-time’ volumetric images. MRI, on the other hand, is able to generate ‘real-time’ volumetric images that allow the behavior of the lung and tumor in motion to be captured. Additionally, MRI has an excellent soft tissue contrast and is capable of producing image datasets in any orientation [147]. With recent advancements in MRI technology such as high-field 3T scanning, MRI has improved in both image quality and temporal resolution. However, the performance of 4D-MRI sequences for lung cancer imaging at 3T is still unclear. It is necessary to evaluate 4D-MR sequences at 3T for lung cancer patients.

Two studies are presented in this chapter for this purpose. The first study aims at comparing three 4D-MRI sequences (TWIST, VIBE, and FLASH 3D)

at 3T in terms of image quality and their ability to capture lung and lung tumor motion. Results showed that FLASH 3D exhibited the best image quality among the three sequences while TWIST has a high temporal resolution, which makes it sufficient to study the motion of tumor and diaphragm under controlled breathing.

The second study focuses on the comparison between 4D-MRI and 4D-CT of lung cancer patients as 4D-CT is generally accepted as the gold standard for lung cancer patients. Tumor volume and motion of the volumes from the same patients were used for comparison. Analyses showed that 4D-MRI exhibited equal ability to present the tumor volume and to describe the tumor motion as 4D-CT.

All the volume estimations of MRI images in Chapter 3 use a spatio-temporal based registration-based segmentation scheme that will be introduced in Chapter 4.

3.2 Comparison of 3D dynamic MR sequences at 3T for imaging of lung cancer

Three Tesla (3T) high-field MRI scanners have been recently available for clinical use. With improved signal-to-noise ratios (SNR) due to higher magnetic field strength, MRI scanner with 3T field strength has been found to have upgraded capabilities in terms of temporal and spatial resolution as

compared to 1.5T MRI [90-92]. This allows a shortened examination time and improved image quality [93].

In the context of lung cancer imaging, limited studies that evaluate thoracic MRI image quality and contrast have been reported. Fink et al. evaluated the image quality and lesion contrast of lung MRI using 5 different 2D sequences at 1.5T and 3T under breath-hold with 5 porcine phantoms and 4 healthy subjects [148]. They found that the lesion contrast is higher at 3T. Similar study has been performed by Fable et al. to compare the image quality of 2D dynamic (2D+time) lung MRI with variations of steady-state free- precession (SSFP) and gradient echo (GRE) cine techniques at 1.5T and 3T [84]. They proved that 2D GRE (FLASH 2D) is better than SSFP at 3T with higher lesion signal intensity and contrast.

However, static images only contain the volumetric information at breath-hold and 2D dynamic only provides limited 2D motion information. To obtain volumetric 3D anatomic data during respiration, a time-resolved 3D MRI data acquisition protocol is needed. To the best knowledge of the author, although there are a few 3D dynamic (3D+time) sequences, they have not been evaluated at 3T for lung cancer imaging. Thus, it remains unclear which of these sequences would give better image quality and contrast for imaging lung and lung tumor, and whether they have the ability to capture lung and lung tumor motion. Furthermore, the studies of Fink et al. [148] and Fable et al. [84] only evaluated sequences using porcine phantoms and healthy subjects. It is important to evaluate the performance of the sequences using real lung cancer patients. The objective of this study is to compare a few 4D-MRI sequences at 3T in terms of image quality and their ability to capture lung and lung tumor motion.

3.2.1 Materials and Methodology

3.2.1.1 Magnetic resonance imaging

In order to image the lung in dynamic phases, 4D-MRI sequences with high temporal resolution were selected. As T2 weighted sequences cannot allow for a high enough temporal resolution, we opted for T1 weighted sequences. As recommended by Fink et al., VIBE is good for the depiction of nodules [148] and Fable et al. showed that GRE (FLASH) images have higher lesion signal intensity and contrast at 3T [84]. Echo-sharing (TREAT/TWIST/TRICKS) sequences have also been proved useful for assessing respiratory mechanisms dynamically [149]. So in this study three different 3D dynamic sequences (VIBE, TWIST, and FLASH 3D) were compared for lung MRI. These are volumetric pulse sequences.

VIBE (Volume Interpolated Body Exam) is a spin-echo sequence typically used in the abdomen under breath-hold. Combination with parallel imaging technique improves the temporal resolution of VIBE; hence it can be used for image acquisition under breathing. TWIST is the acronym for Time-resolved angiography With Interleaved Stochastic Trajectories. It is a MR angiography (MRA) sequence that was originally designed to image the vascular tree. TWIST uses keyhole-imaging technique to speed up imaging time. It acquires the central portion of the k-space first then fill in the rest part from subsequent scans [150]. FLASH is short for Fast Low Angle Snap sHot. It is a gradient echo sequence that has a small flip angle and short TR to ensure fast acquisition [151].

All the images were acquired by a whole body 3T MR system (Siemens Trio MRI scanner, Siemens Healthcare, Erlangen, Germany) in coronal plane as

the coronal plane give a clear view of tumor and lungs. Volumes acquired in axial plane usually contain more slices and will increase acquisition time. In order to improve the temporal resolution, parallel imaging algorithm GRAPPA PAT 2 was applied to all the sequences. As there is a tradeoff between temporal and spatial resolution, each sequence was optimized to achieve the highest possible temporal resolution with a reasonable spatial resolution. All sequences generated images with same spatial resolution. Detailed sequence parameters are specified in Table 3-1. A controlled-breathing maneuver was applied during the scans. All subjects were instructed to start by continuous breathing-in for 3 seconds and breathing-out for 3 seconds. Each subject repeated this breathing in and out maneuver for around 25 s (~4 breathing cycles) and in same manner every time. By doing this, a more repeatable breathing manner can be assured for the same subject when scanning using different sequences

Table 3-1 Sequence parameters for 3D dynamic lung MRI

Sequence	TR	TE	BW	FA	FOV	FOV Phase	Matrix	Slice thickness	Temporal Resolution
	(ms)	(ms)	(Hz/px)	(°)	(mm)	(%)	(px)	(mm)	(s/volume)
TWIST	1.71	0.76	1500	10	360	100	128	4	0.9
VIBE	1.93	0.70	1502	10	360	100	128	4	3.5
FLASH 3D	1.96	0.70	1500	10	360	100	128	4	2.9

TWIST: Time-resolved angiography With Interleaved Stochastic Trajectories; **VIBE:** Volume Interpolated Body Exam; **FLASH 3D:** Volumetric Fast Low Angle Shot

Healthy subjects were scanned first followed by lung cancer patients. After studying healthy subjects, the sequence VIBE was taken out of the protocol for

lung cancer patients because of its relatively poor image quality and low temporal resolution in order to shorten the total scanning time for lung cancer patients.

3.2.1.2 Subjects

Institutional Review Board approval was obtained for this study. Ten healthy subjects (7 men, 3 women; mean age: 29.1 years, age range: 21-37 years) and six lung cancer patients (4 men, 2 women; mean age: 64.0, age range: 52-81 years) underwent MR imaging of the lungs. Informed written consent was obtained prior to all examinations. Inclusion criteria were willingness and ability to provide informed consent. The patients are all with non-small cell lung cancer (NSCLC) and were all scheduled for RT. Exclusion criteria were contraindications to MRI including claustrophobia, pacemakers and other implanted electronic devices and pregnancy. There was no presence of other lung diseases such as chronic obstructive pulmonary disease (COPD) or other types of lesions for all the patients. The tumor location of each patient is shown in Figure 3-1.

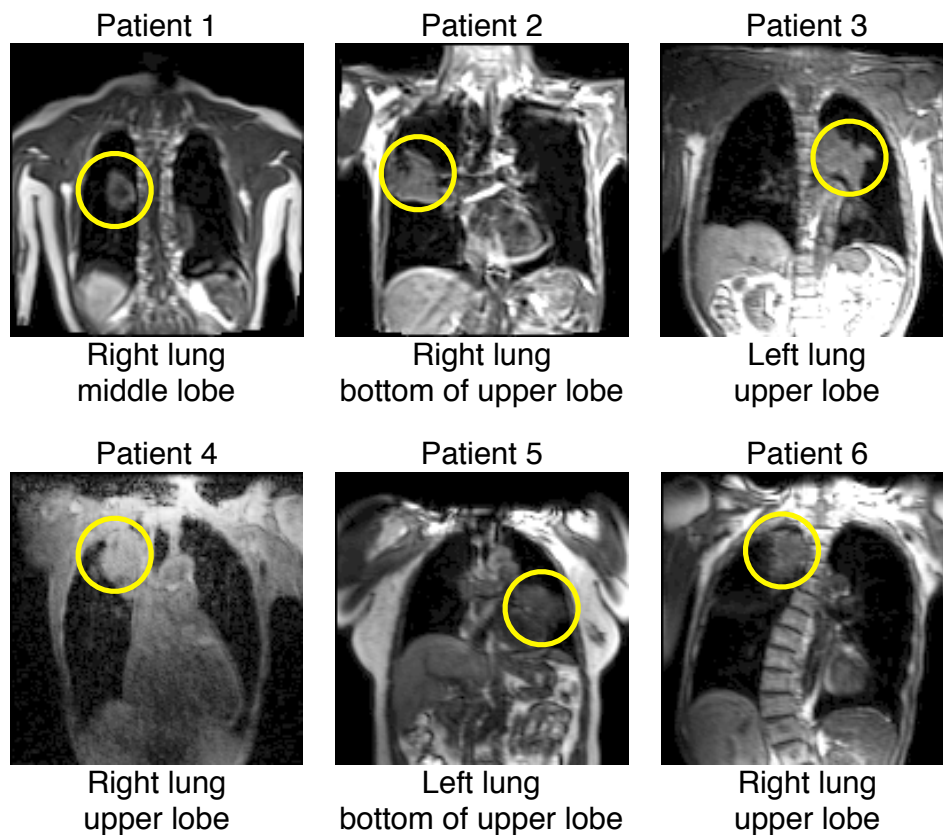


Figure 3-1 Tumor location of each patient. Tumors are marked with yellow circles. Patient 6 is with scoliosis.

3.2.1.3 Image Quality Analysis

To evaluate the sequences, both quantitative and qualitative analyses were performed using the images of healthy subjects and lung cancer patients.

Qualitative analysis

All images were evaluated by two experienced radiologists with 5 years' experience and an experienced radiation oncologist with 6 years' experience in

interpreting MRI. All readers were blinded to sequence type, study time, and subject name, age, and gender. Another independent observer displayed images in random order for each reader. Each reader reviewed all images independently. Criteria for qualitative evaluation were as followed [84]:

- (a) Visualization of structures of interest (SOI) (five-point scale);
- (b) Delineation of anatomical structures (five-point scale);
- (c) Sensitivity of artifacts (three-point scale: 0 = severe artifacts, non-diagnostic; 1 = artifacts, diagnostic; 2 = absence of artifacts). Structures of interests were tumor, heart, liver, spinal cord, chest wall and lungs.

Visualization of SOI aims to evaluate the internal anatomy of the structures of interest. A feature of each structure of interest was identified to best represent its internal anatomy: distinction of (i) myocardium for the heart, (ii) hepatic arteries for the liver, (iii) nerve roots for the spinal cord, (iv) neurovascular bundle for chest wall, and (v) pulmonary vasculature. Table 3-2 summarized the criteria for each scale.

Table 3-2 Criteria for visualization of structures of interest

Scale	Criteria
1	Feature could not be seen
2	Feature was barely seen but its shape could not be identified
3	Location and shape of feature was seen but the distinction from neighboring structures was uncertain
4	Feature was seen and was moderately distinct from neighboring structures
5	Feature was easily and well identified

Delineation of anatomical structures through visual inspection evaluates how distinguishable the boundaries of the SOIs are from the surrounding structures. It was subjectively graded from 1 to 5 as summarized in Table 3-3.

The median and mode of the rankings were calculated to statistically evaluate the sequences. Median presents the value that is middle of all observations while mode shows the most frequently occurring value among the observations.

Table 3-3 Criteria for delineation of anatomical structures

Scale	Criteria
1	Not visible and non-diagnostic structure outline
2	Poor structure outline without sufficient visualization
3	Fairly confident of structure outline
4	Good structure outline sufficient for delineation
5	Excellent structure outline with sharply defined margins

Quantitative analysis

1) Edge sharpness

Edge sharpness is an important parameter of global visual quality of medical images and can be objectively assessed using sigmoid fitting. This technique consists of measuring the edge width, or transition width, using a least-square fitting to a sigmoid function of the form:

$$s(x) = \frac{1}{1 + e^{-a(x-c)}} \quad (3.1)$$

where x is the spatial variable, $s(x)$ is the image intensity, parameter a is inversely proportional to the edge width, and c corresponds to the edge center location. Once the optimal curve parameters are obtained, a measure of rise length is computed and defined as the width from 10% to 90% of the edge height. Based on the assumed shape of the edge given by Equation (3.1), the edge width in pixels is defined by:

$$width = \frac{4.4}{a} \quad (3.2)$$

A significant drop in the edge width can be interpreted as a gain in spatial resolution, as object borders are spread over a lower number of pixels. In this study, the thicknesses of several edges for different organs of interest were computed (Figure 3-2). The same edge locations are used for all sequences to compare their respective sharpness. It is expected that the objective assessment of edge sharpness correlate with the visual evaluation of "Visualization of SOI" and "Delineation of Anatomy".

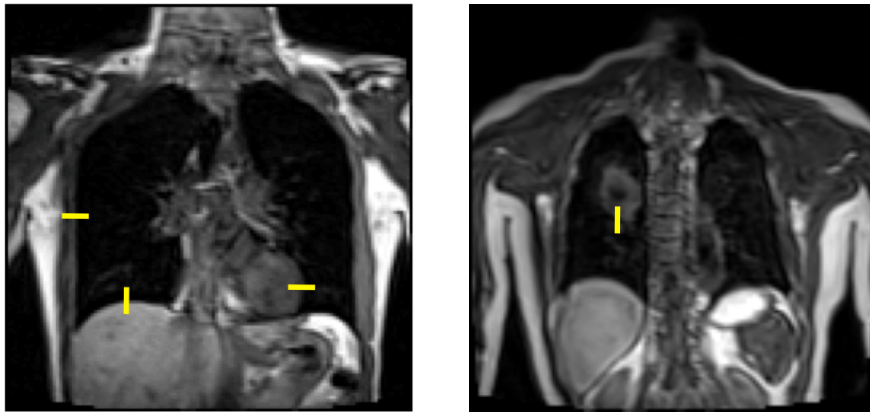


Figure 3-2 Positions that evaluation of edge sharpness took places for different structures of interests (indicated by yellow lines). Structures of interests include tumor, heart, liver, chest wall, and lungs.

2) Local tissue contrast

Because of the non-uniform noise distribution in parallel imaging, the commonly used method to calculate signal-to-noise ratio (SNR) based on noise intensity in background may not be accurate [152]. Local tissue contrast as suggested by [66] was determined in this study by

$$contrast = \frac{S_A - S_B}{S_B} \quad (3.3)$$

where S_A and S_B are the signal intensities of tissue A and B respectively. Tissue B was chosen to be the tissue with less signal intensity so that the calculated contrast will be a positive value. To obtain the contrast value, circular regions with an average number of 50 pixels were positioned in tissues (Figure 3-3). All measurements were performed by an independent examiner.

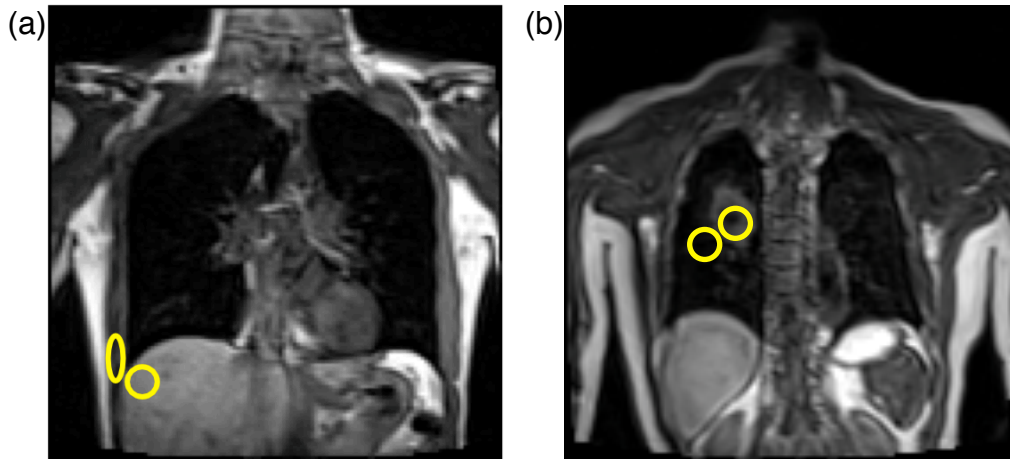


Figure 3-3 Examples of positions that local tissue contrast measurements took places for different organs: (a) chest wall-to-liver; (b) tumor-to-lung

Motion analysis

The 3D trajectory of the tumor centroid and diaphragm domes of right and left lungs is projected in the craniocaudal (CC) direction as major lung and tumor motion are in the CC direction [153]. This is to study whether the 3D dynamic sequences are capable of capturing the lung and tumor motion.

Current RT planning that uses 4D images considers the tumor and other organs positions at all phases between maximum inhalation and exhalation. All the positions at different breathing phases are combined to include all tumor and organ motion [24] (Figure 3-4). In this context, it is important for MRI scans to cover as many positions as possible along the path of tumor and organ motion. Accumulated volume of lungs and tumor was used to represent such ability of sequences in this study. In order to calculate the accumulated volume, the union of segmented volumes of lungs and tumor over 25 s were taken to form the combined segmented volumes. The accumulated volume was calculated by counting the number of voxels contained in this combined segmented volume. It is expected that the higher the temporal resolution, the higher the possibility that the MRI volumes cover more positions of breathing phases, thus the larger the accumulated volume.

The lungs of four representative healthy subjects and both lungs and tumor of six lung cancer patients were segmented using a spatio-temporal based registration-based segmentation scheme (will be discussed in detail in Chapter 4). All the segmented volumes of each subject are combined together to calculate the overall accumulated volume covered during controlled-breathing.

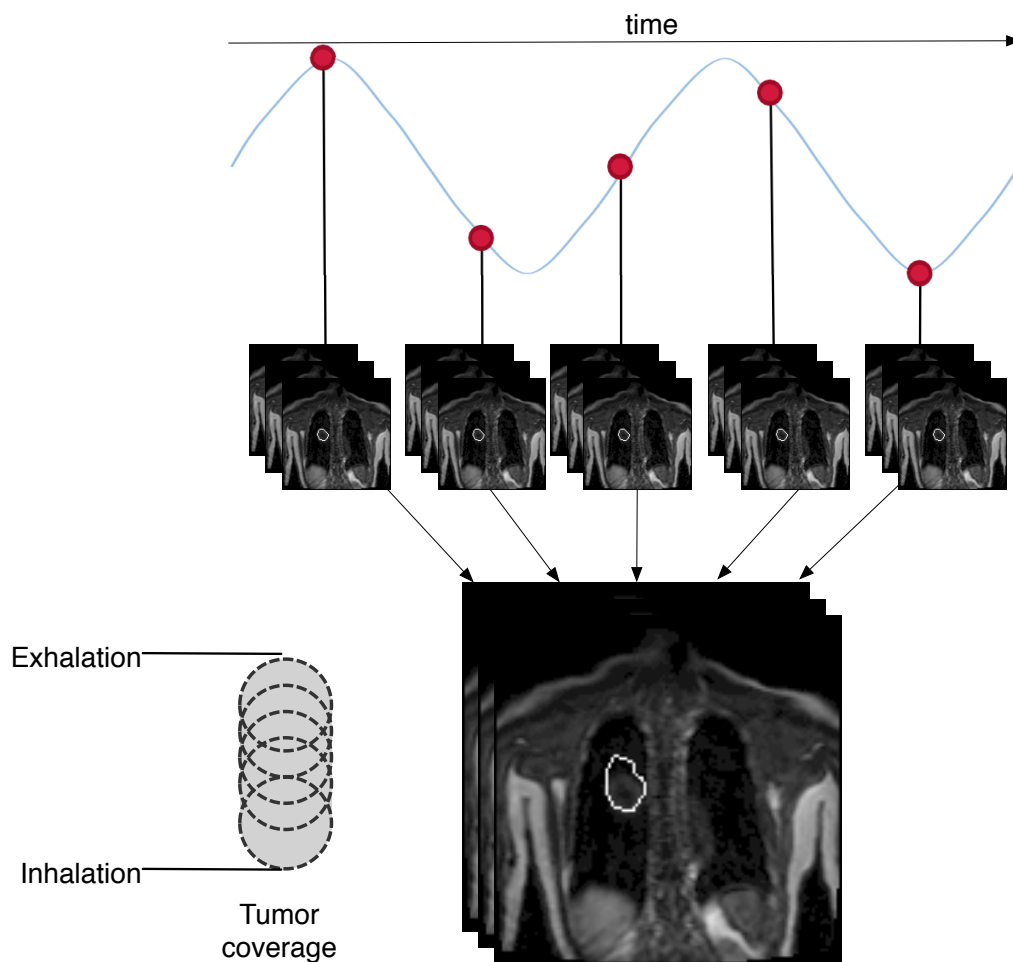


Figure 3-4 Segmented images of tumor during breathing including all the phases are added to form the combined segmented image. Dashed circle in the illustration on the left shows all the tumor position and the grey area presents the accumulated tumor volume.

3.2.2 Study results

3.2.2.1 Image quality analysis

All radiological examinations were performed successfully and there were no adverse events observed. Three 4D-MRI sequences (TWIST, VIBE, and FLASH 3D) were acquired for each healthy subject while two 4D-MRI

sequences (TWIST and FLASH 3D) were acquired for each lung cancer patients.

Qualitative assessments of 4D-MRI sequences are summarized in Table 3-4. All three sequences showed some artifacts that did not affect diagnosis (1/1). FLASH 3D was rated best for heart (3/3) and chest wall (3/3) followed by TWIST, which scored (2/2) and (3/2) for heart and chest wall respectively. FLASH 3D and TWIST were better than VIBE for the visual quality of liver (3/4). VIBE provided best visual quality for lungs (3/4). Flash 3D was preferred for the delineation of liver (3.5/4) and lungs (4/4), though TWIST and VIBE were not far from that. For the delineation of heart, spinal cord, and chest wall all three sequences were rated at the same level with scores of (3/3), (2/2), and (3/3) respectively. In detection of tumor, FLASH 3D was slightly better (3/3). FLASH 3D was also better for the delineation of tumor (3.5/4). Representative images of 4D-MRI sequences are shown in Figure 3-5.

Table 3-4 Qualitative ranking (mean/mode)

	VIBE	TWIST	FLASH 3D
Artifacts	1/1	1/1	1/1
Visualization of SOI			
Tumor	-	3/2	3/3
Heart	2/2	2/2	3/3
Liver	3/3	3/4	3/4
Chest wall	2/2	3/2	3/3
Lungs	3/4	3/3	3/3
Delineation of anatomy			
Tumor	-	2/2	3.5/4
Heart	3/3	3/3	3/3
Liver	3/3	3/3	3/4
Chest wall	3/3	3/3	3/3
Lungs	3/3	3/3	4/4

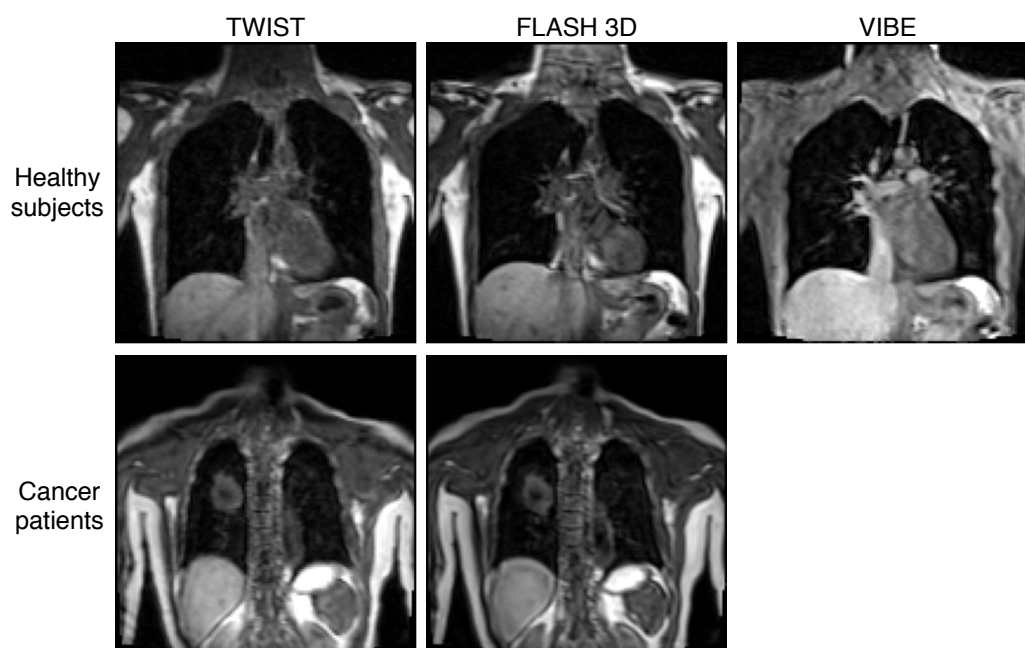


Figure 3-5 4D-MRI lung imaging of normal subject (upper row) and lung cancer patient (lower row) using three different sequences: TWIST, FLASH 3D, and VIBE. VIBE was not acquired for the patients to reduce scan time.

Edge widths between SOIs and lungs of 3D dynamic sequences are shown in Table 5. FLASH 3D had the smallest edge widths for tumor (1.01 mm), heart (4.78 mm), and chest wall (4.29 mm). Images acquired by TWIST showed best edge sharpness for liver (4.37). Images acquired by VIBE were the worst among all the sequences in terms of edge sharpness of all SOIs (heart: 6.31 mm, liver: 9.00 mm, chest wall: 6.31 mm).

Table 3-5 Edge width (mm/pixels) measurements

	VIBE	TWIST	FLASH 3D
Tumor	-	1.31/0.47	1.01/0.36
Heart	6.31/2.24	5.77/2.05	4.78/1.70
Liver	9.00/3.20	4.37/1.55	4.96/1.76
Chest wall	6.31/2.24	5.24/1.86	4.29/1.53

The local tissue contrasts for 3D dynamic sequences are summarized in Table 3-6. FLASH 3D showed the highest contrast for heart-to-liver (0.95), chest wall-to-liver (1.76), heart-to-lung (22.18), chest wall-to-lung (23.70), liver-to-lung (33.68), and tumor-to-lung (11.69). TWIST showed slightly less contrast than FLASH 3D. VIBE is the worst of all three in terms of local tissue contrasts.

Table 3-6 Local tissue contrast measurements

	VIBE	TWIST	FLASH 3D
Heart-Liver	0.35	0.76	0.95
Chest wall-Liver	0.55	1.34	1.76
Heart-Lung	9.97	17.26	22.18
Chest wall-Lung	10.00	17.18	23.70
Liver-Lung	17.12	23.46	33.68
Tumor-Lung	-	8.65	11.69

3.2.2.2 Motion analysis

The displacement of the diaphragm dome of both lungs in CC direction is shown in Figure 3-6 and Figure 3-7 for four representative healthy subjects and six lung cancer patients respectively. The tumor trajectory is shown in Figure 3-8. In 25 s of image acquisition, approximately 3 to 6 breathing cycles were recorded. One can see that tumor of Patient 1 has the highest mobility while that of Patient 4 has the lowest. With a high temporal resolution, TWIST clearly displayed a continuous trajectory of diaphragm and tumor motion. FLASH 3D

and VIBE are proved to be unable to present the path of diaphragm and tumor motion. However, they almost covered the two extreme positions at maximum exhalation and inhalation.

The accumulated volumes of left lung, right lung, and tumor of six lung cancer patients and four healthy subjects are presented in Table 3-7, Table 3-8, and Table 3-9 respectively. Due to the relative high temporal resolution, segmented images of TWIST showed the largest accumulated volume of left lung (1503.2 ± 408.4 ml), right lung (1800.0 ± 350.2 ml), and tumor (164.1 ± 83.5 ml). If we consider TWIST to be the reference, segmented images of FLASH 3D showed a reduction of 126.9 ± 101.1 ml ($8.4 \pm 5.4\%$) for left lung and 183.5 ± 184.2 ml ($7.7 \pm 6.0\%$) for right lung. A small difference was noticed for the accumulated volume of tumor between TWIST and FLASH 3D, with a difference of 4.3 ± 5.2 ml ($2.4 \pm 2.4\%$). For VIBE, the accumulated volumes were even smaller, with a larger difference of 181.8 ± 93.6 ml ($11.1 \pm 4.2\%$) for left lung and 279.8 ± 55.3 ml ($14.6 \pm 1.1\%$) for right lung from those of TWIST.

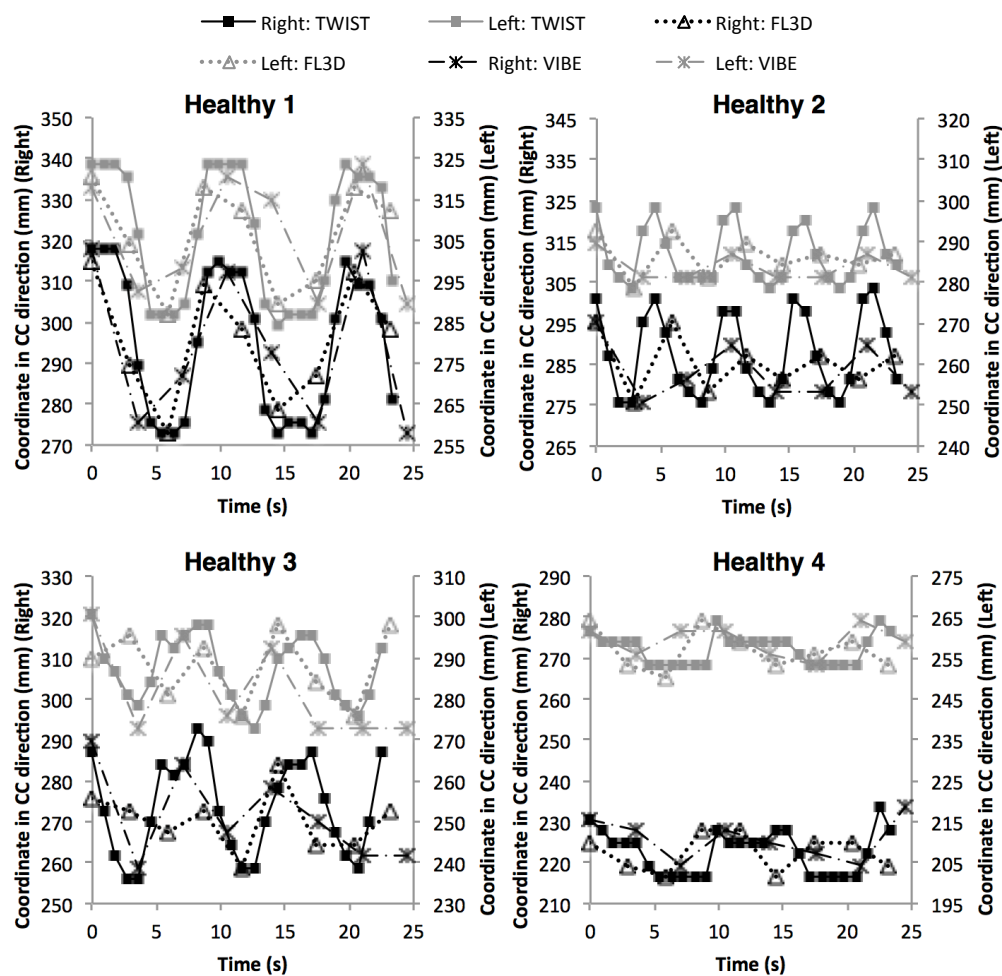


Figure 3-6 Diaphragm dome trajectory of left and right lungs presented by TWIST, FLASH 3D (FL3D in short), and VIBE in CC direction of four healthy subjects.

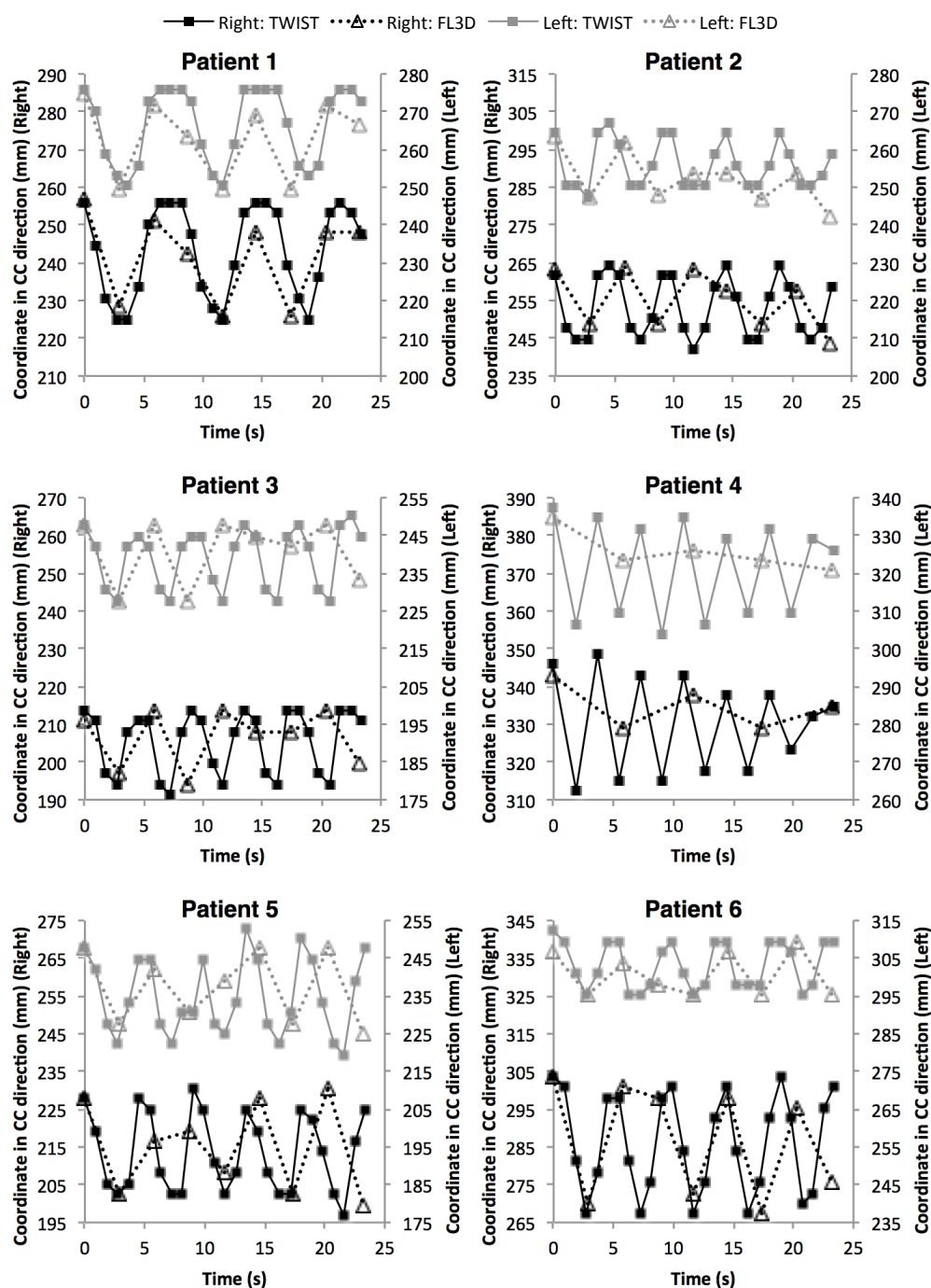


Figure 3-7 Diaphragm dome trajectory of left and right lungs presented by TWIST, FLASH 3D (FL3D in short), and VIBE in CC direction of six lung cancer patients. VIBE was not acquired for the patients to reduce scan time.

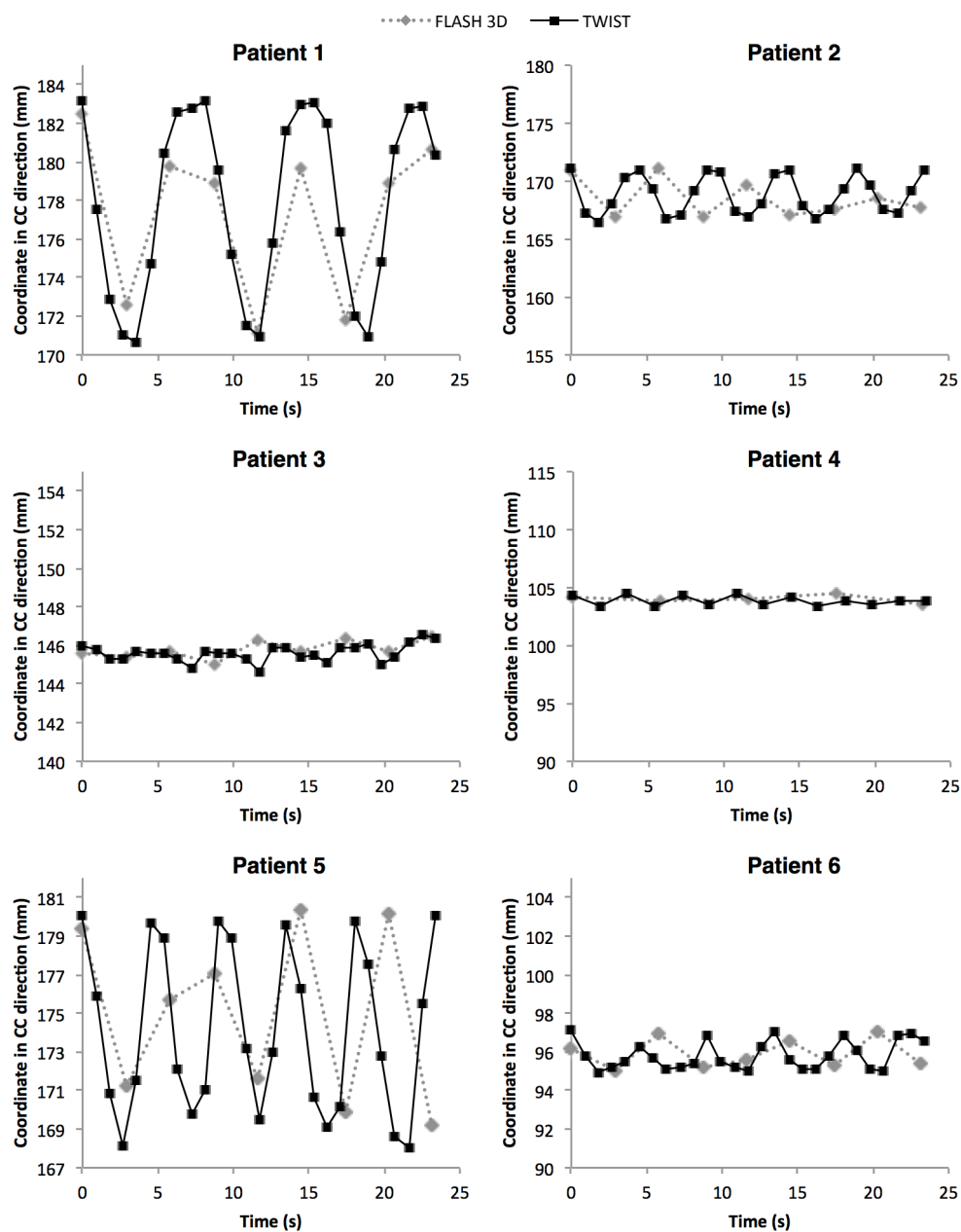


Figure 3-8 Tumor trajectory presented by FLASH 3D and TWIST in CC direction of six lung cancer patients.

Table 3-7 Accumulated left lung volume of four healthy subjects and six lung cancer patients over 3 to 5 breathing cycles. V_{TWIST} , V_{FLASH} , and V_{VIBE} represent the accumulated volume for TWIST, FLASH 3D, and VIBE respectively. The unit for all the volumes is mL. ΔV_{FLASH} and ΔV_{VIBE} are calculated as $V_{TWIST} - V_{FLASH}$ and $V_{TWIST} - V_{VIBE}$ respectively. $\% \Delta V_{FLASH}$ and $\% \Delta V_{VIBE}$ are calculated as $\Delta V_{FLASH}/V_{TWIST}$ and $\Delta V_{VIBE}/V_{TWIST}$ respectively.

	V_{TWIST} (ml)	V_{FLASH} (ml)	V_{VIBE} (ml)	ΔV_{FLASH} (ml)	$\% \Delta V_{FLASH}$	ΔV_{VIBE} (ml)	$\% \Delta V_{VIBE}$
Healthy 1	1440.4	1432.8	1362.5	7.6	0.5	77.9	5.4
Healthy 2	1934.7	1713.3	1634.4	221.5	11.5	300.3	15.5
Healthy 3	1822.8	1626.8	1622.7	195.9	10.7	200.0	11.0
Healthy 4	1203.0	1114.2	1054.2	88.8	7.4	148.8	12.4
Patient 1	972.1	861.4		110.7	11.4		
Patient 2	1777.6	1751.2		26.4	1.5		
Patient 3	1064.2	970.5		93.7	8.8		
Patient 4	1800.2	1454.6		345.6	19.2		
Patient 5	1018.2	944.9		73.3	7.2		
Patient 6	1998.5	1892.6		105.9	5.3		
Average	1503.2	1376.2	1418.5	126.9	8.35	181.8	11.1
(stdev)	(408.4)	(376.7)	(273.4)	(101.1)	(5.4)	(93.6)	(4.2)

Table 3-8 Accumulated right lung volume of four healthy subjects and six lung cancer patients over 3 to 5 breathing cycles.

	V_{TWIST} (ml)	V_{FLASH} (ml)	V_{VIBE} (ml)	ΔV_{FLASH} (ml)	$\% \Delta V_{FLASH}$	ΔV_{VIBE} (ml)	$\% \Delta V_{VIBE}$
Healthy 1	1841.4	1821.5	1602.4	19.9	1.1	238.9	13.0
Healthy 2	2267.4	2015.0	1916.9	252.4	11.1	350.5	15.5
Healthy 3	2060.8	1866.9	1763.7	193.9	9.4	297.1	14.4
Healthy 4	1525.2	1345.0	1292.5	80.3	11.8	232.7	15.3
Patient 1	1274.5	1206.8		67.7	5.3		
Patient 2	2075.4	2041.0		34.5	1.7		
Patient 3	1534.9	1477.9		567.0	3.7		
Patient 4	2064.3	1628.7		435.6	21.1		
Patient 5	1347.5	1259.9		87.6	6.5		
Patient 6	2008.4	1912.0		96.4	4.8		
Average	1800.0	1657.5	1643.9	183.5	7.7	279.8	14.6
(std)	(350.2)	(316.6)	(267.1)	(184.2)	(6.0)	(55.3)	(1.1)

Table 3-9 Accumulated tumor volume of six lung cancer patients over 3 to 6 breathing cycles.

	V_{TWIST} (ml)	V_{FLASH} (ml)	ΔV_{FLASH} (ml)	$\% \Delta V_{FLASH}$
Patient 1	63.6	63.5	0.1	0.2
Patient 2	203.4	202.6	0.8	0.4
Patient 3	101.0	98.0	3.0	3.0
Patient 4	198.4	197.3	1.1	0.6
Patient 5	292.9	279.4	13.5	4.6
Patient 6	125.3	118.0	7.3	5.8
Average	164.1	159.8	4.3	2.4
(stdev)	(83.5)	(80.5)	(5.2)	(2.4)

3.2.3 Study discussion

With its rapid development in recent years, MRI of the lung has shown potential for broad clinical applications. Lung nodules larger than 4–5 mm in diameter can be easily detected by MRI with comparable sensitivity to CT [154, 155]. For lung cancers of the superior sulcus (Pancoast tumor), MRI is mandatory to delineate tumor infiltration of the chest wall, brachial plexus and vasculature, all of which would strongly influence resection margins and gross tumor volume for RT [156]. The planning of RT of lung cancer patients would also benefit from dynamic MRI by accurate calculation of the target volume without the use of ionizing radiation.

The focus of this study is on the evaluation of 4D-MRI sequences for the imaging of the chest and lung tumor at 3T. Generally, the results of qualitative analysis and quantitative analysis matched well. Images with sharper edges and higher local tissue contrast were also rated with higher score by independent observers. The delineation of structures were rated the same for TWIST and

VIBE sequences although TWIST images have sharper edges. This is largely due to the relatively low image resolution. Though large differences between edge widths of images were obtained in physical size (mm), the differences are less than 2 pixels for pixel size. This makes it hard for observers to distinguish the differences between the two images when they were evaluating based on delineation of target structures.

FLASH 3D has the best image quality and local tissue contrast among three sequences at 3T. Fabel et al. [84] found that contrast and image quality of GRE sequence (FLASH 2D) improved at 3T. In this study, we further proved that 3D GRE sequence (FLASH 3D) is also favored at 3T. FLASH 3D also showed sharpest edge for tumor, heart, and chest wall except for liver, while TWIST achieved better edge sharpness at liver/lung interface (Table 5). This could be due to the relatively low temporal resolution of FLASH 3D. As the liver/lung interface has the most prominent motion, it is reasonable to expect that faster sequence will have less motion artifact which will result in sharper edge.

TWIST has a slightly poorer image quality (though still acceptable) but faster acquisition time as compared to FLASH 3D. With a 0.9 s/volume acquisition, which is 3 times faster than FLASH 3D, TWIST is able to capture the lung and tumor motion within a breathing cycle, which is typically 5s duration. The accumulated volume of segmented images over 3 to 6 breathing cycles showed that TWIST had the largest accumulated volume, which indicates that TWIST was able to cover more positions along the motion path of diaphragm and tumor. This is important for RT. Though the accumulated lung volume of FLASH 3D is much less than that of TWIST, the accumulated tumor volume of FLASH 3D is similar to that of TWIST in a 25 s' acquisition time.

This is because the magnitude of tumor motion is much smaller than that of diaphragm motion. FLASH 3D is thus capable of detecting the extreme positions of tumor, although it is not sufficient to cover the range of diaphragm motion.

The reason why TWIST is capable of fast acquisition is that TWIST incorporates a keyhole technique for temporal acceleration. Conventionally, every point in k-space ($k_x k_y k_z$) is sampled. The keyhole technique manipulates conventional k-space sampling strategy by dividing $k_y k_z$ space into a central and a peripheral sector (Figure 3-9) [157, 158]. The central sector defines the main contrast in the image while the peripheral sector defines the detail information in the image. The temporal acceleration is achieved by alternatively acquiring the full central sector and a portion of the peripheral sector (e.g. half of the peripheral sector); data can be borrowed from temporally neighboring peripheral sector acquisitions (Figure 3-10). The temporal resolution is defined as the repetition time of the center sector. As a result, the acquisition time is shortened because the time required for a portion of the peripheral sector is clearly shorter than that for a full one.

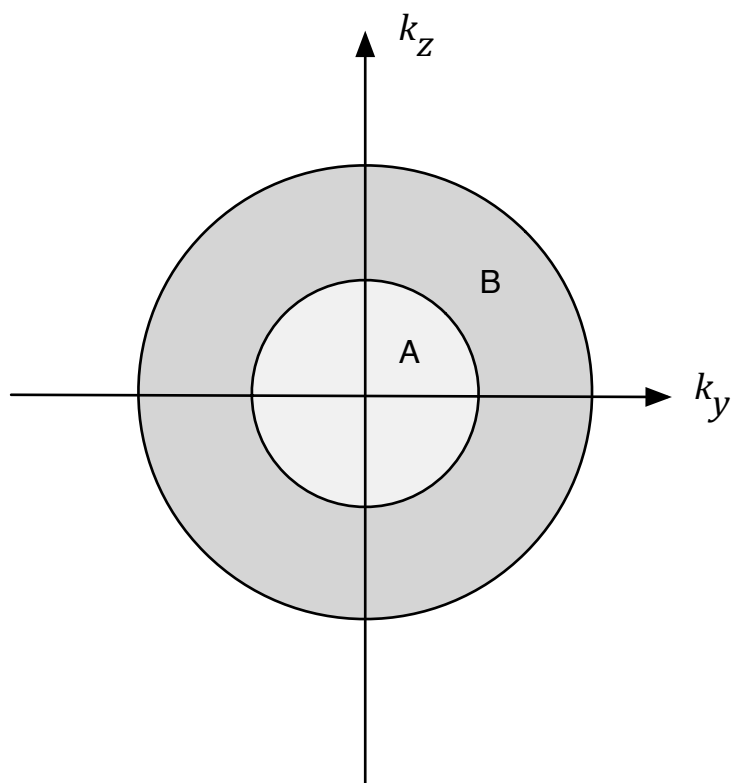


Figure 3-9 k-space is divided into two sectors: the central sector (A) and the peripheral sector (B).

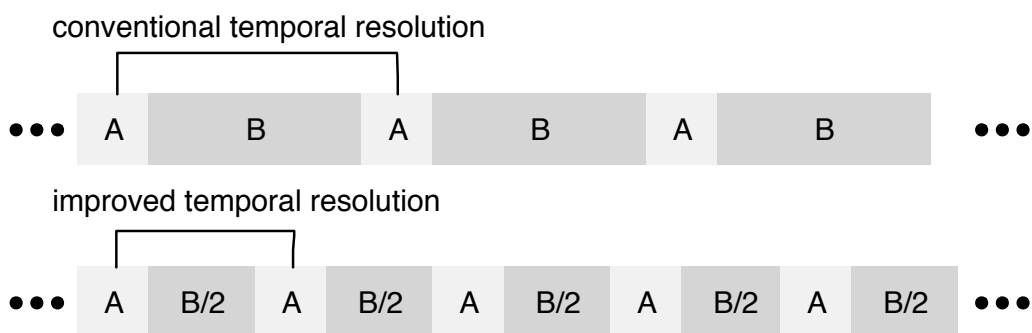


Figure 3-10 Conventionally, the temporal resolution is $A+B$. Keyhole technique improves the temporal resolution by sampling B half as frequently thus the improved temporal resolution is $A+B/2$.

The age group of healthy subjects (29.1 years) and lung cancer patients (64.0 years) were not matched. This is due to the difficulty in volunteer recruitment. However, in this study, the sequences are compared within the subject and not across subjects. Further more, it is not the scope of this study to compare the groups of healthy subjects and lung cancer patients. The effect of the unmatched age group between healthy subjects and lung cancer patients are minimum. A limitation of the study is that the statistical power of the lung cancer patient dataset might be insufficient. Nevertheless, in this study coherent results were shown for the six patients in this study. It is expected that similar results can be observed on other patients. We can clearly observe and evaluate the strengths and weaknesses of the different MRI sequences. It would also be interesting to compute the contrast between tumor and adjacent other than lung tissues (e.g. heart, liver, and chest wall). However, the tumors in our data series were not close to other organs. We will focus on the interface between tumor and other organs in the future work.

3.2.4 Study conclusion

In conclusion, this study has compared three 3D dynamic sequences performed on clinical MRI scanners for imaging of the lungs at 3T. FLASH 3D produces the best image quality whereas TWIST has good image quality at a faster temporal resolution, which is capable of showing the motion path of tumor.

3.3 4D-imaging of lung cancer: comparison of 4D-MRI and 4D-CT based on tumor volume and motion

As mentioned earlier, CT is the current standard modality for RT. In order to investigate the potential for 4D-MRI to serve as an alternative modality to be used in 4D-RT, it is necessary to compare 4D-MRI with 4D-CT. Biederer et al. evaluated how size and displacement of artificial pulmonary nodules are reproduced using 4D-CT and 4D-MRI at 1.5T using porcine phantoms [86]. They found that tumor sizes are exactly reproduced using 4D-CT but overestimated using 4D-MRI due to its limited temporal and spatial resolution. The tumor displacement was underestimated by both 4D-MRI and 4D-CT.

However, to fully evaluate the performance of 4D-MRI on lung cancer, phantom study is insufficient. 4D-MRI of real lung cancer patients needs to be studied. Recent studies showed that quantitative assessment of the lung volume during breathing could be derived from 4D-MRI data and results correlate well with spirometric measurements [159]. In this study, the focus is on the tumor volume and motion of 4D-MRI imaging of lung cancer patients. Such information cannot be acquired using lung function tests such as spirometry. Since 4D-CT currently is the gold standard for RT, 4D-CT images serve as the ground truth for 4D-MRI to compare with. The aim of this study is to compare 4D-MRI and 4D-CT from the same patient in terms of tumor volume and motion trajectory and coverage.

3.3.1 Materials and methodology

3.3.1.1 4D-MRI and 4D-CT Data

As discussed in Section 3.2, 4D-MRI using TWIST sequence is capable of showing the motion path of tumor while displaying a good image quality. Hence TWIST is selected in this study. The 4D-MRI volumes acquired by TWIST sequence at 3T of the same 6 lung cancer patients were used in this study. The specifications of the acquired images are the same as in Section 3.2.

Thoracic 4D-CT datasets of the same 6 lung cancer patients acquired for their RT planning were analysed to serve as the ground truth. Images were acquired using a large bore, 16-slice dedicated CT simulator with respiratory correlated imaging (Brilliance CT Big Bore, Philips, Eindhoven, The Netherlands). Each 4D CT dataset comprises a series of 3D volumes in axial plane at different phases of the breathing cycle, with a total of nine to ten phases across a breathing cycle. Hence, there are nine to ten 3D volumes for each patient. Each of the 3D volume covers the whole thorax. The in-plane resolution ranges from $0.57 \text{ mm} \times 0.57 \text{ mm}$ to $1.17 \text{ mm} \times 1.17 \text{ mm}$. The through-plane resolution ranges from 3 mm to 5 mm. The details of the 4D-CT volumes are listed in Table 3-10.

Table 3-10 Specifications of the 4D-CT dataset for each patient

	Matrix	Spatial resolution (mm^3)
Patient 1	$1024 \times 1024 \times 132$	$0.57 \times 0.57 \times 3.00$
Patient 2	$512 \times 512 \times 90$	$1.16 \times 1.16 \times 5.00$
Patient 3	$512 \times 512 \times 80$	$1.17 \times 1.17 \times 5.00$
Patient 4	$512 \times 512 \times 103$	$1.18 \times 1.18 \times 5.00$
Patient 5	$512 \times 512 \times 127$	$1.19 \times 1.19 \times 3.00$
Patient 6	$512 \times 512 \times 85$	$1.14 \times 1.14 \times 5.00$

3.3.1.2 Sorting MRI volumes into breathing phases

The 4D-MRI and 4D-CT used in this study were acquired at two different sessions. The acquisition scheme and breathing maneuver for 4D-MRI and 4D-CT are different as well. Thus, in order to compare 4D-MRI with 4D-CT, it is necessary to sort MRI volumes into breathing phases with respect to the phases in 4D-CT.

In this study, the height of tumor-bearing lung is used to sort the MRI volumes. It is based on the fact that the diaphragmatic movement is the principal movement in the chest and all the lung-related structures move almost synchronously [160], which indicates that once the lung height of two thoracic images are the same, structures within the lung (blood vessels, tumor, etc.) are at the same position. For each volume of 4D-CT and 4D-MRI, coronal plane crossing the trachea is first located. Though 4D-CT volumes are acquired in the axial plane, it is viewed in the coronal plane for convenience. The lung height is measured from the apex of the lung to the diaphragmatic dome in the cranialcaudal (CC) plane in the middle of the hemithorax [161] (Figure 3-11).

For each MRI volume, the breathing state (i.e. inhalation or exhalation) is first identified by comparing the lung height with adjacent volumes. Subsequently the lung height of this MRI volume is compared to that of 4D-CT volumes of similar lung height that are in the same breathing state. The two adjacent CT volumes that bound the MRI volume are then located (Figure 3-12). The corresponding breathing phase of the MRI volume is calculated as:

$$P_{MRI} = \frac{(H_{MRI} - H_{CT}^{low})(P_{CT}^{high} - P_{CT}^{low})}{(H_{CT}^{high} - H_{CT}^{low})} + P_{CT}^{low} \quad (3.4)$$

where P_{MRI} is the breathing phase of the MRI volume, P_{CT}^{high} is the phase of CT volume at higher phase, P_{CT}^{low} is the phase of CT volume at lower phase, H_{MRI} is the lung height of the MRI volume, H_{CT}^{high} is the lung height of CT volume at higher phase, H_{CT}^{low} is the lung height of CT volume at lower phase. If the lung height of the MRI volume is equal to a CT volume at the same breathing state, the breathing phase of the CT volume is assigned to the MRI volume.

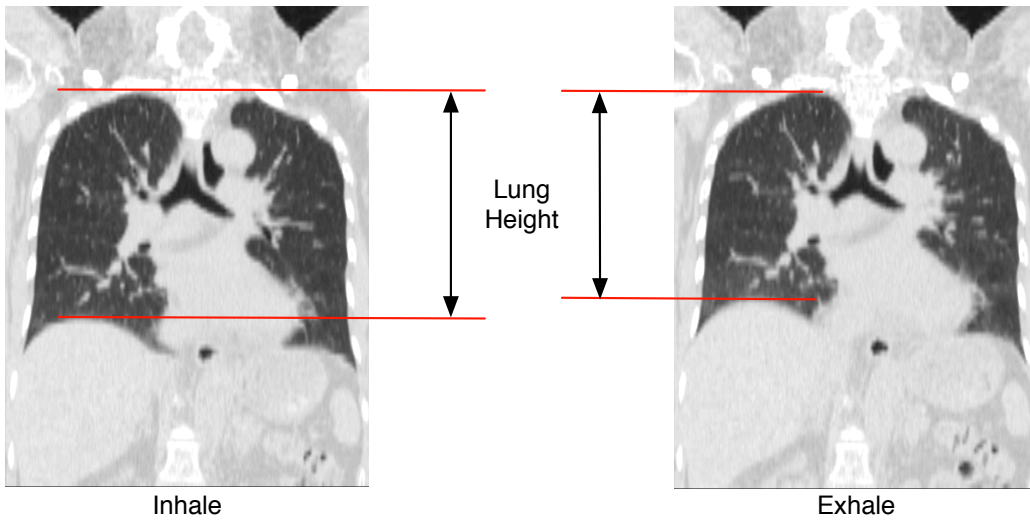


Figure 3-11 Illustration of the measurement of lung height using 4D-CT images. The lung height is measured from the apex of the lung to the diaphragmatic dome in CC direction in the coronal slice that crosses the trachea.

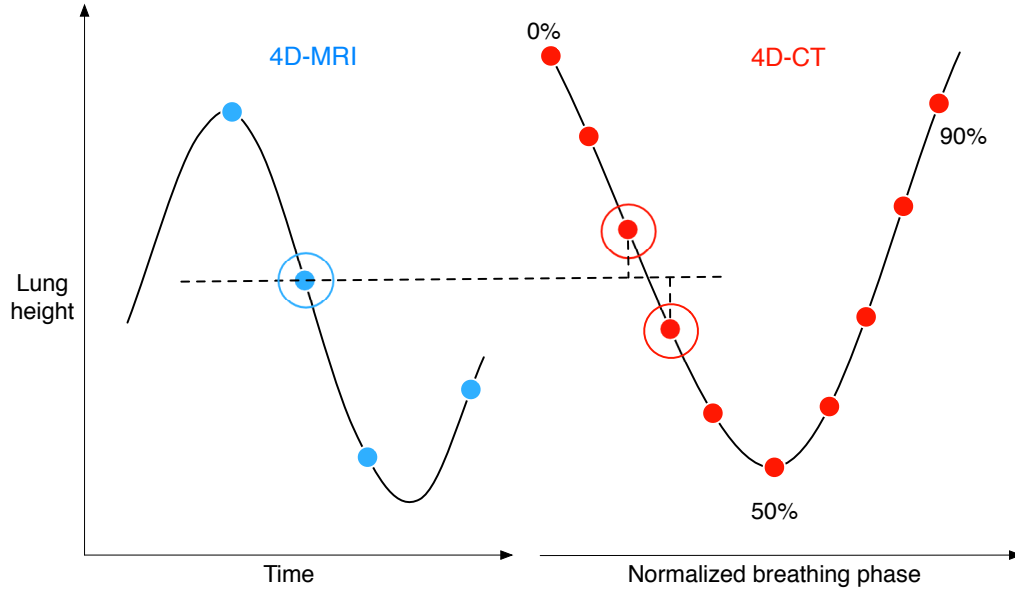


Figure 3-12 Illustration of sorting a 4D-MRI volume into corresponding breathing phase.

3.3.1.3 Comparison of tumor volume and mobility

For all the 4D-MRI and 4D-CT volumes of all patients, tumor was segmented using a spatio-temporal based registration-based segmentation scheme developed in Chapter 4.

Since lung tumor deforms and rotates during normal respiration [20, 21], it is important to compare the tumor volume at the same breathing phase. Thus, tumor volumes at maximum exhalation phase (V_{ME}) of sorted 4D-MRI and 4D-CT were calculated using segmented volumes for each patient.

Similar to Section 3.2, the accumulated volume of tumor was used to represent whether 4D-MRI is able to cover the motion coverage of the tumor as 4D-CT does. For each patient, the union of segmented tumor volumes for all

the sorted MRI volumes was taken to form the combined segmented volume. Using the combined segmented volume, the accumulated volume (V_{Acc}) was then calculated. The same was done to 4D-CT volumes. The accumulated volumes derived using 4D-MRI and 4D-CT were then compared.

The 3D trajectories of the tumor centroid of all sorted MRI volumes and 4D-CT were projected in the CC direction as major lung motion and tumor mobility is in the CC direction. This is to study whether there is any difference in describing tumor motion between 4D-MRI and 4D-CT.

3.3.2 Study results

Samples images of 4D-MRI and 4D-CT volumes of each patient are shown in Figure 3-13. For each patient, nine to eleven MRI volumes were successfully sorted into phases with respect to the phases in 4D-CT.

Tumor volumes of sorted 4D-MRI volume and 4D-CT volume at maximum exhalation phase are summarized in Table 3-11. The tumor volume captured by 4D-CT had an average value of 118.1 ± 59.8 ml while the average volume derived using 4D-MRI is 116.8 ± 57.0 ml. Difference was small between the two modality, with an average value of 3.2 ± 2.0 ml ($3.3 \pm 2.4\%$). In order to determine whether the observations in 4D-MRI differs a lot from those in 4D-CT, a paired t -test is performed as it is known for determining of two sets of data are significantly different from each other. The hypothesis is that there is significant difference between the observations in 4D-MRI and 4D-CT. The paired t -test was applied using SPSS 18.0 for Windows [162]. Results showed

that there is no significant difference between the two modalities in terms of representation tumor volume ($p = 0.46$).

The accumulated tumor volumes of sorted 4D-MRI volumes and 4D-CT volumes over one breathing cycle are listed in Table 3-12. The accumulated tumor volume presented by 4D-CT had an average value of 139.7 ± 64.3 ml while that derived using 4D-MRI is 143.6 ± 64.6 ml. Difference was small between the two modalities, with an average difference of 5.4 ± 5.1 ml ($4.5 \pm 5.8\%$). There is no significant difference between the two modalities (paired t-Test, $p = 0.19$).

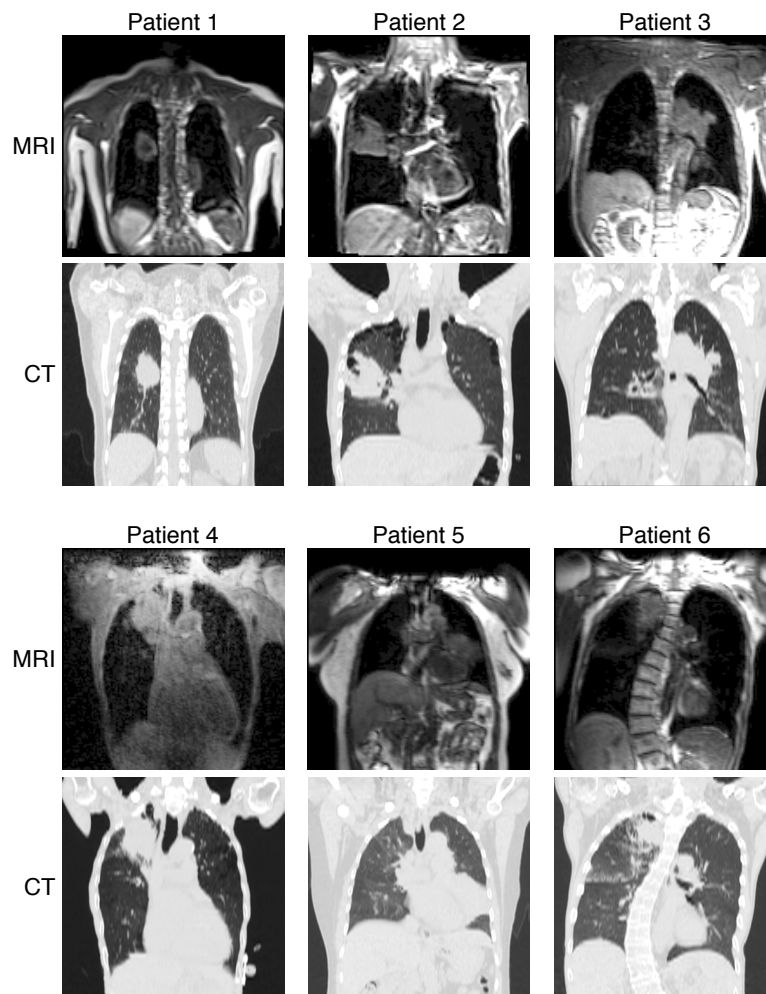


Figure 3-13 Sample images of 4D-MRI and 4D-CT of 6 patients

Table 3-11 Tumor volumes of sorted MRI volume and 4D-CT volume at maximum exhalation phase of six lung cancer patients. V_{ME}^{CT} and V_{ME}^{MRI} represent the tumor volume for CT and MRI respectively. ΔV_{ME}^{MRI-CT} is calculated as $V_{ME}^{MRI} - V_{ME}^{CT}$. $\% \Delta V_{ME}^{MRI-CT}$ is calculated as $\Delta V_{ME}^{MRI-CT} / V_{ME}^{CT}$. Negative value means MRI has underestimated the tumor volume.

	V_{ME}^{CT}	V_{ME}^{MRI}	ΔV_{ME}^{MRI-CT}	$ \Delta V_{ME}^{MRI-CT} $	$ \% \Delta V_{ME}^{MRI-CT} $
	(ml)	(ml)	(ml)	(ml)	
Patient 1	37.4	38.8	1.4	1.4	3.7
Patient 2	194.8	189.4	-5.4	5.4	2.8
Patient 3	110.5	107.1	-3.3	3.3	3
Patient 4	161.4	161.7	0.2	0.2	0.1
Patient 5	141.1	136.4	-4.65	4.65	3.3
Patient 6	63.4	67.7	4.3	4.3	6.7
Average	118.1	116.8		3.2	3.3
(stdev)	(59.8)	(57.0)		(2.0)	(2.4)

Table 3-12 Accumulated tumor volumes of sorted MRI volumes and 4D-CT volumes over one breathing cycle. V_{Acc}^{CT} and V_{Acc}^{MRI} represent the accumulated tumor volume for CT and MRI respectively. ΔV_{Acc}^{MRI-CT} is calculated as $V_{Acc}^{MRI} - V_{Acc}^{CT}$. $\% \Delta V_{Acc}^{MRI-CT}$ is calculated as $\Delta V_{Acc}^{MRI-CT} / V_{Acc}^{CT}$. Negative value means MRI has underestimated the accumulated tumor volume.

	V_{Acc}^{CT}	V_{Acc}^{MRI}	ΔV_{Acc}^{MRI-CT}	$ \Delta V_{Acc}^{MRI-CT} $	$ \% \Delta V_{Acc}^{MRI-CT} $
	(ml)	(ml)	(ml)	(ml)	
Patient 1	48.8	50.0	1.2	1.2	2.5
Patient 2	218.5	221.2	2.7	2.7	1.2
Patient 3	113.0	109.0	-4.0	4.0	3.6
Patient 4	168.8	170.9	2.1	2.1	1.3
Patient 5	192.5	199.3	6.8	6.8	3.5
Patient 6	96.7	111.3	14.6	14.6	15.1
Average	139.7	143.6		5.3	4.5
(stdev)	(64.3)	(64.6)		(5.1)	(5.8)

Table 3-13 lists the tumor motion coverage in CC direction captured by sorted 4D-MRI volumes and 4D-CT volumes over one breathing cycle. The tumor volume moving range captured by 4D-CT had an average value of 2.3 ± 2.6 mm while that displayed in 4D-MRI was 2.3 ± 2.4 mm. Difference is small between the two modalities, with an average difference of 0.2 ± 0.2 mm ($14.6 \pm 9.5\%$). There is no significant difference between the two modalities (paired t-Test, $p = 0.47$).

The tumor trajectories in CC direction of sorted 4D-MRI volumes and 4D-CT volumes over one breathing cycle for three lung cancer patients are displayed in Figure 3-14. The tumor of Patient 1 displayed the highest mobility while that of Patient 3 has the lowest. Visually the tumor motion path of sorted MRI volumes matches well to that of 4D-CT volumes.

Table 3-13 Tumor motion coverage of sorted MRI volumes and 4D-CT volumes in CC direction over one breathing cycle. S^{CT} and S^{MRI} represent the tumor moving range for CT and MRI respectively. ΔS^{MRI-CT} is calculated as $S^{MRI} - S^{CT}$. $\% \Delta S^{MRI-CT}$ is calculated as $\Delta S^{MRI-CT} / S^{CT}$. Negative value means MRI has underestimated the tumor motion coverage.

	S^{CT}	S^{MRI}	ΔS^{MRI-CT}	$ \Delta S^{MRI-CT} $	$ \% \Delta S^{MRI-CT} $
	(mm)	(mm)	(mm)	(mm)	
Patient 1	6.3	5.7	-0.6	0.6	8.9
Patient 2	0.6	0.7	0.1	0.1	9.8
Patient 3	0.1	0.1	-0.0	0.0	22.2
Patient 4	0.1	0.1	0.0	0.0	22.2
Patient 5	4.5	4.6	0.1	0.1	1.9
Patient 6	2.1	2.5	0.5	0.5	22.6
Average	2.3	2.3		0.2	14.6
(stdev)	(2.6)	(2.4)		(0.2)	(9.5)

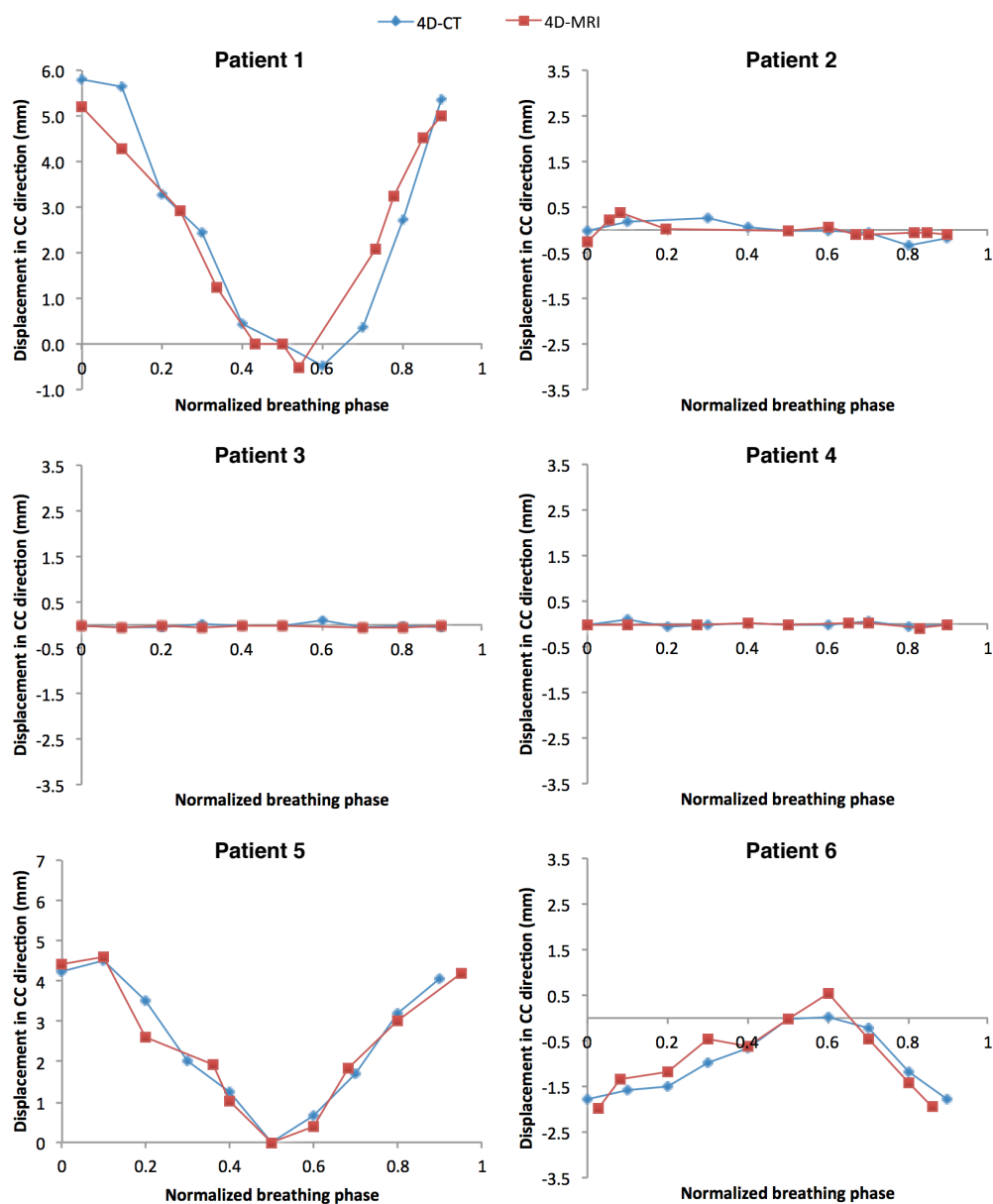


Figure 3-14 Comparison of tumor trajectories in CC direction between sorted 4D-MRI volumes and 4D-CT volumes over one breathing cycle.

3.3.3 Study discussion

This study compared 4D-MRI with 4D-CT in terms of tumor volume and motion trajectory and coverage. In order to compare 4D-MRI and 4D-CT that are not acquired in the same session, a method to sort 4D-MRI volumes into corresponding breathing phases in 4D-CT system without the use of external breathing signal was developed. It allows the direct quantitative comparison between 4D-MRI and 4D-CT. The accuracy of this method is further evaluated in Chapter 5.

Results showed that there is no significant difference between 4D-MRI and 4D-CT in terms of tumor volume. This is inconsistent with the findings by Biederer et al [86]. They scanned 4 porcine lung phantoms with artificial tumors under a ventilation rate of 8 cycles per minute using 4D-CT (slice thickness: 0.8-1.5 mm; temporal resolution: 0.5 s/volume) and 4D-MRI (1.5T; echo-shared FLASH 3D, similar to TWIST used in this study; spatial resolution: $2.7 \text{ mm} \times 2.7 \text{ mm} \times 4.0 \text{ mm}$; temporal resolution: 1.4 s/volume). In their work, the tumor sizes were exactly reproduced with 4D-CT but overestimated by 4D-MRI. They discussed that this could be due to limited temporal resolution of 4D-MRI acquisition (1.4 s/volume). The temporal resolution could also be the reason why in this study 4D-MRI produced the tumor volume similar to that of 4D-CT. In this study, we used a 3T MRI scanner instead of 1.5T. Higher magnetic field is able to enable a faster scanning time. The temporal resolution of TWIST sequence used in our study is 0.9 s/volume, which is nearly 36% faster. It is believed that the lower the temporal resolution, the more blur a moving object appears on the image. The positions of the moving object at different times are integrated and averaged during the period of acquisition time. As a result, with higher temporal

resolution, the tumor volumes derived using 4D-MRI in this study are similar to the ground truth obtained using 4D-CT.

Visual comparison of tumor motion path in the CC direction (Figure 3-14) shows that the sorted 4D-MRI is able to exhibit a complete tumor displacement path as 4D-CT. Quantitative evaluation of accumulated tumor volume (Table 3-12) and tumor motion coverage in the CC direction (Table 3-13) further proves that there is no significant difference between the two modalities in terms of investigating tumor motion. Despite a lower temporal resolution compared with 4D-CT, the advantage of 4D-MRI over 4D-CT is its capability of repeated acquisitions over multiple breathing cycles. As a result, more positions can be covered to form an average breathing cycle. By averaging from multiple breathing cycles, 4D-MRI exhibits comparable ability as 4D-CT to describe the tumor motion over one breathing cycle.

Due to the difficulty of recruiting lung cancer patients, a limitation of the study could be the insufficient number of lung cancer patient dataset. However, the results generated in this study are very consistent for the six patients. It is expected that results would not differ much for other lung cancer patients.

3.3.4 Study conclusion

This study proposed to sort 4D-MRI volumes into corresponding breathing phases in 4D-CT system by comparing the lung height between volumes of 4D-MRI and 4D-CT. In terms of lung tumor imaging, 4D-MRI exhibited comparable ability to capture the tumor volume and to describe the tumor

motion as 4D-CT. Thus 4D-MRI has potential to be used in 4D-RT as a radiation-free alternative to 4D-CT.

3.4 Chapter discussion and summary

Three 4D-MRI sequences (FLASH 3D, VIBE, and TWIST) have been compared in terms of image quality and their ability to capture lung and tumor motion. FLASH 3D exhibited the best image quality among the three sequences. FLASH 3D was capable of covering the extreme positions of tumor motion path but failed to capture the motion range of lungs due to low temporal resolution. With a temporal resolution of 0.9 volume/s, TWIST is sufficient to study the motion of tumor and diaphragm under controlled breathing. Volumes acquired by TWIST were then used to compare with 4D-CT volumes to see whether 4D-MRI is comparable to 4D-CT in terms of presenting tumor volume and describing tumor motion. Tumor volume and tumor motion analysis showed that there is no significant difference between 4D-MRI and 4D-CT.

All the 4D-MRI datasets were acquired using a Siemens scanner in this study. Although not tested, the author believes the experiments and results can be repeated using 3T scanner of other manufactures such as GE and Philips. This is because the sequences used in this study all have equivalent ones on GE and Philips scanners. Table 3-14 summarizes the equivalent sequences on Siemens, Philips, and GE scanners.

Table 3-14 Equivalent sequences used by different manufactures

Manufacture	Siemens	Philips	GE
Sequence	FLASH	FFE	SPGE
(Abbrev.)	TWIST	TRAK	TRICKS
	VIBE	THRIVE	LAVA

FFE: Fast Field Echo; **SPGE**: SPoiled Gradient Recalled acquisition in the steady state; **TRAK**: Time-Resolved Angiography using Keyhole; **TRICKS**: Time-Resolved Imaging of Contrast Kinetics); **THRIVE**: T1 High Resolution Isotropic Volume Excitation; **LAVA**: Liver Acquisition with Volume Acceleration.

A limitation of the studies in Chapter 3 is that the statistical power of the lung cancer patient dataset might be insufficient due to the difficulty in volunteer recruitment. The studies are not regarding the race, age, sex and type of lung cancers represented by the patients. Nevertheless, coherent results were shown for the six patients in this study. It is expected that similar results can be observed on other patients regardless of the race, age, sex and type of lung cancers. More studies however need to be carried on. The focus of the studies in Chapter 3 is to evaluate the performance of 4D-MRI sequences in thoracic imaging and to gain insights to the 4D-MRI sequences thus allowing further development of the sequences.

Chapter 4 Automated segmentation of multi-structures on 4D-MRI thoracic dataset

4.1 Chapter overview

In the second step of 4D-RT (i.e. target delineation), tumor and other target structures need to be segmented for every 3D volume within the 4D dataset. However, manual segmentation of a 4D dataset that typically contains many 3D volumes is extremely tedious and time-consuming. Manual segmentation could also result in large intra- and inter-user variability. This requires the development of new automated segmentation techniques or schemes for 4D-MRI thoracic data segmentation.

This chapter presents the development of a novel automated segmentation scheme based on deformable registration for 4D-MRI thoracic dataset. Three studies were performed in this chapter. The first study is to apply the basic registration-based segmentation scheme to a 4D-MRI thoracic dataset to study whether registration-based segmentation approach is suitable. Accurate results showed that the registration-based approach is suitable for the segmentation of 4D-MRI thoracic dataset. However, directly applying registration-based

segmentation techniques to segment the whole 4D-MRI dataset will be inefficient. One reason for this inefficiency is that the tolerance number to terminate registration is usually set as a fixed value that can potentially lead the registration to exceed the point beyond what is required. This will result in unnecessary computational amount. In the second study, we investigated the relationship between the optimal tolerance number and image similarity and proposed a manner that is based on spatio-temporal information to adaptive adjust registration tolerance. In the third study, using the results obtained in earlier study, an automated 4D registration-based segmentation scheme that is based on spatio-temporal information for the segmentation of thoracic 4D-MRI thoracic dataset is proposed. The proposed scheme saved up to 95% of computation amount while achieving comparable accurate segmentations compared to directly applying registration-based segmentation to 4D dataset. The scheme facilitates rapid 3D/4D visualization of the lung and tumor motion and, potentially, the tracking of tumor during radiation delivery.

4.2 Registration-based segmentation of 4D-MRI thoracic dataset¹

As discussed in Section 2.3.2, registration-based segmentation has been popular for the segmentation of 4D images compared to other segmentation techniques. However, although registration-based segmentation has been employed in a number of applications of segmenting 4D dataset, including 4D-CT of lungs, heart, liver, and kidney, and 4D-MRI cardiac dataset, this technique has not been reported to be an accurate method to segment 4D-MRI thoracic images. Thus, in this study, the registration-based segmentation technique is adopted for the purpose of target delineation of 4D-MRI thoracic dataset. This study aims at segmenting multiple structures (lungs) of a 4D-MRI thoracic dataset using the basic registration-based segmentation scheme to evaluate the accuracy of this method.

4.2.1 Materials and method

4.2.1.1 Registration-based segmentation

The overall schema of the registration-based segmentation method is illustrated in Figure 4-1. First, a reference volume (v_{ref}) is manually segmented

¹ The work in this section is derived from Y. Yang, C.H. Tan, and C.L. Poh. ‘Visualization of lung using 4D magnetic resonance imaging.’ *Proceedings of the 1st International Symposium on Bioengineering (ISOB 2011)*. pp. 49-55. 2011. Permission of reprint is granted in the copyright agreement.

² The work in this section is derived from: Y. Yang, E. Van Reeth, and C.L. Poh.

to extract the lung structure and tumor that will serve as the template (m). Three dimensional B-spline non-rigid registration [163] is then applied between target volumes (v_t , $t = 1, 2, 3, \dots, n$) and the reference volume (v_{ref}). B-spline registration deforms an image by manipulating an underlying mesh of control points based on B-splines. In this study, a uniform grid of control points was automatically constructed with 8 control points along each dimension. By calculating displacements of control points, local elastic deformations can be found. These control points act as parameters of a free-form deformation model based on B-splines. Optimization is performed in a sequence of Quasi-Newton iterations with respect to a similarity measure that quantifies the quality of the match between the deformed reference scan and the target scans. Mutual information is used in this work as the similarity measure. Three-dimensional displacement fields from the reference volume to the target volumes ($\mathbf{r}_{(v_{ref} \rightarrow v_t)}$) can be acquired by modeling with every point within the 3D volume using the 3D displacement of each point. The resulting displacement fields are vector fields in which each vector is represented by an arrow pointing from the point in the reference volume to the same point after its movement in the registered reference volume. The corresponding transformations are used to deform the template (m) into deformed segmentation masks (m_t). This registration-based segmentation scheme was performed using insight toolkit (ITK) [164].

Manual segmentation was performed by an expert in lung structure and then independently verified by an experienced radiologist to ensure the segmentation is correct.

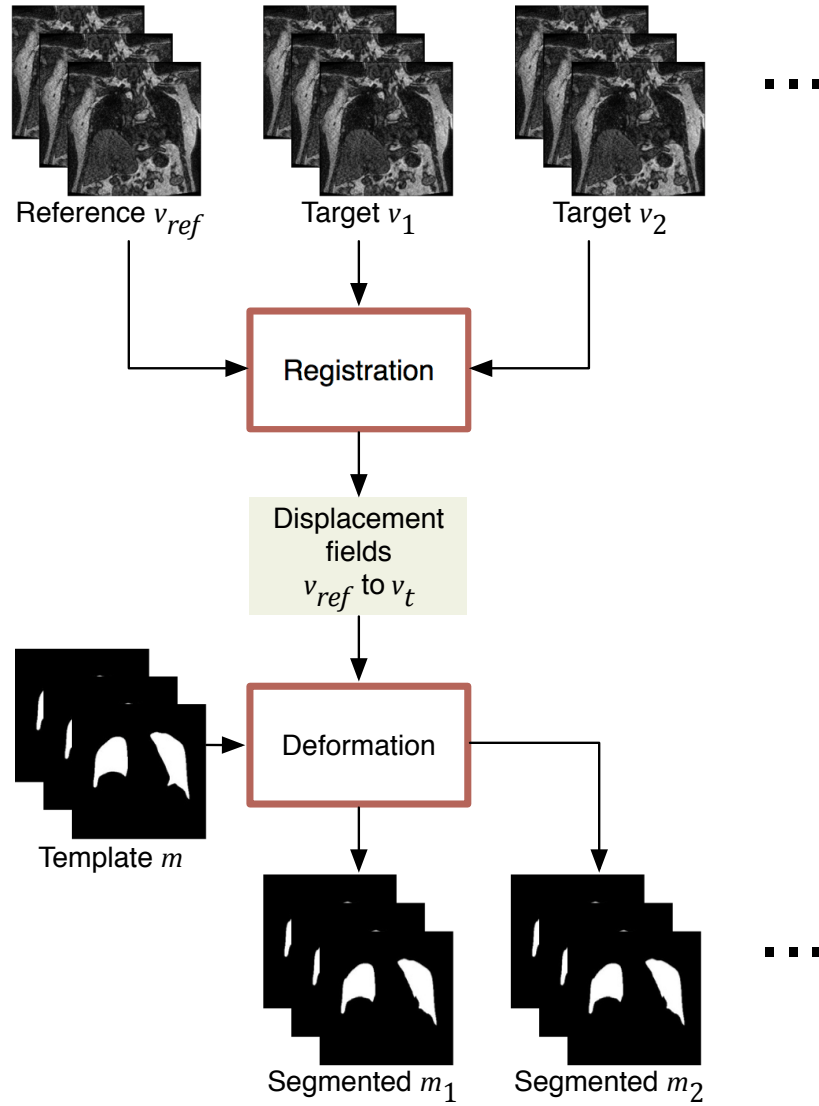


Figure 4-1 Schematic of the registration based segmentation method. Inputs to the scheme are: the reference volume (v_{ref}), the target volumes (v_t), and the template (m). Intermediate results are the transformation warping ($r_{(v_{ref} \rightarrow v_t)}$). The output of the scheme is the deformed binary segmentations of the target scans (m_t).

4.2.1.2 Validation of the segmentation method

Each target volume was manually segmented and verified by an experience radiologist who is blinded from the automated segmentation results. These

manual segmented volumes serve as the ground truth for the validation of the automated segmentation. Automatically segmented volumes can be quantitatively evaluated by comparing to the ground truth. Three metrics sensitivity, specificity and Dice's coefficient (DSC) were used to quantify how well two surfaces match each other.

Sensitivity shows the proportion of true positives that are correctly identified.

$$\text{Sen.} = \frac{\text{TruePositive}}{\text{TruePositive} + \text{FalseNegative}} \quad (4.1)$$

Specificity represents the proportion of negatives that are correctly identified.

$$\text{Spec.} = \frac{\text{TrueNegative}}{\text{TrueNegative} + \text{FalsePositive}} \quad (4.2)$$

Dice's coefficient [165] indicates how well two shapes, A and B match:

$$\text{DSC} = \frac{2|A \cap B|}{|A| + |B|} \quad (4.3)$$

If two segmentations are identical, then all three values will be equal to 1. The three values will be 0 if they have no common region.

4.2.1.3 Multi-dimensional visualization

An important step in analyzing the anatomy and motion of organs is to construct 3D models. It is possible to construct the 3D surface models using the segmented images of target structures. In this study, 3D models are constructed

using the marching cubes algorithm [166] using visualization toolkit (VTK) [167] and visualized using Paraview [168] subsequently.

4.2.1.4 Data

As presented in Chapter 3, TWIST sequence has good image quality while being able to show the motion path of diaphragm and tumor. As a result, TWIST is selected in this study. A total of seven 3D volumes from a 4D-MRI dataset of the thorax of one healthy subject were used. To show the capability of the segmentation technique, all seven volumes are either at the maximum inhalation phase or at the maximum exhalation phase since this will require the largest deformation by the registration method. All the scans were acquired on a Siemens Magnetom Trio 3T MR system using a 12-channel phased array coil. An in-plane resolution of 320×320 pixels and $1.09 \times 1.09 \text{ mm}^2$ was achieved. For each scan, 60 slices were acquired with an out of plane resolution of 1.5 mm. The resulting acquisition time was 5 seconds per volume. As a preliminary study, only odd slices were used for each scan. Hence, the resulting out of plane resolution is 3 mm. Time between two scans in this work is approximately 15 seconds.

4.2.2 Study results

The proposed registration-based segmentation method was successfully applied to all seven 3D thoracic MR volumes with approximately 15 seconds between each set. Figure 4-2 shows examples of segmented images. Figure

4-2(a) illustrates a typical coronal 2D slice of the reference scan and target volume 1 and 2. Figure 4-2(b) shows the registered reference volume to the corresponding target volumes. Figure 4-2(c) shows the resulting segmentations for the reference volume and target volume 1 and 2 and Figure 4-2(d) shows the final contour obtained overlaid with the corresponding MR image. The segmentations for target volumes were generated by the registration-based approach while the reference volume was manually segmented. Table 4-1 summarizes the matching indices between the manual and automated segmentations of all six target volumes. The results show that the automated segmentation results matched well with the ground truth. Acceptable sensitivity and DSC (an average of 0.844 ± 0.014 and 0.851 ± 0.005 respectively) were achieved, whereas a high specificity was obtained, an average of 0.980 ± 0.003 .

Using the segmented volumes, it is possible to generate the 3D models of each target volume and calculate the approximate lung volume at each time point. Figure 4-3 shows examples of visualizing the 3D models of the reference volume, target volume 1, 2, and 3. Compare with the reference volume, lungs of target volume 1 and 3 were expanded while those of target volume 2 were contracted. Using the assumption that the approximate lung volume equals the multiplication of the total number of identified pixel within the 3D lung structure by the size of a pixel, seven sets of lung volumes were calculated. Figure 4-3 summarizes the approximate lung volume for the reference volume and target volume 1, 2, and 3. One can see that target volume 3 has the largest volume while target volume 2 has the smallest volume among all seven volumes.

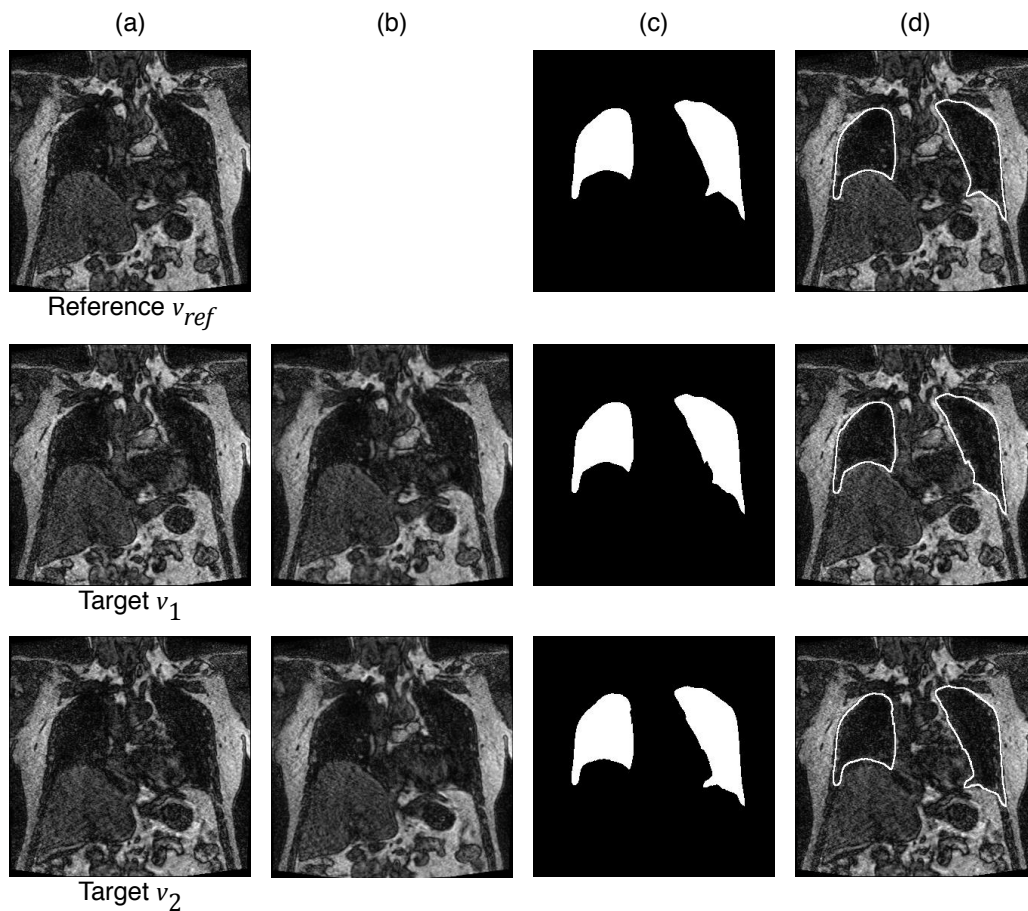


Figure 4-2 Coronal slices of (a) original volumes: reference volume and target volume 1 and 2; (b) registered reference volume corresponding to target volume 1 and 2; (c) Manual segmentation of reference volume and automated segmentations of target volume 1 and 2; (d) volumes with segmented contours.

Table 4-1 Evaluation Results of Automated Segmentation

Target scan	Sen.	Spec.	DSC
1	0.855	0.977	0.851
2	0.864	0.980	0.860
3	0.828	0.984	0.854
4	0.839	0.981	0.849
5	0.828	0.981	0.846
6	0.846	0.979	0.845
Average	0.844	0.980	0.851
Stdev	0.014	0.003	0.005

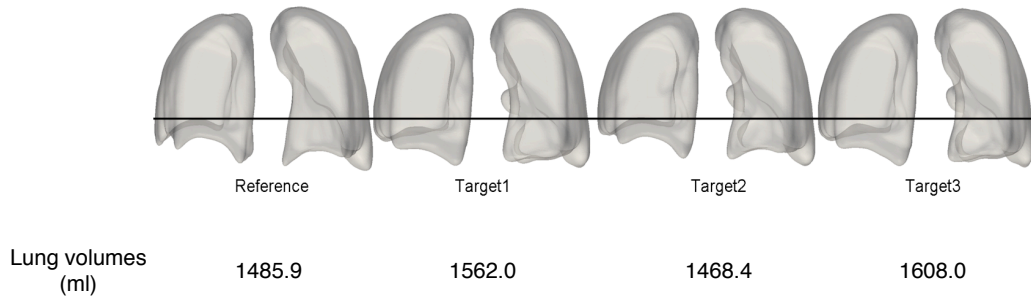


Figure 4-3 Three-dimensional model and volume calculated for reference volume, target volume 1, target volume 2, and target volume 3.

4.2.3 Study discussion

Images segmented by registration-based segmentation method achieved acceptable sensitivity, specificity, and DSC. Standard deviations of all three metrics are very low, indicating that the automated segmentation method works generally well for all the data sets. From Figure 4-2, it can be clearly seen that the automatically generated contours well delineated the boundary of lungs on target volumes. These results prove that the registration-based segmentation technique is suitable for accurate segmentation of 4D-MRI thoracic data.

For target volume 1 and 3 shown in Figure 4-3 as examples, comparing with the reference scan, the lungs were expanded. For target volume 2, the lungs were contracted as compared to the reference volume. This correlates well with the lung volume values. In the deformation fields from v_{ref} to the v_1 and v_3 , the arrows in the lung area are pointing down as expected. Most of the vectors with large magnitude are at the dome of the diaphragm, which shows that the diaphragm motion is most prominent during breathing. For the deformation field from v_{ref} to v_2 , the arrows point upward because the lungs were contracted. It is also noticed that the magnitude of the deformation fields from

v_{ref} to v_2 is smaller than those from v_{ref} to v_1 and v_3 . This is because the volume difference between v_{ref} and v_2 is much smaller than those between v_{ref} and v_1 and v_3 , as presented in Figure 4-3. Small difference in diaphragm position is also shown in Figure 4-3.

4.2.4 Study conclusion

This section presented a study that investigates an automatic segmentation method performed on 4D thoracic MRI dataset. The proposed algorithm is based on a registration-based segmentation technique to segment 3D lung structures and to reconstruct 3D models. Deformation fields from the reference scan to target scans, formed by using the 3D displacements of each point in the images, can provide a basis for motion analysis.

4.3 Adapting registration-based segmentation for efficient segmentation of thoracic 4D-MRI²

In the earlier Section 4.2, it is shown that the registration-based segmentation method is able to accurately segment the 4D-MRI thoracic dataset. Generally, registration algorithms are considered to have converged when the difference between successive deformation fields are smaller than a pre-determined threshold referred as tolerance. The tolerance should be set such that enough iterations are performed for accurate registration while registration is terminated before the point beyond which computational effort is wasted [169]. During registration-based-segmentation progress, though different images are registered to the reference image, the tolerance is usually set as a fixed value. However, it is known that the larger the difference between two image volumes, the more iteration is required for registration to converge. Since the tolerance number is inversely proportional to the iteration number, the iteration number could potentially drop if the tolerance number is set differently with respect to different pairs of registered volumes throughout the whole registration-based segmentation progress.

The hypothesis is that the tolerance number should be related to the similarity of two registered images. The more similar the two images are, the

² The work in this section is derived from: Y. Yang, E. Van Reeth, and C.L. Poh. ‘Adapting registration-based-segmentation for efficient segmentation of thoracic 4D MRI.’ *Computational Intelligence in Healthcare and e-health (CICARE)*, 2013 *IEEE Symposium on*. pp. 42-45. IEEE, 2013. Permission of reprint is granted in the copyright agreement.

smaller the tolerance is needed for registration to achieve accurate results. In this study, this hypothesis is proved using two widely used deformable registration methods: the demons algorithm [139] and B-spline registration [163]. A new method that is based on spatio-temporal information to indicate the similarity of dynamic thoracic images is also introduced. Its usage is displayed for the task of segmenting the lung and lung tumor at different respiratory phases using thoracic 4D-MRI dataset that comprises a number of 3D-MRI volumes acquired over time.

4.3.1 Materials and methodology

4.3.1.1 Common similarity measures

Similarity measure is used to quantize how similar the two volumes are. Please refer to Equation (2.3) (2.4) and (2.5) for the common similarity measures used in this study.

4.3.1.2 Relative diaphragm displacement

The diaphragmatic movement is the principal movement in the chest and all the lung-related structures do move almost synchronously [160]. Since our task is to segment the lung and lung tumor of 4D-MRI dataset, the diaphragm displacement could be a good indicator to evaluate the similarity of two volumes. A two-dimensional spatio-temporal (2DST) image shows the prominent motion pattern of the diaphragm in cranio-caudal direction [160]. The generation of 2DST image in this study is illustrated in Figure 4-4.

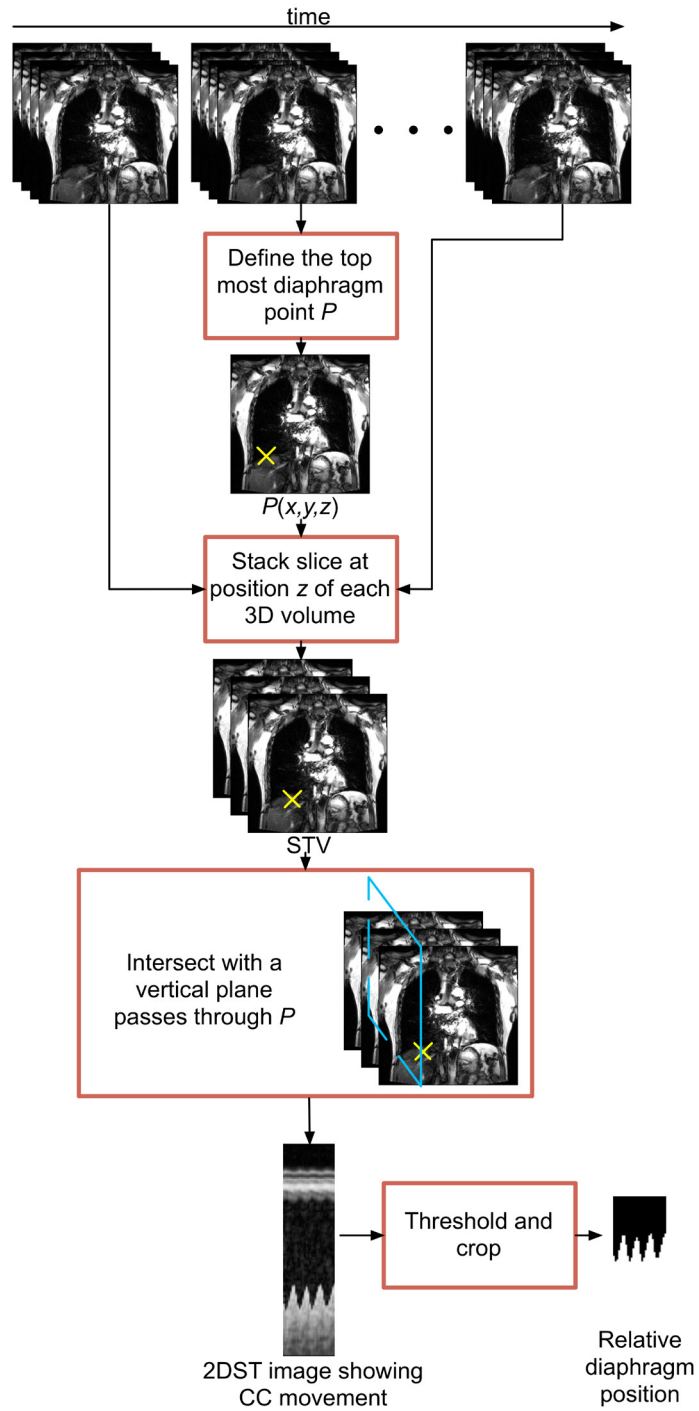


Figure 4-4 Generation of 2DST image

The top diaphragm point ($P(x, y, z)$) of a 3D volume within the 4D dataset is first defined by the user. A spatio-temporal volume (STV) is then constructed by stacking coronal slices at the same position z of each 3D volume within the

4D dataset. A sagittal plane that passes through this point $P(x,y,z)$ orthogonally intersects STV and defines a 2DST image (Figure 4-4). After applying a simple hard threshold, the relative diaphragm position is obtained from the binary 2DST image.

4.3.1.3 Deformable registration stopping tolerance

Demons registration

Demons registration iteratively deforms the reference volume by applying a displacement vector $d\mathbf{r}$ in a voxel-by-voxel manner, according to (4.7),

$$d\mathbf{r}^{(n+1)} = \frac{(v_{ref}^{(n)} - v_t)\nabla v_t}{(v_{ref}^{(n)} - v_t)^2 + |\nabla v_t|^2} \quad (4.7)$$

where v_{ref} is the reference volume, v_t is the target volume, and n is the iteration number. The gradient operator ∇ is calculated spatially in 3D. A Gaussian filter is applied to smooth the displacement field, suppress noise and preserve the geometric continuity of the deformed image. The overall deformation field \mathbf{r} is updated iteratively by:

$$\mathbf{r}^{(n+1)} = \mathbf{r}^{(n)} + d\mathbf{r}^{(n+1)} \quad (4.8)$$

Gu et al. [170] defined a term called relative norm:

$$l^{(n)} = \frac{\sum |d\mathbf{r}^{(n+1)}|}{\sum |\mathbf{r}^{(n)}|} \quad (4.9)$$

Summations are defined over whole volumes.

In this study, the stopping criterion for demons registration was defined as:

$$l^{(n-1)} - l^{(n)} \leq e \quad (4.10)$$

where e is the tolerance for registration to stop.

B-spline registration

B-spline registration deforms an image by manipulating an underlying mesh of control points based on B-splines. It tries to minimize a cost function C associated with B-spline control point transformation parameter ϕ :

$$C(\phi) = D[v_t, \phi(v_{ref})] + \alpha R(\phi) \quad (4.11)$$

where D is the image dissimilarity, R is the regularizing term associated with smoothness of the deformation, and α is a regularizing parameter. In this study, sum of square difference (SSD) was used for image dissimilarity and thin sheet of metal bending energy [171] was used for smoothing. The stopping criterion was defined as:

$$\left\| \frac{dC(\phi)}{d\phi} \right\| \leq e \quad (4.12)$$

4.3.1.4 Deformable registration stopping tolerance versus similarity measures

It is hypothesized that a smaller tolerance is needed for registration between two more similar volumes with same level of registration accuracy. In order to prove this, pairs of volumes at different positions of breathing cycle were registered. For each pair, automated segmentation of target volume was obtained after each iteration during registration. Dice's similarity coefficient (DSC) that indicates the level of match for two segmentations were calculated between automated segmentations and the ground truth segmentation of the target volume. Ground truth was generated by manual segmentation of the MRI data and validated by an independent experienced radiologist who was blinded from the registration based segmentation results. It is expected that as the iteration goes on, the registration will deform the reference image closer to the target image so that the DSC value will increase while the tolerance number ϵ will decrease. A sample plot of DSC and tolerance number against the iterations is shown in Figure 4-5. When the DSC value hit the 'plateau', tolerance number at that iteration was noted down. Samples of segmented images are shown in Figure 4-6.

4.3.1.5 Data

4D-MRI scans with TWIST sequence of two patients were used in this study. The specificities of the acquired images are the same as in Section 3.2. A total of 11 volumes from 2 patients were used to run this test to study the

relationship between the optimal tolerance number and the similarities measures i.e. SSD, XCOR, MI, and the relative diaphragm displacement.

4.3.2 Study results and discussion

Plots of optimal tolerance number against SSG, XCOR, MI and relative diaphragm displacements are shown in Figure 4-7 and Figure 4-8 for demons and B-spline registration respectively. It is found that generally the optimal value of tolerance decreases when relative similarity between two volumes increases. Fitted power equation was used to quantify the relationship between the optimal tolerance number and similarity measures. Image similarity based on relative diaphragm displacement achieved the highest R^2 values, with 0.957 for demons registration and 0.772 for B-spline registration.

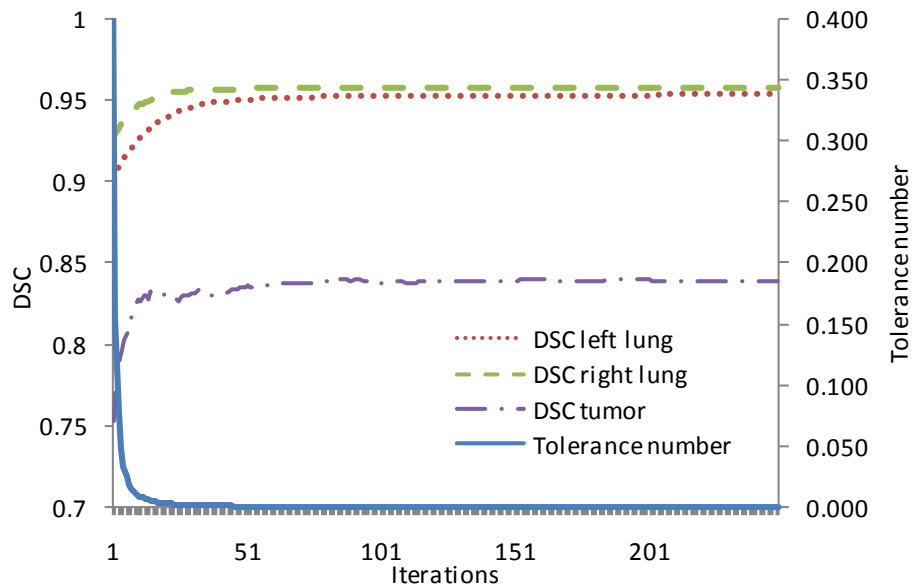


Figure 4-5 Sample plot of DSC and tolerance number against the iterations

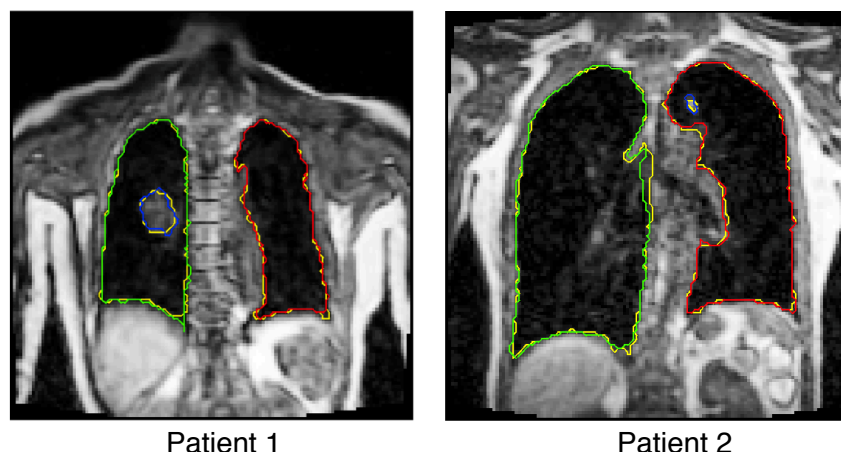


Figure 4-6 Samples of automatically segmented images of Patient 1 and Patient 2. Contours in red: left lung; Contours in green: right lung; Contours in blue: tumor; Contours in yellow: ground truth.

Geometry based similarity measures, such as DSC, are commonly used to quantify the accuracy of segmentation. In our study, the optimal tolerance numbers chosen for registration to stop were also based on the segmentation accuracy. Thus, it is reasonable that the optimal tolerance number is closely related to the geometry based relative diaphragm displacement as observed in our study, rather than those similarity measures that are image intensity based. Other geometry based similarity measures, such as anatomical landmarks, curves and surfaces [127] could potentially also relate well with the optimal tolerance. But the simple generated relative diaphragm displacement without user intervention would be a better choice.

4.3.3 Study conclusion

This study showed that, the more similar the two images are, the smaller the tolerance is needed for registration to achieve accurate results. The results suggest that relative diaphragm displacements can a good choice as a guide to

adaptively adjust the tolerance parameter used in registration-based-segmentation scheme to reduce the computational complexity for the segmentation of 4D thoracic MRI images. This is exploited and studied in the development of a spatio-temporal based scheme for efficient registration-based segmentation of thoracic 4D-MRI that will be presented in the next Section 4.4.

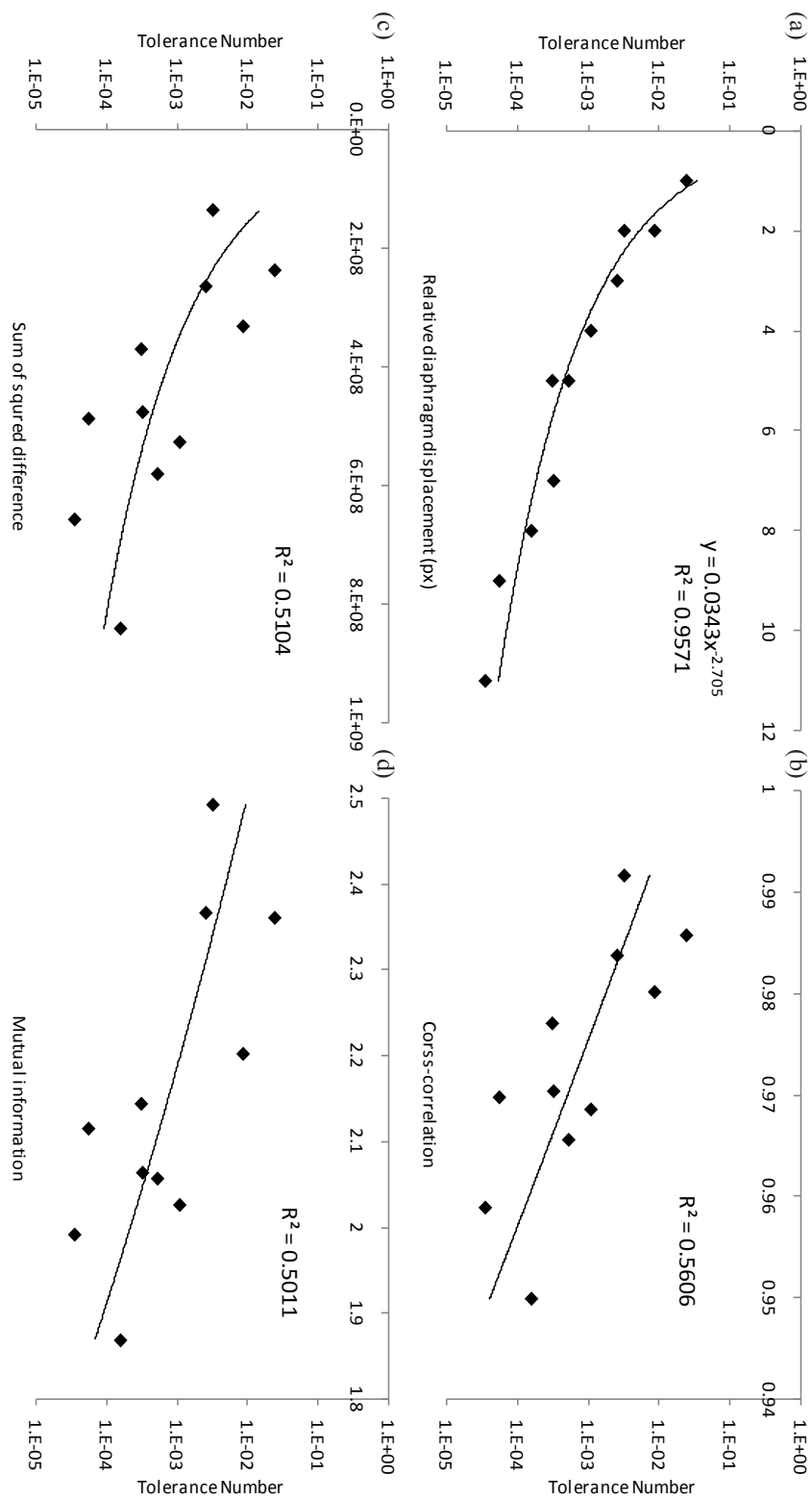


Figure 4-7 Plots of optimal tolerance number against (a) relative diaphragm displacement; (b) cross-correlation; (c) sum of squared difference; and (d) mutual information for demons registration

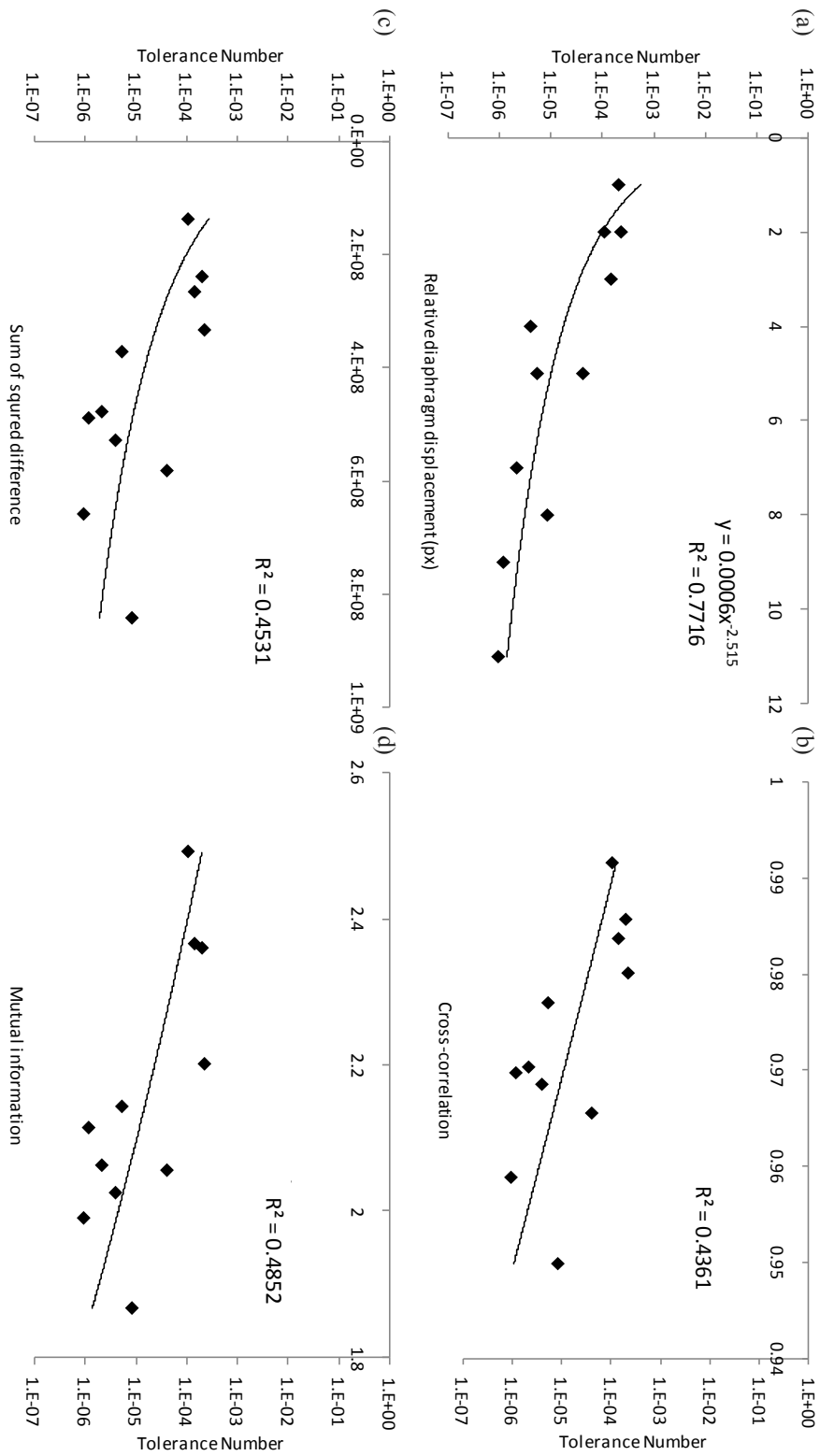


Figure 4-8 Plots of optimal tolerance number against (a) relative diaphragm displacement; (b) cross-correlation; (c) sum of squared difference; and (d) mutual information for B-spline registration

4.4 A Spatio-temporal based scheme for efficient registration-based segmentation of thoracic 4D-MRI³

As discussed in Chapter 2 and Section 4.2 Chapter 4, the general scheme of applying registration-based segmentation method to segment 4D images is to register a reference volume (v_{ref}) to the other target volumes using 3D deformable registration to obtain the respective deformation fields (Figure 4-9(a)) [105]. The reference volume will be segmented separately and this segmented reference volume will then serve as the template for propagation. The reference volume is usually segmented in a semi-automatic manner. To obtain the final segmented target volumes, the corresponding deformation fields are used to deform the template volume to match the target volumes. Figure 4-10 illustrates the flowchart of this basic registration-based segmentation scheme. However, the direct application of registration-based segmentation to 4D images over several breathing cycles is inefficient. It is shown in Section 4.3 Chapter 4 that the larger the difference between the two volumes, the more numbers of iteration are required for registration to converge. If the reference volume is chosen blindly and registered to the other volumes within the 4D

³ The work in this section is derived from: Y. Yang, E. Van Reeth, C.L. Poh, C.H. Tan, and I. W.K. Tham. 'A spatio-temporal based scheme for efficient registration-based segmentation of thoracic 4D MRI' *Biomedical and Health Informatics, IEEE Journal of* (Accepted). Permission of reprint granted in the copyright agreement.

dataset, the potential difference between volumes to register can be large (e.g. for volumes at full-exhale and full-inhale phases). This would lead to large computational time. One way to reduce computational time is to sequentially register adjacent volumes as illustrated in Figure 4-9(b). Adjacent volumes are believed to be similar. Thus, the number of iterations for registrations to converge is smaller. However, the propagated and accumulated registration error may be very large for volumes at later time frame [172]. Consequently, the registration scheme shown in Figure 4-9(a) is more commonly used.

In this section, a novel spatio-temporal based scheme for 4D registration-based segmentation of thoracic 4D MR images is proposed and developed. The aim is to improve the efficiency of the basic registration-based segmentation scheme. The proposed scheme takes advantage of the periodicity of the acquired volumes along the breathing cycles. Spatio-temporal information about diaphragm movement is derived directly from the 4D MR images to optimally choose the reference volume and to categorize the other volumes into sub-groups based on diaphragm positions. The tolerance parameter of registration is subsequently adjusted based on the spatio-temporal information to speed up the registration convergence by reducing the number of iterations required. The proposed scheme is fully automatic after the initial segmentation of reference volume to generate the template volume.

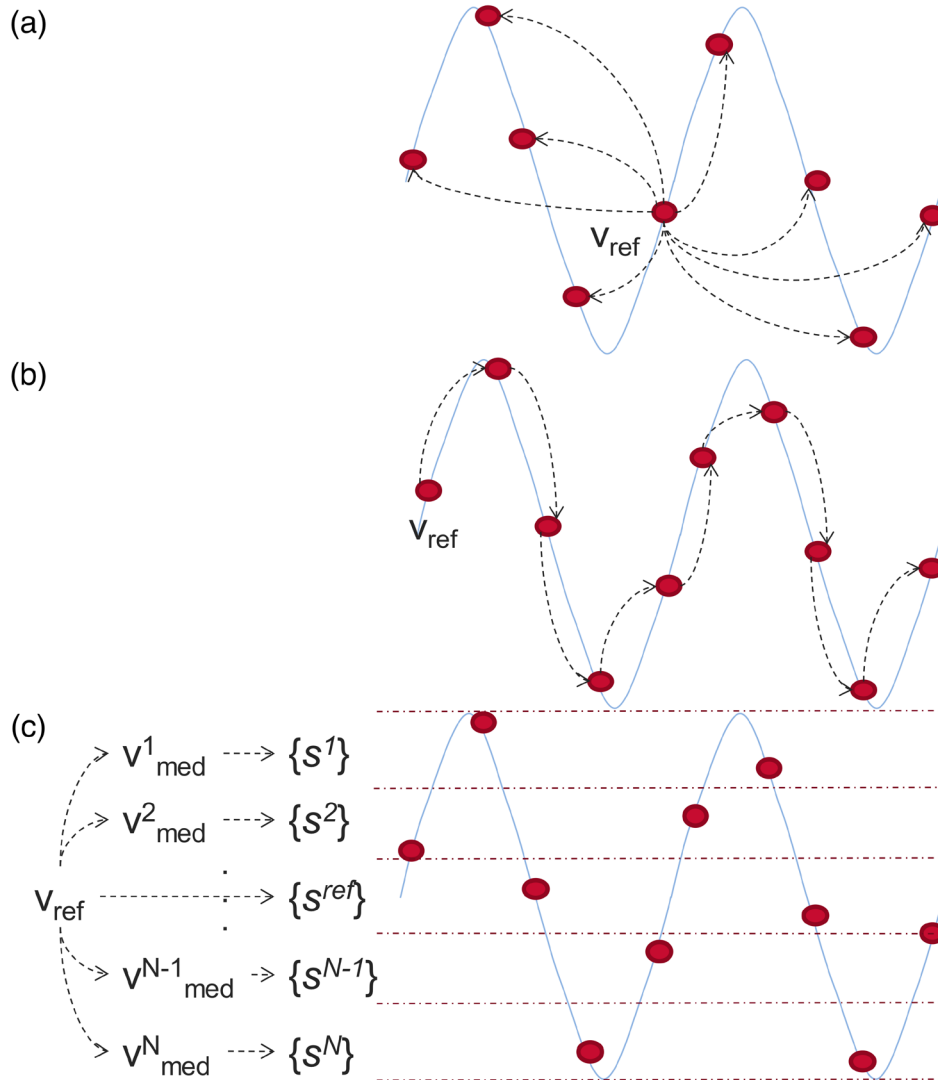


Figure 4-9 Different registration strategies: (a) Registrations are performed from the reference volume (v_{ref}) to every other target volume; (b) Registrations are performed sequentially between adjacent volumes; (c) Similar volumes are grouped into N sets s^i . The reference volume (v_{ref}) is registered to each representative v_{med}^i of volume set s^i and to each volume within the reference set s^{ref} . Each representative v_{med}^i is registered to each volume with the corresponding volume set s^i .

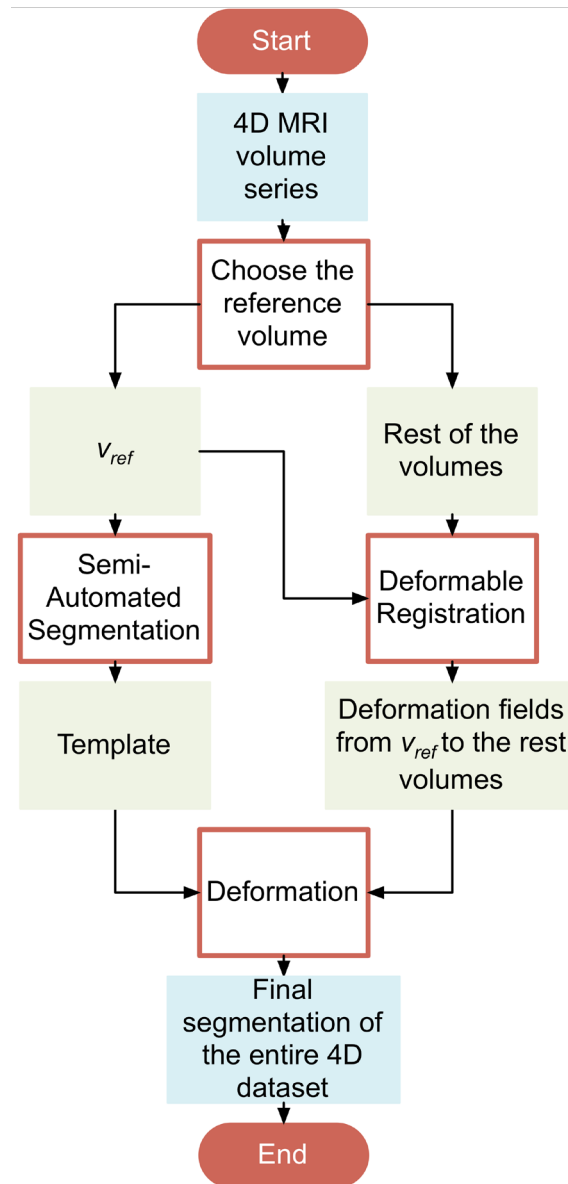


Figure 4-10 Basic registration-based-segmentation scheme

4.4.1 Materials and methodology

4.4.1.1 Proposed scheme

Limiting the number of iterations required during the registration step is central to the proposed approach. The proposed scheme aims at performing registration between volumes that are acquired at similar phases of the breathing cycle. Thus, the first step of the proposed scheme consists of sorting the acquired volumes along the breathing cycle through the generation of 2D spatio-temporal (2DST) images, and grouping the volumes that have similar diaphragm positions into N sets. Within each set, fast registrations are performed. A representative volume is chosen based on relative diaphragm position in each set and each representative volume is subsequently registered with the reference volume from which the initial segmentation was obtained. The overall schematic is illustrated in Figure 4-11. The following sub-sections detail each step of the proposed registration-based segmentation scheme.

Generate two-dimensional Spatio-Temporal (2DST) image

The 2DST image shows the prominent motion pattern of the diaphragm in cranio-caudal direction. Generation of 2DST image in this study is the same as Section 4.3 Chapter 4 (Figure 4-4). A function d is defined to represent the relative diaphragm position. The maximum exhalation position is set as 0 and the maximum inhalation position is set as d_{max} .

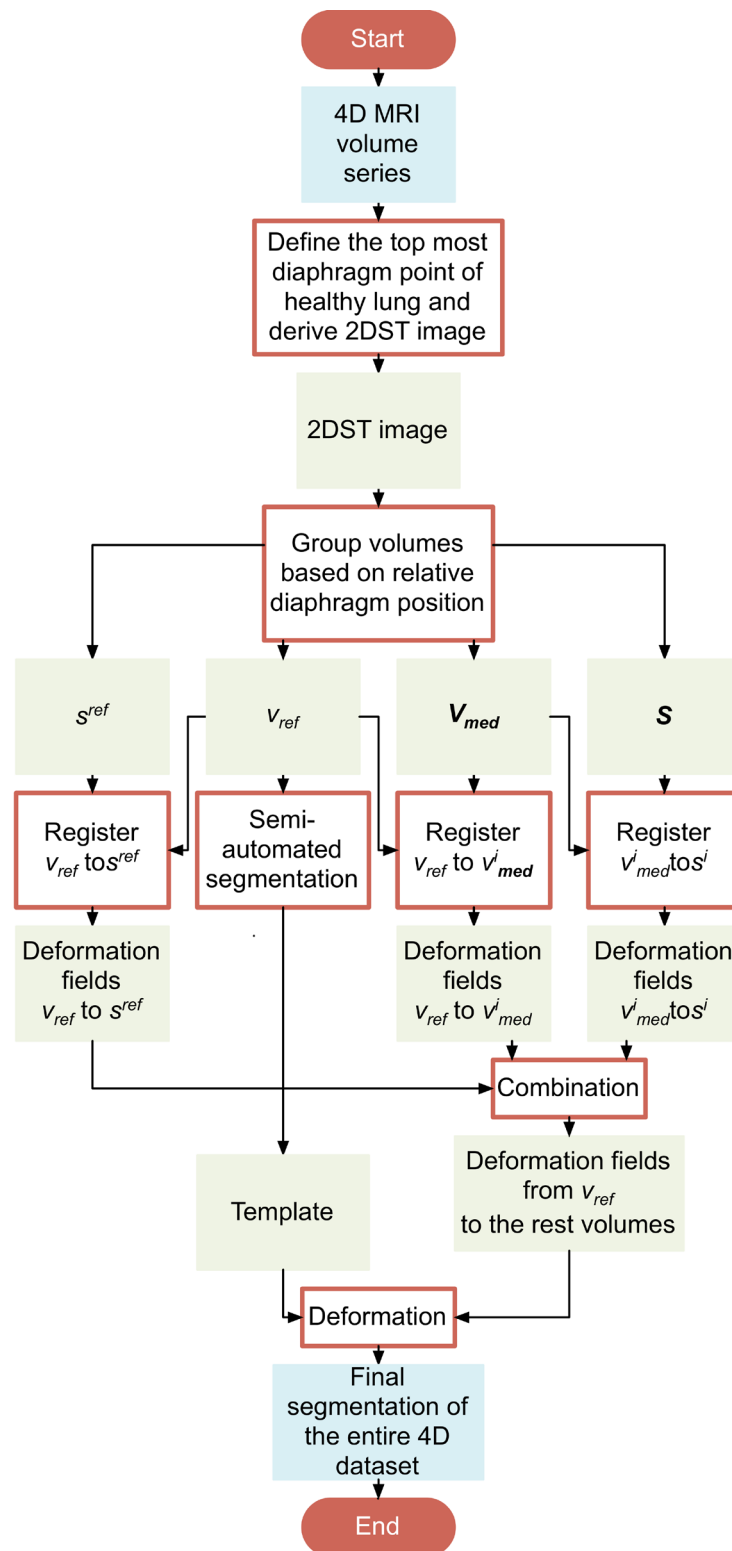


Figure 4-11 Overall illustration of proposed scheme

Group volumes based on relative diaphragm position

All volumes are grouped based on relative diaphragm position derived from the previous step. The idea is to group similar volumes into one set (Figure 4-9) so that most of the registrations are performed between similar volumes within each set (s^i). The reference volume (v_{ref}) is selected as the median position of all the volumes within a 4D data series:

$$v = v_{ref} \quad \text{if} \quad d(v) = \text{median}(d) \quad (4.13)$$

The chosen reference volume is then segmented and the segmented reference volume will serve as the template. In this study, we used an interactive active contour based segmentation method [98] available in 'ITK-SNAP' [173], an open-source program developed by Yushkevich et al. for semi-automatic segmentation of 3D images, to delineate both lungs and tumor.

Volumes whose relative diaphragm displacements from v_{ref} are not greater than x pixels are grouped together to form the reference set (s^{ref}).

$$\begin{aligned} v \in s^{ref} \quad & \text{if} \quad d(v_{ref}) - x \leq d(v) \leq d(v_{ref}) + x \\ \text{AND} \quad & v \neq v_{ref} \end{aligned} \quad (4.14)$$

All other volumes are grouped into N sets of volumes (s^i , $i = 1, 2, 3, \dots, N$) so that within each set, the relative diaphragm displacement between any two volumes do not differ more than $2x + 1$ pixels.

$$\begin{aligned}
v \in s^i & \quad \text{if } (i-1)(2x+1) \leq d(v) \leq i(2x+1)-1 \\
\text{AND} & \quad v \notin s^{ref} \\
(i = 1, 2, 3, \dots, N) & \quad N = \text{ceiling}\left(\frac{d_{max} + 1}{2x + 1}\right)
\end{aligned} \tag{4.15}$$

A median volume (v_{med}^i) was then selected to be the representative volume of each set (s^i).

$$v = v_{med}^i \quad \text{if } d(v) = \text{median}[d(s^i)] \tag{4.16}$$

This grouping step is illustrated in Figure 4-12. We set $x = 1$ in this study.

Perform a series of deformable registrations and segment target volumes

After grouping volumes based on relative diaphragm position, registrations are performed. In order to make the process efficient, registrations should be performed between similar volumes. Thus the reference volume will be registered to each volume within the reference set, and each representative volume will then be registered to each volume within its corresponding volume set. The only relatively large computational cost will be in the registration of reference volume to each representative volume. For this purpose, a number of registrations are performed as follows (Figure 4-9 and Figure 4-11):

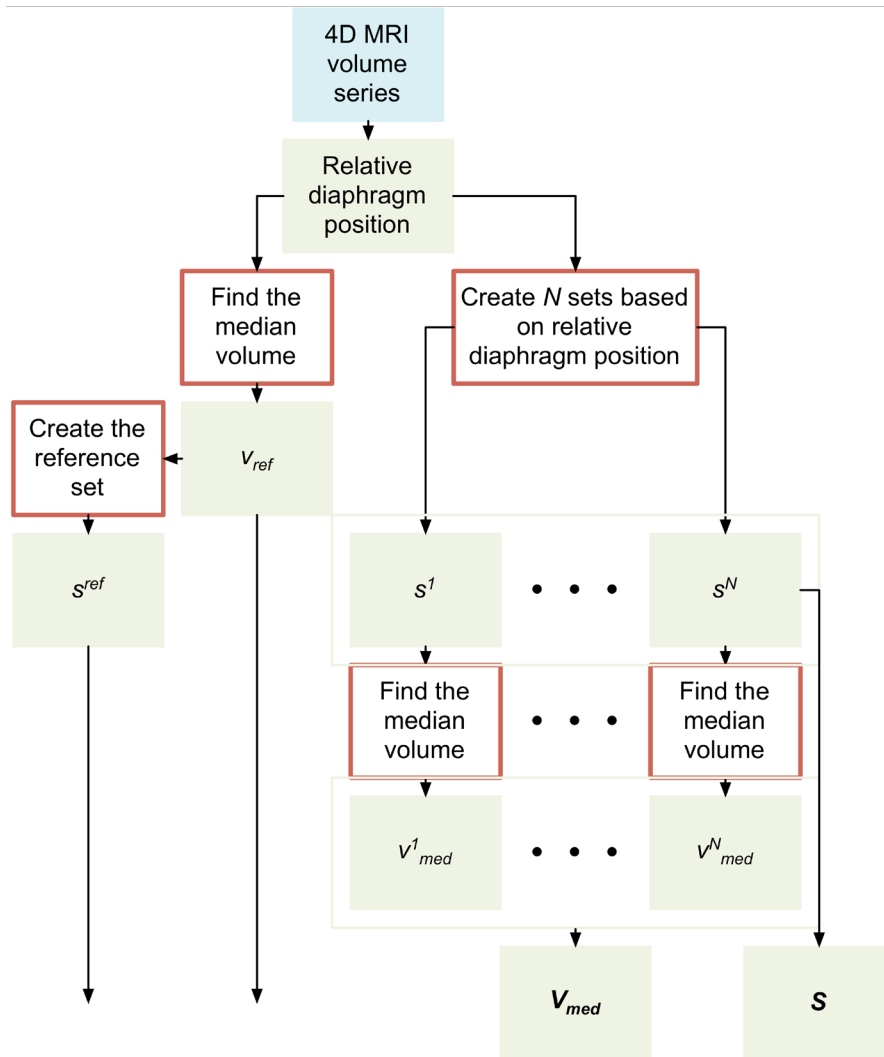


Figure 4-12 Detailed steps of grouping similar volumes based on relative diaphragm position.

1) The reference volume (v_{ref}) is registered to each volume within the reference set (s^{ref}). Deformation fields from the reference volume to each volume within the reference set ($\mathbf{r}_{(v_{ref} \rightarrow s^{ref})}$) are obtained.

2) The reference volume (v_{ref}) is registered to each representative volume (v_{med}^i) of volume set (s^i), generating the deformation field ($\mathbf{r}_{(v_{ref} \rightarrow v_{med}^i)}$).

3) Each representative volume (v_{med}^i) is registered to each volume within its corresponding volume set (s^i). Then we get deformation fields from registering representative volume to the volumes within the corresponding volume set ($\mathbf{r}_{(v_{med}^i \rightarrow v^j)}$, $v^j \in s^i$ AND $v^j \neq v_{med}^i$).

From the combination of the computed deformation fields, it is now possible to propagate the template volume, segmented using v_{ref} , to any volume of the 4D dataset. We hypothesize that the deformation from v_{ref} to any volume ($v^j \neq v_{med}^i$) can be computed with a minimal error as:

$$\begin{aligned} \mathbf{r}_{(v_{ref} \rightarrow v^j)} &= \mathbf{r}_{(v_{ref} \rightarrow v_{med}^i)} + \mathbf{r}_{(v_{med}^i \rightarrow v^j)} \\ v^j &\in s^i \quad \text{AND} \quad v^j \neq v_{med}^i \end{aligned} \tag{4.17}$$

This hypothesis will be validated using the accuracy of the automated segmentation results (see Section 4.4.2.1).

4.4.1.2 Deformable registration and stopping tolerance

The proposed scheme could be used for any deformable registration method. To demonstrate and evaluate the scheme, we implemented two widely used deformable registration algorithms (i.e. Demons and B-spline registration). As shown in Section 4.3, for both Demons and B-spline registration, the tolerance e is approximately inversely related to the relative diaphragm displacement. The power function in the plots of tolerance e versus relative diaphragm displacement (Figure 4-7 and Figure 4-8) showed good fitting results, with $R^2 = 0.957$ and 0.772 for Demons and B-spline registration respectively. As a

result, the tolerance e is adapted with respect to the relative diaphragm distances between any two pairs of registered volumes to optimize the iteration number using the exponential functions obtained:

For Demons registration, the function is:

$$e = 0.0343(\Delta d)^{-2.705} \quad (4.18)$$

and for B-spline registration,

$$e = 0.0006(\Delta d)^{-2.515} \quad (4.19)$$

where e is the tolerance value and Δd is the relative diaphragm displacement.

4.4.1.3 Evaluation

The basic registration-based segmentation scheme was implemented to benchmark the accuracy and computation amount of our proposed scheme. As there is no criterion for the basic scheme to choose the reference volume, two test cases were implemented:

Best case: Choose the reference volume whose relative diaphragm position is the median of all the volumes. This is the same way of choosing the reference volume as our proposed scheme. The maximum diaphragm displacement between two volumes is then: $d_{max}/2$.

Worst case: Choose the reference volume whose relative diaphragm position is at the maximum exhalation phase (or maximum inhalation phase) among all

volumes. The maximum diaphragm displacement between two volumes in this case is: d_{max} .

Accuracy

To validate our hypothesis of Equation (4.17), the accuracy of the proposed and the basic segmentation schemes are evaluated by comparing the segmentation results with ground truth. Three volumes within the 4D dataset for each subject were randomly chosen and segmented using ‘ITK-SNAP’ to serve as the ground truth. These ground truth were verified by an experienced clinician and edited where necessary. Dice’s similarity coefficient (DSC) is used to quantify how well two segmentations, A and B match each other. If two segmentations are identical, then DSC will be equal to 1. It will be 0 if A and B have no common voxel.

Computation amount

Our scheme is designed to limit the computational complexity of applying registration-based segmentation for 4D dataset segmentation. In order to evaluate the benefit of our scheme, the number of additions and multiplications were counted for the proposed scheme and for the basic scheme. The percentage reduction of computation amount is calculated as:

$$\text{reduction}(\%) = \frac{a_{basic} - a_{proposed}}{a_{basic}} \times 100 \quad (4.20)$$

where a_{basic} and $a_{proposed}$ consists of the number of additions and multiplications for the basic scheme and for the proposed scheme, respectively.

4.4.1.4 MRI data

To evaluate and demonstrate the proposed scheme, 4D MRI scans of the thorax of 3 healthy volunteers and 3 lung cancer patients were acquired and analyzed using TWIST sequence. The specifics of scans are the same as those presented in Chapter 3.

4.4.2 Study results

Both lungs and the tumor from all 6 subjects (30 volumes per subject) were successfully segmented using the proposed scheme. A total of 180 volumes were segmented. Representative segmented images using proposed scheme were shown in Figure 4-13. Three-dimensional models were also generated from segmented images. The method used to construct 3D models is the same as Section. 4.2 Chapter 4.

4.4.2.1 Accuracy

Figure 4-14 (a) and (b) show the DSC for left lung, right lung, and tumor of all subjects for schemes using demons and B-spline registration respectively. Proposed scheme achieved good segmentation accuracy, average $DSC_{left\ lung} =$

0.96 ± 0.01 , $DSC_{\text{right lung}} = 0.96 \pm 0.01$, and $DSC_{\text{tumor}} = 0.83 \pm 0.10$ using demons registration and average $DSC_{\text{left lung}} = 0.94 \pm 0.02$, $DSC_{\text{right lung}} = 0.95 \pm 0.01$, and $DSC_{\text{tumor}} = 0.81 \pm 0.10$ using B-spline registration. Friedman statistical test [174] is known for detecting differences in treatments across multiple test samples. The test was carried out using SPSS 18.0 for Windows [162]. Results showed that there are no significant differences between the three schemes tested in terms of segmentation accuracy. This implies that the proposed scheme achieved similar accuracy as the basic scheme.

4.4.2.2 Computation time/amount

All the registration-based segmentations were performed using Windows XP, on an Intel Xeon Processor (dual core, 3.00 GHz) with 9 GB RAM. All the schemes were implemented using MATLAB version 7.1.1 (The Mathworks, Inc, Natick)[175]. As the focus was on evaluating the computational improvement of the proposed scheme over the basic scheme, the MATLAB implementations used in this study were not particularly optimized for reduced computational cost and memory usage. Time for segmenting the entire 4D data set of one subject (thirty 3D volumes) was around 35 min for proposed scheme, 70 min (best case) to 123 min (worst case) for basic scheme.

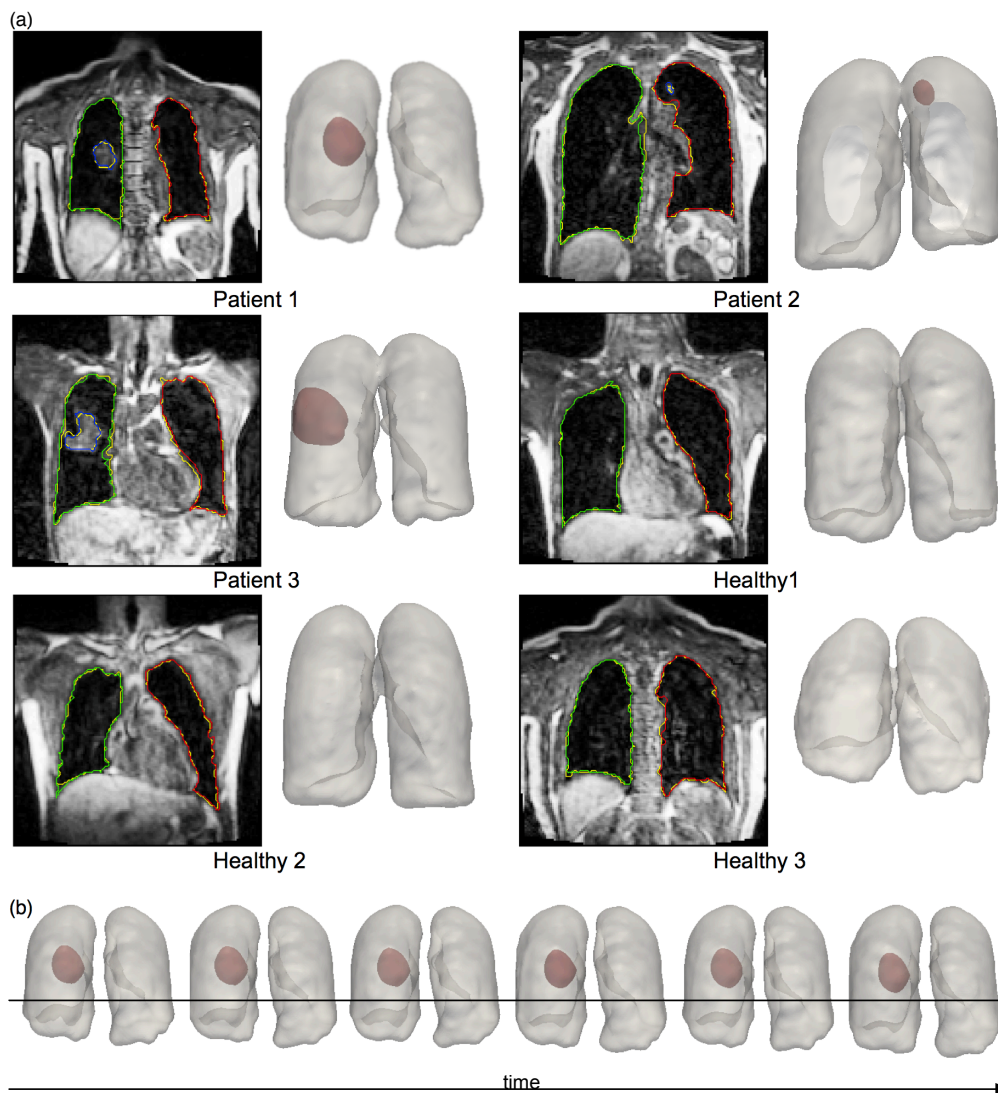


Figure 4-13 Representative sample segmented images using proposed scheme. (a) 2D slices and corresponding 3D models. Contours in red: left lung; Contours in green: right lung; Contours in blue: tumor; Contours in yellow: ground truth. (b) Representative sample 3D models constructed by automated segmented images of Patient 1 showing the movement of lungs and tumor over time.

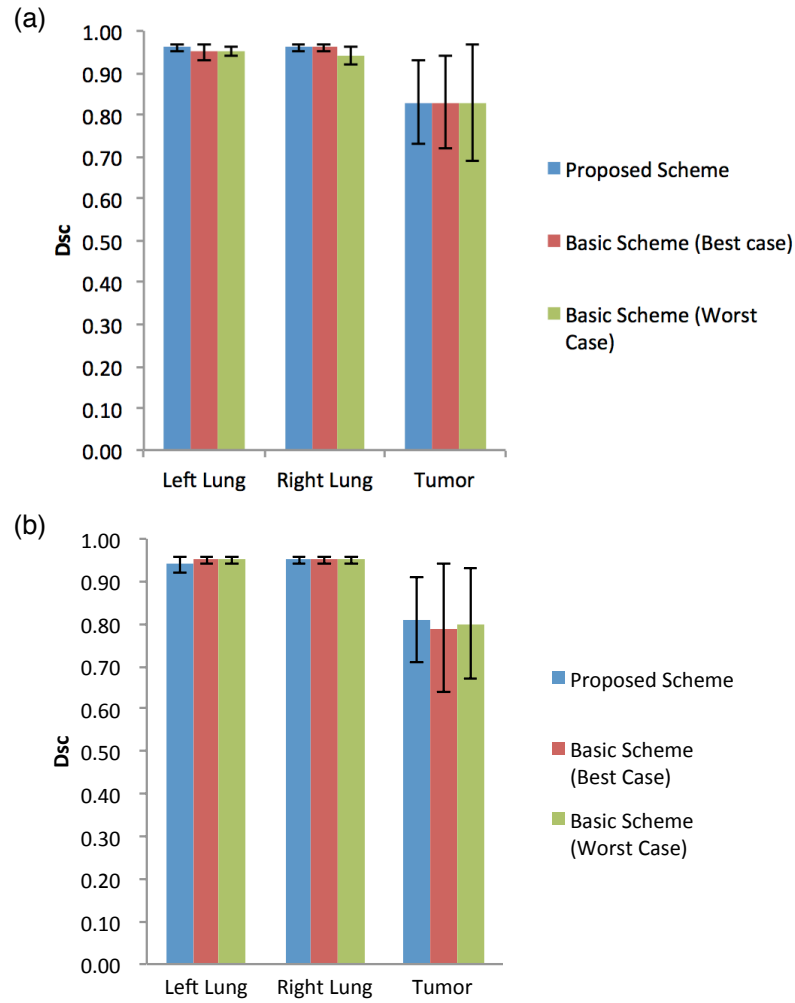


Figure 4-14 Accuracy results (average Dice's coefficient) of target structure segmentations for schemes using (a) demons registration and (b) B-spline registration

The average reduction of computation amounts (number of additions and multiplications) of schemes using demons and B-spline registration are shown in Figure 4-15. When counting the computational amount/time saving, the time counted includes pre-processing steps such as generating the 2DST image, grouping the volumes, and identifying control points. In the case of demons registration, the average reduction of computation amounts ranged from $44.01 \pm 10.42\%$ (best case) to $66.12 \pm 12.61\%$ (worst case). Improvement was

even better using B-spline registration, with $81.23 \pm 8.18\%$ (best case) to $92.85 \pm 5.37\%$ (worst case). The computational amount of the additional steps is negligible, for the ratio of computational amount of additional steps against the total amount less than 10^{-9} .

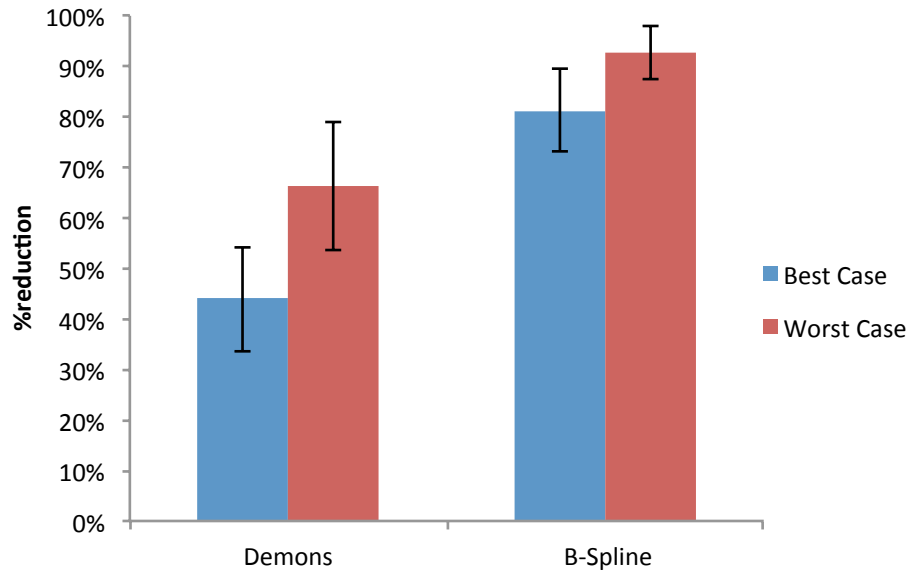


Figure 4-15 Percentage reduction of computation amounts (addition and multiplication) between proposed scheme and basic scheme (both cases) using demons registration and B-spline registration

The plots of maximum diaphragm displacement of each subject against the reduction of total computation amount (number of additions plus number of multiplications) are shown in Figure 4-16.

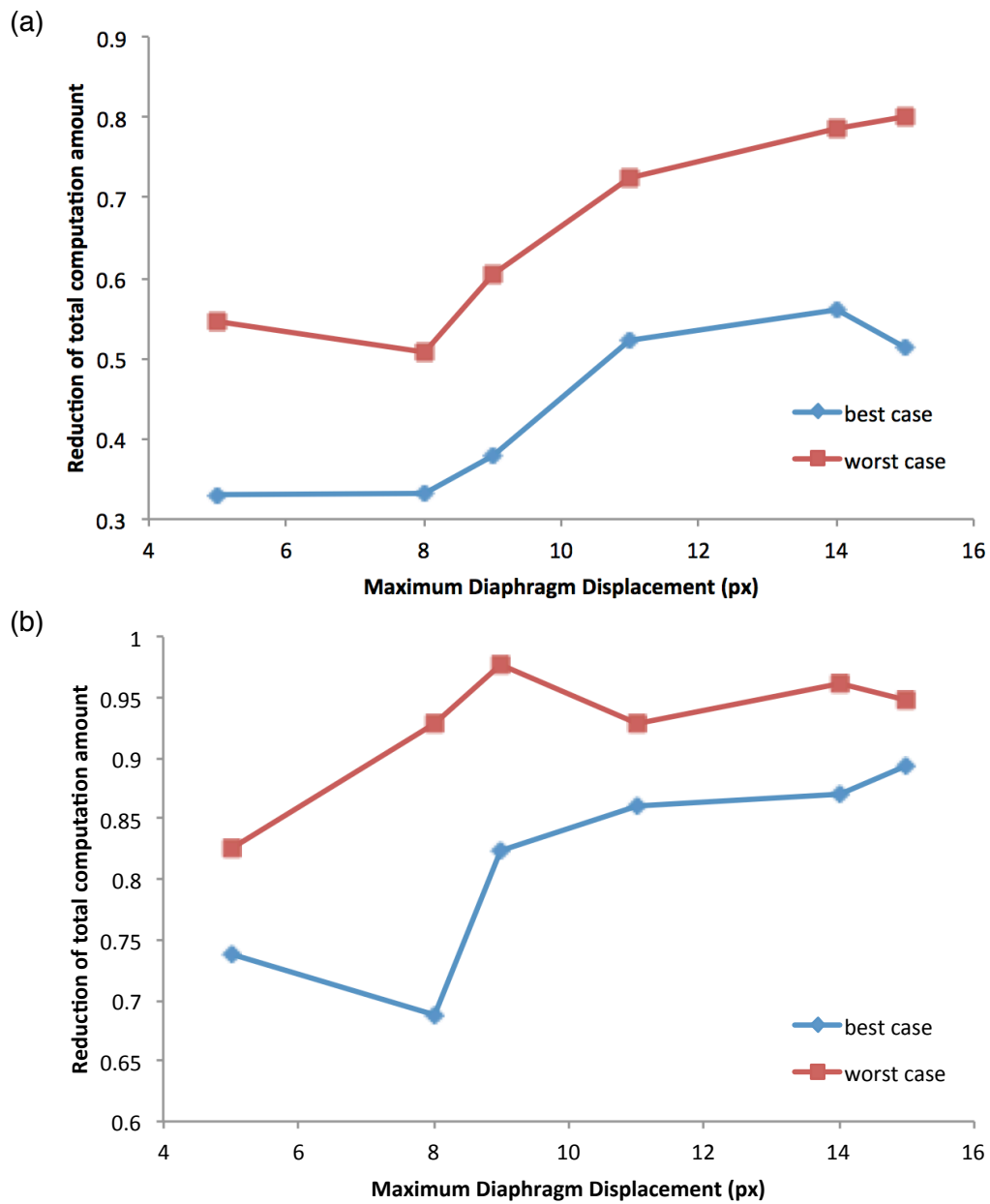


Figure 4-16 Plot of maximum diaphragm displacement of each subject against the reduction of total computation amount for proposed scheme using (a) demons registration and (b) B-spline registration

4.4.3 Study discussion

The proposed scheme has shown to be efficient in segmenting 4D thoracic MR images, achieving reduction in computational amount while maintaining good accuracy as compared to the basic scheme. Limiting the number of iterations by adapting the tolerance number to the relative diaphragm position has shown to be effective in reducing the computation amount. Grouping volumes based on relative diaphragm position has allowed only similar volumes to be registered, preventing registration of volumes with large differences that will take longer to converge.

In the proposed scheme, apart from representative volumes (v_{med}^i), which are directly registered to the reference volume, the deformation fields used to segment target volumes (v^i) within set s^i are combined from two registration steps: deformation fields from registering the reference volume to each representative volume ($\mathbf{r}_{(v_{ref} \rightarrow v_{med}^i)}$) and deformation fields from registering representative volumes to each volume within the corresponding volume set ($\mathbf{r}_{(v_{med}^i \rightarrow v^j)}$). In the basic scheme, all target volumes are directly registered to the reference volume. Therefore, the deformation fields obtained are $\mathbf{r}_{(v_{ref} \rightarrow v^j)}$. Since there is no significant difference between the proposed scheme and the basic scheme in terms of segmentation accuracy, it indicates that $\mathbf{r}_{(v_{ref} \rightarrow v_{med}^i)} + \mathbf{r}_{(v_{med}^i \rightarrow v^j)}$ is a good approximation of $\mathbf{r}_{(v_{ref} \rightarrow v^j)}$. It also shows that the propagation and accumulation of the registration error is negligible when only two steps of registration are performed. The volumes that are close to the reference volume v_{ref} (in terms of relative diaphragm displacement) are grouped into the reference set s^{ref} . In this way, v_{ref} can be

directly registered to each volume within s^{ref} . Thus the volumes within s^{ref} do not have to go through the process $\mathbf{r}_{(v_{ref} \rightarrow v_{med}^i)} + \mathbf{r}_{(v_{med}^i \rightarrow v^j)}$. The computational amount can be saved this way.

For all the schemes, a smaller DSC for the segmentation of tumor was obtained, especially for Patient 2 (Figure 4-13). This is likely due to the small size of the tumor. The voxel effects [176] become very significant in each step of the scheme and in the calculation of DSC. Any error in the deformable registration and other procedures results in a relatively significant mismatch.

The proposed scheme introduces additional steps compared to the basic scheme. These steps are the generation of 2DST images and the grouping of volumes based on relative diaphragm positions. However, the additional number of operations introduced by these steps was largely compensated by the computational complexity reduction made during the subsequent registration steps.

From Figure 4-16, it can be seen that when the range of the diaphragm movement (d_{max}) increases, the reduction in complexity by using the proposed scheme increases. For the basic scheme, the reference volume has to be registered to every volume with large differences (volumes at full-inhale and full-exhale phase), which increases the number of iterations for registration to converge. The larger the d_{max} , the more iterations are needed. By using the proposed scheme, the reference volume needs to be registered only once to each representative (v_{med}^i) of volume set (s^i). The other registrations take place between v_{med}^i and other volumes within s^i that are very similar. When more volumes are acquired within one 4D dataset, there will be more volumes with large differences from the reference volume (e.g. volumes at full-inhale and

full-exhale phase) since the lungs have a periodic motion pattern. Therefore, the improvement in terms of computation amount will be larger when the proposed scheme is used for 4D dataset with more volumes, which makes the proposed scheme especially useful to study the changes of pulmonary motion pattern over time. Moreover, the improvement will be greater if the proposed scheme is applied on volumes with higher spatial resolution, where the organ displacements are spread over a higher number of pixels.

In this study, when grouping similar volumes into sets we have set the x number to be 1 so that the diaphragm position between any two volumes do not differ more than 3 pixels. This is due to the relatively low spatial resolution of the images used in this study. With one pixel equals to 2.81mm in the physical space, we considered one pixel movement a large diaphragm displacement. Also, by setting x equals to 1, there are enough number of volumes within each set so that the efficiency of the proposed scheme is optimized. For different applications, especially for images with higher spatial resolution, one can set the x number to be larger than 1 to avoid creating too many sets with little differences between volumes within different sets and too few volumes within each set.

The proposed scheme is designed to be suitable for parallel computing. All the registrations can be performed independently in a parallel manner. This can lead to even faster segmentation of an entire 4D dataset and fall into realistic computational times in practice. Finally, the proposed scheme can also be potentially used for segmentation of other organs having periodic motion, such as heart and liver. For segmentation of 4D cardiac data, new spatio-temporal information has to be modeled instead of the relative diaphragm displacement.

A limitation of this study is that the tolerance value for registration to stop is application dependent. Preliminary training needs to be carried out for other applications (e.g. 4D MRI cardiac images, 4D MRI liver images) to acquire relationship between tolerance number and spatio-temporal information. Nonetheless, once this relationship is established, the scheme is automatic.

4.4.4 Study conclusion

This study presents an accurate and computational-saving registration-based segmentation scheme for 4D thoracic MRI data series. The scheme is fully automatic after initial segmentation to obtain the template volume. The proposed scheme incorporates spatio-temporal information about diaphragm movement to optimally choose the reference volume and to classify the other volumes into sub-groups. It also adaptively adjusts the tolerance value based on spatio-temporal information in order to lower the iteration number of registrations. The proposed scheme does not depend on any particular registration method. As demonstrated, it reduces computation amounts by up to 95% while maintaining accurate segmentations.

4.5 Chapter summary

In this chapter, the basic registration-based segmentation scheme using B-spline registration was first studied and shown to be an accurate approach to segment 4D-MRI thoracic dataset. However, it is not efficient to just directly apply the basic scheme to a 4D-MRI thoracic dataset that contains many 3D volumes. The relative diaphragm displacement was introduced as a new similarity measure for registration of 3D volumes with a 4D-MRI thoracic dataset. This is based on the fact that, for 4D-MRI thoracic dataset, the diaphragmatic movement causes the main difference between two 3D volumes. It was found that the tolerance value for registration to achieve accurate results is closely inversely related to the relative diaphragm displacement. Based on this finding, a novel spatio-temporal based scheme for efficient registration-based segmentation of thoracic 4D-MRI was proposed. The proposed scheme utilizes the relative diaphragm displacement to optimally choose the reference volume and to classify the other volumes into sub-groups. The tolerance value for registration to stop is also adaptively adjusted based on spatio-temporal information in order to lower the iteration number of registrations. The proposed scheme does not depend on any particular registration method. The proposed scheme saved up to 95% of computation amount while achieving comparable accurate segmentations compared to directly applying registration-based segmentation to 4D dataset. The scheme facilitates rapid 3D/4D visualization of the lung and tumor motion and potentially the tracking of tumor during radiation delivery.

Chapter 5 Fusion of 4D-MRI and static 3D-CT: creating simulated 4D-CT dataset

5.1 Chapter overview

Fusion of multiple image modalities is an interesting application as it combines different useful information into one image. The study presented in this chapter aims at bringing the advantages of MRI and CT, which are the high spatial-resolution and the ability to provide the electron density for RT dose calculation of CT, and MRI's ability to continuously acquire volumetric images over a long period of time without involving ionizing radiation. In this chapter, a novel method based on deformable image registration and Finite Element Method (FEM) was developed to fuse a static 3D-CT volume (acquired under breath-hold) and the temporal information extracted from 4D-MRI volumes, creating a simulated 4D-CT dataset. The study focuses on imaging for lung cancer RT. Comparing the simulated 4D-CT with the acquired 4D-CT of lung cancer patients based on landmarks, accurate results (error $\|E\| < 2$ mm) were achieved using the proposed method. The simulated 4D-CT dataset generated has high spatial resolution, can be used for direct dose calculation, and is able to

show continuous movement of tumor and organs over multiple breathing cycles.

5.2 Introduction

5.2.1 Motivation

As discussed in Chapter 2, one of the main advantages of MRI over CT is that MRI does not involve any radiation. As a result, 4D-MRI is able to continuously image for a prolonged time and to capture ‘real-time’ motion. The individual changes in respiration depth and frequency can be captured. Different breathing maneuvers can also be studied using 4D-MRI. However, visualization of anatomical details (e.g. vascular tree, lung fissures) within the lungs is limited in 4D-MRI because of the low proton density inside the lungs and the relatively low spatial resolution of MRI images. For special interests in RT, MRI lacks the electron density information to directly calculate the radiological dose applied to each voxel for treatment planning. On the other hand, CT is generally accepted as the gold standard to visualize the lung parenchyma because of its high spatial resolution. Furthermore, the Hounsfield units in CT images can also be used to calculate the radiation dose for RT. However, the high radiation involved in 4D-CT prohibits prolonged imaging. Only one averaged breathing cycle can be acquired. As a result, the individual changes in respiration frequency and depth cannot be captured. If the patients experience irregular breathing patterns, severe motion artifact will appear on the

images. Consequently, it would be beneficial if the advantages of MRI and CT can be fused together. That is to combine the high spatial resolution and intensity of CT and the motion information provided in 4D-MRI. The fused 4D dataset will contain 3D volumes over several breathing cycles. As a result, the detailed motion pattern of tumor and other organs can be studied. The fused 4D dataset will also have a high spatial resolution that could potentially increase the accuracy of target delineation for RT. The fused 4D dataset will have the Hounsfield units provided in the CT images, allowing the radiological dose to be calculated. The radiation during image acquisition will be kept to a minimum level, as only one volume of 3D static CT (dose: 1-10 mSv [48]) is required instead of using 4D-CT (dose: 30-40 mSv [49]).

Medical image fusion is an advanced image processing technique to integrate the information of multiple image modalities. Positron emission tomography (PET) and CT are often fused together as CT provides clear anatomical structures but lacks the functional and metabolic changes associated with the pathology that can be captured by PET. On the other hand, PET has low resolution and lacks anatomical structures for clinicians to reference. Fusion CT and PET aids the interpretation of both CT and PET [177-179]. Another important application using image fusion technique is the integration of the spatial information of CT and MRI. The fusion of CT and MRI was often used for the localization and delineation of prostate cancer because MRI has better soft tissue contrast than CT when differentiating the prostate gland from the periprostatic soft tissues while CT provides electron densities for dose calculation [42, 180, 181]. However, most of the image fusion application is focused on the combination of spatial information from different imaging modalities. A recent study by Miyabe et al. [182] created simulated 4D-CT

dataset by deforming a static 3D-CT using motion data extracted from 2D fluoroscopy. However, fluoroscopy still involves ionizing radiation and only captures 2D motion overtime. Prolonged scanning with fluoroscopy to study respiratory motion poses potential risk of radiation-induced injuries to patients [183].

With regards to extracting respiratory motion from images, deformable image registration is generally used. Respiratory motion information can be obtained by registering either 3D-CT scans acquired at exhale and inhale breath-holds (BH) [184, 185] or 3D volumes at different phases of 4D-CT dataset [186-188]. Displacement field estimations are directly extracted from the image data. However, as discussed in Chapter 2, the deformable registration algorithms are generally based on image intensity. For low-contrast regions, their intensity metrics are not sensitive to displacement changes, and the displacements in these low-contrast regions are usually regularized by regularization forces for non-parametric algorithms or by interpolations for parametric methods [189]. As a result, the registration accuracy in these regions is doubtful. Hence, the displacement fields generated using deformable registration in these low-contrast regions can not mimic the true respiratory motion [190]. The knowledge about mechanical processes of breathing and physical properties of organs are not taken into consideration in which the estimated displacement fields can be ‘unrealistic’ [191].

Biomechanical model [192-194] can be used to deal with the disadvantage of deformable registration, complementing deformable registration. To use biomechanical model, surface meshes representing lung structure at exhale and inhale phases are first constructed explicitly. Displacement of surface can be found by methods such as iterative closest point (ICP) [195] and deformable

model (see Section 2.3.1). Then it becomes a boundary value problem which is to estimate the internal displacement given the surface displacement of the model. This problem can then be solved by finite element method (FEM), which is a technique to calculate the displacement without using the image intensity. Physical material property is assigned to the elements in the model to ensure a realistic displacement of each volume element.

5.2.2 Finite Element Method

The method presented in this study uses deformable image registration to extract respiratory motion of lung surface from 4D-MRI dataset and then employs FEM to estimate the motion inside the lung area. A short review on the FEM will be presented.

For most of the practical problems that involve complicated geometries, material properties, and loadings (e.g. force, temperature), it is not possible to find the exact analytical mathematical solutions. Even the approximate solution of a given problem is often not convenient to be found. The Finite Element Method (FEM) aims to find the solution of a complicated problem through numerical methods by approximating the problem over simple sub-regions and then assembling them together [196]. Those interconnected sub-regions are called finite elements. These finite elements are connected to each other through nodal points. In the FEM, instead of solving the actual variation of variables (e.g. velocity, displacement, temperature) inside the entire body in one operation, the approximating functions are formulated in terms of the values of

the variables at the nodal points and combine them to obtain the solution of the whole body [197].

The solution of a problem by the FEM can be solved by the following steps [197, 198]. The displacement problem is taken as an example to explain each step.

1) Discretization of the structure and selection of the Element Types

The entire body of an object is first divided into many finite elements. This process is called discretization. The appropriate type, and arrangement of the elements must be assigned properly so that it fits the actual physical behavior. The element size and computational effort must be balanced. Smaller element size would generate more accurate results but would also result in larger computation amount. Typical finite elements used for problems in different dimensions are illustrated in Figure 5-1.

2) Selection of displacement model

A displacement model needs to be defined to use the values of nodal points to find suitable solution within the element. Generally, linear, quadratic, or cubic polynomials are frequently used functions because they are simple to calculate and implement.

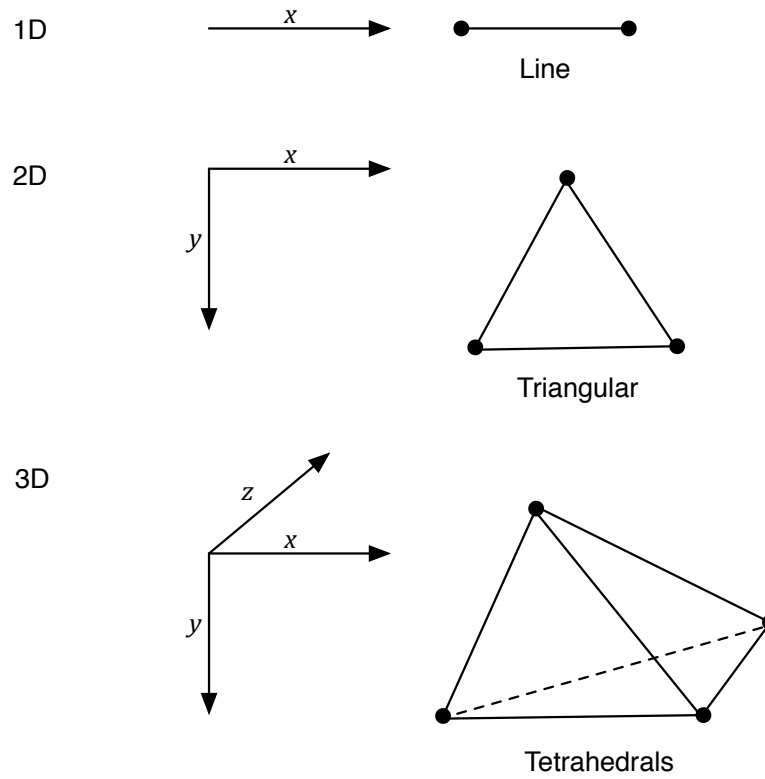


Figure 5-1 Typical simple finite elements defined for one-, two-, and three-dimensional problems. The elements showed here are low-order ones with nodal points only located at corners. For high-order finite elements, there are intermediate nodal points along edges.

3) Derivation of individual element stiffness matrices and element equilibrium equations

For each element, the element stiffness matrix $[k]$ is defined as:

$$\begin{Bmatrix} f_1 \\ f_2 \\ \vdots \\ f_n \end{Bmatrix} = \begin{bmatrix} k_{11} & k_{12} & \dots & k_{1n} \\ k_{21} & k_{22} & \dots & k_{2n} \\ \vdots & \vdots & \ddots & \vdots \\ k_{n1} & k_{n2} & \dots & k_{nn} \end{bmatrix} \begin{Bmatrix} r_1 \\ r_2 \\ \vdots \\ r_n \end{Bmatrix} \quad (5.1)$$

or in a compact form:

$$\{f\} = [k]\{r\} \quad (5.2)$$

where $\{f\}$ is the vector of the force applied on each element nodal point, $\{r\}$ is the corresponding vector of displacement of each nodal point and n is the total number of nodal points within the body. Work of forces at equilibrium conditions or the energy conservation is frequently used for the purpose of deriving the element stiffness matrices and equations of displacement problems [199].

4) Assembling the element equations to obtain the global equilibrium equation

Because the whole body is divided into several finite elements, the global stiffness matrix $[K]$ and the vector of global forces $\{F\}$ need to be derived from individual element stiffness matrices and forces:

$$[K] = \sum_{i=1}^n [k^{(i)}] \quad \{F\} = \sum_{i=1}^n \{f^{(i)}\} \quad (5.3)$$

where $[k^{(i)}]$ and $\{f^{(i)}\}$ are the individual stiffness matrices and force matrices for element i . The global equilibrium equation is formulated as:

$$\{F\} = [K]\{r\} \quad (5.4)$$

5) Solving for the unknown displacements of nodal points using boundary conditions

The global stiffness matrix $[K]$ is square and symmetric in most situations and is usually singular (determinant equals 0). Thus, boundary conditions (e.g.

displacements of nodal points at the boundary of the body) of the problem need to be incorporated to solve the global equation. The global equilibrium equations can be expressed as:

$$\begin{Bmatrix} F_1 \\ F_2 \\ \vdots \\ F_n \end{Bmatrix} = \begin{bmatrix} K_{11} & K_{12} & \dots & K_{1n} \\ K_{21} & K_{22} & \dots & K_{2n} \\ \vdots & \vdots & \ddots & \vdots \\ K_{n1} & K_{n2} & \dots & K_{nn} \end{bmatrix} \begin{Bmatrix} r_1 \\ r_2 \\ \vdots \\ r_n \end{Bmatrix} \quad (5.5)$$

For linear problems, the vector $\{r\}$ can be easily solved using elimination methods such as Gauss's method or iterative methods such as the Gauss–Seidel method [200].

5.3 Objective

The objective of this study is to develop a novel method to fuse the temporal information in 4D-MRI and the spatial information in static 3D-CT. Deformable image registration is used to derive displacement fields of the lung surface from 4D-MRI dataset. A FEM based approach is then used to estimate the displacements inside the lung area, because the displacement fields generated from deformable registration is not reliable in this area due to low image intensity.

5.4 Materials and methodology

5.4.1 Proposed scheme

The key concept of the proposed approach is to use the temporal information provided by 4D-MRI dataset to deform a static 3D-CT volume, forming a simulated 4D-CT dataset. Deformable registration and FEM are the two main techniques used to transfer the temporal information in 4D-MRI to the 3D-CT volume. As shown in Chapter 4, the segmented surface generated by registration-based segmentation method accurately fit to the target volumes, which indicates that deformable registration is accurate in high-contrast regions (e.g. lung/chest wall interface, lung/diaphragm interface). Thus, it gives the idea of using only the lung surface displacement fields (high-contrast regions) generated by deformable registration to serve as the boundary conditions in FEM to further estimate the displacement fields inside the lungs. The final displacement fields generated are used to transfer the temporal information in 4D-MRI to the 3D-CT volume.

The overall schema of the proposed method is illustrated in Figure 5-2. Schematically, the workflow of our framework can be summarized as follows:

- 1) Deformable registrations are performed between volumes in 4D-MRI dataset to extract the displacement fields (\mathbf{r}_{MRI}) between them.
- 2) A MRI volume in the same breathing phase of the 3D-CT is selected and registered to the 3D-CT volume in order to obtain the global displacement (\mathbf{r}_{global}) between MRI and CT.

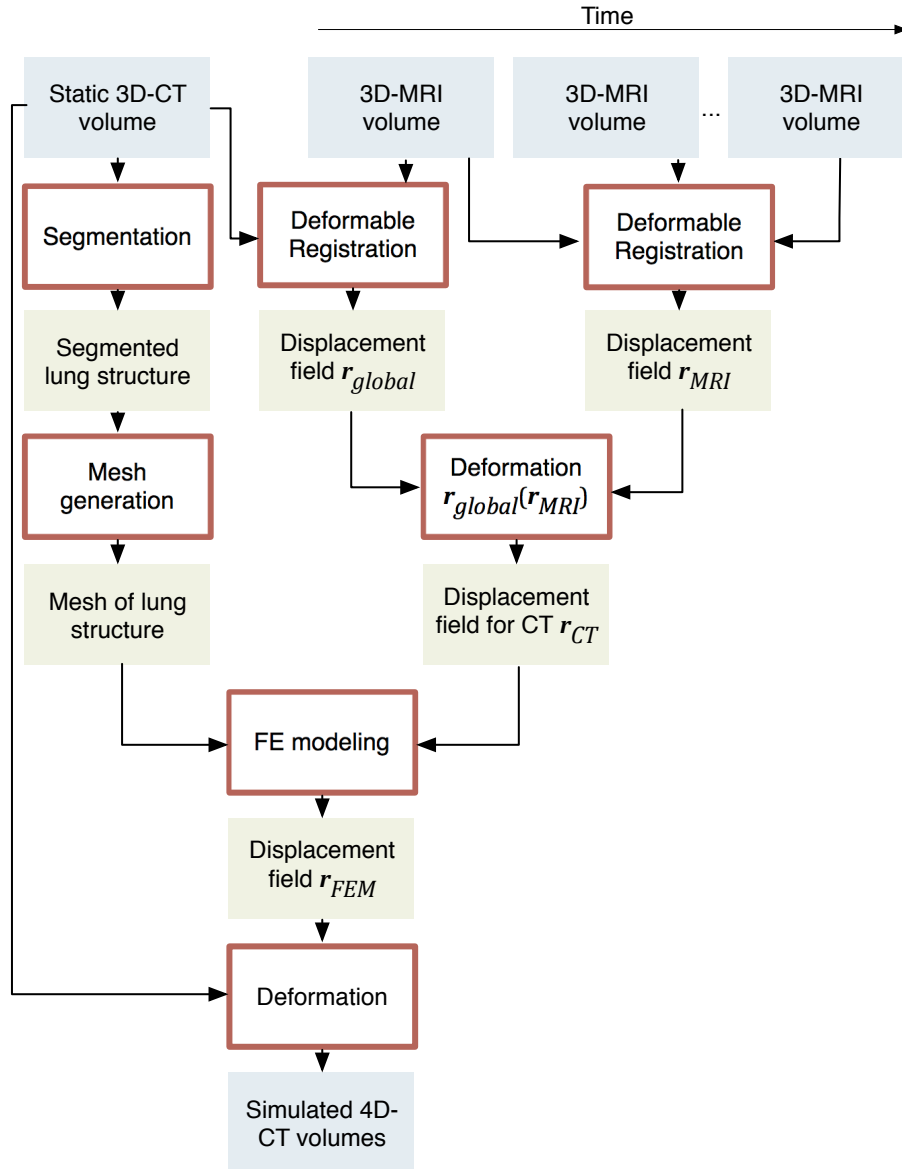


Figure 5-2 Overall scheme of proposed FEM approach to simulate 4D-CT volumes using static 3D-CT volume and 4D-MRI volumes.

3) The global displacement field (\mathbf{r}_{global}) is applied to deform the displacement fields between MRI volumes (\mathbf{r}_{MRI}) so that the displacement fields can be used to deform the 3D-CT volume. The deformed \mathbf{r}_{MRI} is denoted as \mathbf{r}_{CT} .

4) A volumetric tetrahedron mesh representing lung geometry for the finite element model is constructed using the 3D-CT volume.

- 5) The finite element model is used to compute the displacement within the lung structure (\mathbf{r}_{FEM}) using the displacement fields \mathbf{r}_{CT} as a prescribed displacement boundary condition.
- 6) The 3D-CT volume is then deformed by the displacement field generated from FEM (\mathbf{r}_{FEM}) to form a 4D-CT dataset.

The following sub-sections detail each step of the proposed scheme of generating the simulated 4D-CT dataset.

1) Registration between 4D-MRI volumes

The registration between 4D-MRI volumes is performed using the spatio-temporal based scheme with Demons registration developed in Chapter 4. A reference volume (v_{MRI}^A) is selected automatically based on its relative diaphragm position in the whole 4D-MRI dataset and registered to the rest volumes within the 4D-MRI dataset. The displacement fields from the reference volume to the rest volumes ($\mathbf{r}_{MRI}^{(v_{MRI}^A \rightarrow v_{MRI}^t)}$, $t = 1, 2, \dots, N$) are obtained.

2) Registration between the static 3D-CT volume and one MRI volume

The MRI volume (v_{MRI}^B) that is at the same breathing phase of the static 3D-CT volume (v_{CT}^{ref}) is first located. (For detailed method on sorting 4D-MRI volumes into corresponding phases of 4D-CT volumes, please refer to Section 3.3 Chapter 3.) Though the selected MRI volume (v_{MRI}^B) is at the same

breathing phase as the 3D-CT volume, there would still be some systematic differences between the two volumes due to patient positioning, imaging field of view (FOV), etc. Deformable registration is used to compensate such differences. The MRI volume (v_{MRI}^B) is registered to the CT volume (v_{CT}^{ref}) using B-spline registration. Since this is the registration between different modalities, mutual information is used as the similarity measure (as introduced in Chapter 2). The output displacement field is denoted as $\mathbf{r}_{global}^{(v_{MRI}^B \rightarrow v_{CT}^{ref})}$.

3) Generation of displacement fields for the static CT volume

Because the reference volume (v_{MRI}^A) selected in step 1 is based on its relative diaphragm position in the whole 4D-MRI dataset, it may not be the same volume (v_{MRI}^B) that matches the breathing phase of 3D-CT. It is necessary to generate the displacement fields from v_{MRI}^B to the rest of the volumes in 4D-MRI dataset ($\mathbf{r}_{MRI}^{(v_{MRI}^B \rightarrow v_{MRI}^t)}$). With $\mathbf{r}_{MRI}^{(v_{MRI}^A \rightarrow v_{MRI}^t)}$ generated in step 1, $\mathbf{r}_{MRI}^{(v_{MRI}^B \rightarrow v_{MRI}^t)}$ can be calculated as:

$$\mathbf{r}_{MRI}^{(v_{MRI}^B \rightarrow v_{MRI}^t)} = \mathbf{r}_{MRI}^{(v_{MRI}^A \rightarrow v_{MRI}^t)} - \mathbf{r}_{MRI}^{(v_{MRI}^A \rightarrow v_{MRI}^B)} \quad t = 1, 2, \dots, N \quad (5.6)$$

The displacement fields used to deform the 3D-CT volume (\mathbf{r}_{CT}) can be finally generated by applying \mathbf{r}_{global} to $\mathbf{r}_{MRI}^{(v_{MRI}^B \rightarrow v_{MRI}^t)}$ to compensate the global differences between 4D-MRI volumes and the 3D-CT:

$$\mathbf{r}_{CT}^{(v_{CT}^{ref} \rightarrow v_{CT}^t)} = \mathbf{r}_{global}^{(v_{MRI}^B \rightarrow v_{CT}^{ref})} \left(\mathbf{r}_{MRI}^{(v_{MRI}^B \rightarrow v_{MRI}^t)} \right) \quad (5.7)$$

where v_{CT}^t are the subsequent CT volumes within the 4D-CT dataset that are to be simulated.

4) Construction of volumetric tetrahedron mesh representing lung geometry

In order to perform finite element modeling, volumetric mesh representing lung geometry needs to be constructed first. The geometry of the lung is constructed using the 3D-CT volume v_{CT}^{ref} because the 3D-CT has higher spatial resolution. The lung structure of the 3D-CT volume is interactively segmented using ‘ITK-SNAP’ [18], which is a software used to segment 3D images based on the active contour methods [19]. A surface mesh is also generated from the segmented images using ‘ITK-SNAP’. This surface mesh is then exported into Meshlab (open-source 3D mesh processing software) [201] for successive smoothing and decimation to improve the mesh quality and to reduce the number of surface elements for computational efficiency during the finite element modeling. These smoothing and decimation steps are necessary as the initial surface mesh reconstructed from the segmented images contains (i) step-like artefacts that results in a block-like geometry for the lungs and (ii) excessive number of poor quality elements that may results in numerical instability during the finite element simulation (Figure 5-3). For mesh smoothing and decimation, the taubin smoothing and quadric-based edge collapse strategy algorithms implemented in Meshlab are used respectively. The choice of the two algorithms is based on the need for volume preservation during smoothing and maintaining geometrical features during decimation. The resultant surface mesh is then imported into Matlab to generate a volumetric

mesh for the finite element analysis using the iso2mesh toolbox (free Matlab/Octave-based mesh generation and processing toolbox) [202].

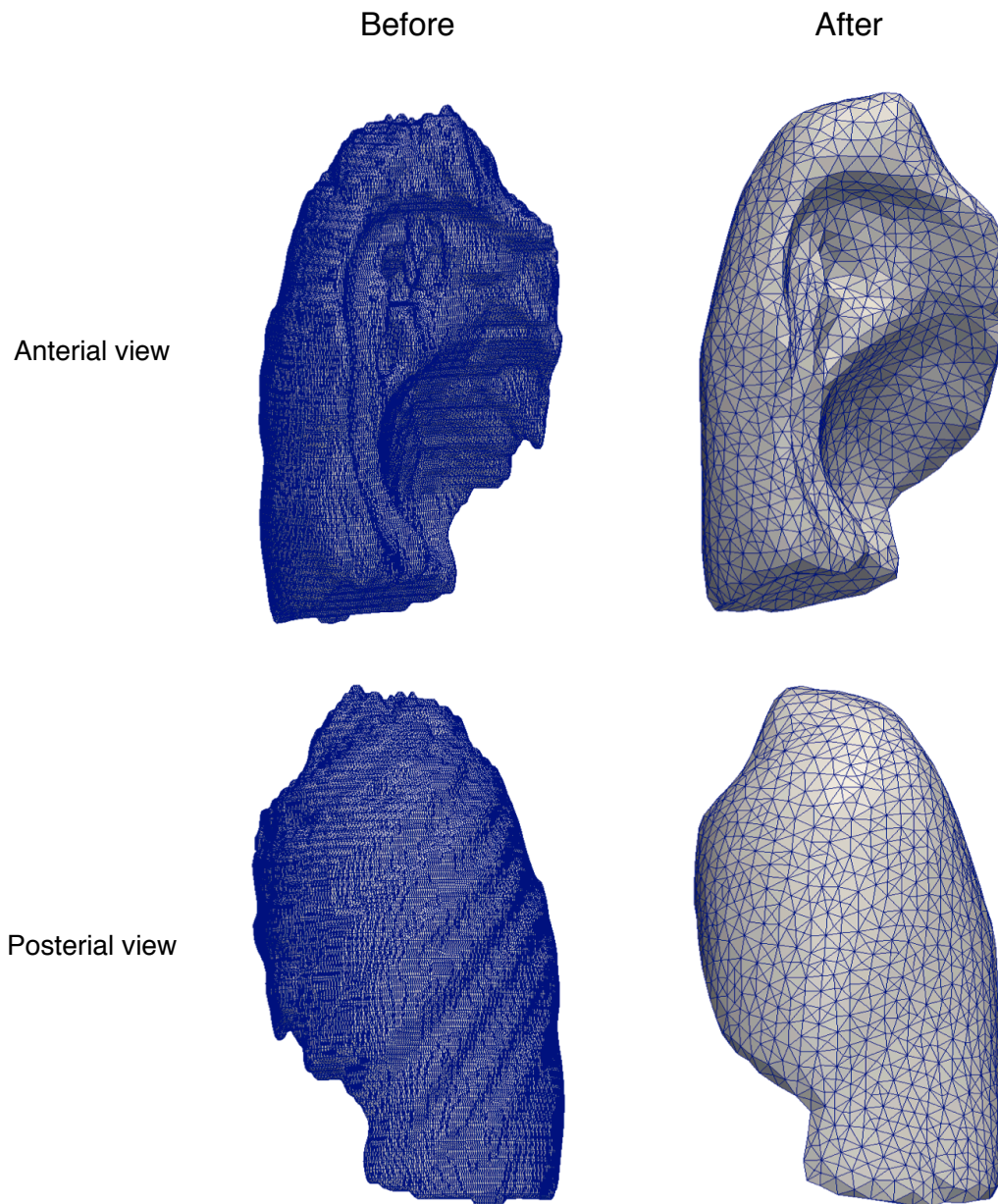


Figure 5-3 An example of the initial lung surface mesh and the smooth and decimated mesh after processing

5) Finite element modeling

The lung is modeled as an incompressible hyper-elastic Mooney-Rivlin solid [203] with the following parameters: elastic modulus (E) = 250 Pa and Poisson's ratio = 0.3 [204]. In this study, it is assumed that the lung tissue (including tumor) is homogeneous. Tumor information (location, size, motion, etc.) was not included in the FE modeling process. In our preliminary study, it was found that assigning different material property to the tumor only had minimal effect on the results. As a result, the tumor information is excluded in this study for the simplicity of the model construction.

The displacement fields (\mathbf{r}_{CT}) computed in step 3 are then applied as prescribed displacement boundary conditions on the surface of the finite element model in order to compute the interior deformation. The global equilibrium equation of the system (Eq. 5.5) can then be partitioned as:

$$\begin{bmatrix} K_u & K_{up} \\ K_{up}^T & K_p \end{bmatrix} \begin{Bmatrix} r_u \\ r_p \end{Bmatrix} = \begin{Bmatrix} F_u \\ F_p \end{Bmatrix}, \quad (5.8)$$

where r_u are the unknown displacements in the lung interior, r_p are the prescribed displacement on the surface of the lung, F_u and F_p are the external forces acting on the lung interior and lung surface respectively (if any) and $[K_u, K_{up}, K_p]$ are partitioning of the global stiffness matrix. The unknown displacements r_u can then be computed using the following equation:

$$[K_u]\{r_u\} = F_u - [K_{up}]\{r_p\}. \quad (5.9)$$

Essentially, the lung geometry is deformed from the shape of v_{CT}^{ref} to the shapes of the lung in the subsequent CT volumes. The displacement fields in the interior of the lung ($\mathbf{r}_{FEM}^{(v_{CT}^{ref} \rightarrow v_{CT}^t)}$) are then solved using FEBio (an open-source, nonlinear finite element solver) [21]. Finally, this interior lung deformation computed from the finite element model is then interpolated onto the image voxel grid to deform the CT volume.

6) Generation of simulated 4D-CT dataset

The CT volumes over time are simulated by deforming v_{CT}^{ref} with the corresponding displacement fields generated from FE modeling:

$$v_{CT}^t = \mathbf{r}_{FEM}^{(v_{CT}^{ref} \rightarrow v_{CT}^t)}(v_{CT}^{ref}) \quad (5.10)$$

5.4.2 Data

Scans of 4D-MRI using TWIST sequence and 4D-CT were acquired for six lung cancer patients. For details of image acquisition and image specifications, please refer to Chapter 3.

5.4.3 Evaluation

In order to evaluate the accuracy of the proposed scheme, 4D-CT dataset acquired of the patients were used. For each patient, CT volume at end-expiration (EE) or end-inspiration (EI) was selected as the reference CT volume v_{CT}^{ref} . The CT volumes at EI/EE and mid-inspiration (MI)/mid-expiration (ME) whose lung heights matched with 4D-MRI volumes were identified to serve as the ground truth for the simulated CT volumes to compare with.

For each patient, landmarks including prominent inner lung vascular and bronchial bifurcations are selected at the reference (EE/EI) CT volumes, the target CT volumes (EI/EE and MI/ME), and the simulated CT volumes [194]. All the landmarks were identified by an expert in lung anatomy and verified by an experienced radiation oncologist. The landmarks are located in different areas of the lung. For each lung, there are:

10 - 15 landmarks in the middle of the lung

10 - 15 landmarks near the lung border

10 - 15 landmarks close to the tumor (if any).

The landmarks are selected to be evenly distributed throughout the whole lung or tumor in order to assess the accuracy of the proposed method throughout the whole lung (Figure 5-4). The landmarks are divided into different sites to quantify the error in different regions.

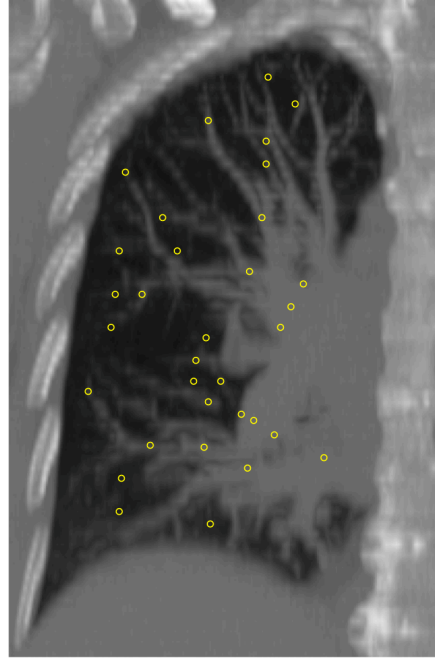


Figure 5-4 An example of the landmark points selected in the right lung of one patient. Landmarks are projected onto a single maximum intensity image for visualization. The landmarks are selected to be evenly distributed throughout the whole lung.

The same anatomical landmark that locates in the reference CT volume (v_{CT}^{ref}), target CT volume (v_{CT}^t) and synthetically generated target CT volume (v_{CT}^{sim}) is denoted as \mathbf{p}^{ref} , \mathbf{p}^t , and \mathbf{p}^{sim} respectively. All the landmarks are selected by an expert in lung anatomy and then independently verified by an experienced radiologist to ensure that there is no miss pairing of landmarks.

The actual displacement of landmarks from v_{CT}^{ref} to v_{CT}^t is calculated as:

$$\|P\| = \|\mathbf{p}^t - \mathbf{p}^{ref}\| \quad (5.11)$$

The error of landmark position in simulated CT volumes is defined by:

$$\|E\| = \|\mathbf{p}^t - \mathbf{p}^{sim}\| \quad (5.12)$$

The simulation of 4D-CT volumes using only the displacement fields from registration (r_{CT}) was implemented to benchmark the accuracy of the proposed FEM approach (Figure 5-5).

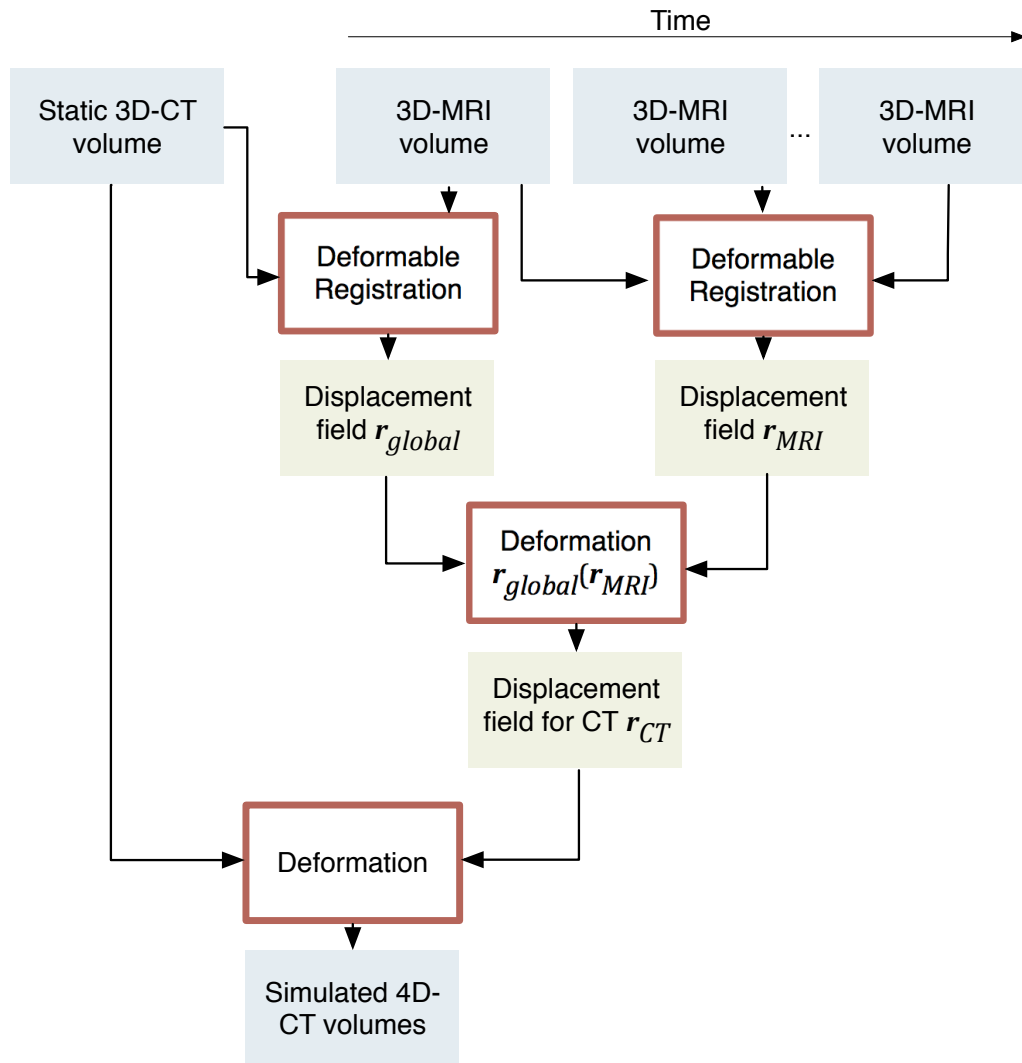


Figure 5-5 Overall scheme of simulating 4D-CT volumes using the displacement fields from registration directly. This is to benchmark the accuracy of the proposed FEM approach.

5.5 Results

Proposed FEM-based fusion approach has been successfully implemented using MATLAB version 7.1.1 (The Mathworks, Inc, Natick) [175] and simulated 4D-CT volumes for six patients were generated. The simulation of 4D-CT volumes has also been carried out by using only the displacement fields from registration (\mathbf{r}_{CT}). Volumes deformed using displacement fields generated with or without FEM approach exhibited visually comparable results. However, volumes deformed using FEM approach were more similar to the ground truth at some locations within the lung (marked by white arrows in Figure 5-6).

It is observed that the displacement fields generated by the two methods were different (Figure 5-7). For both methods, displacements with large magnitude were located at the interface between lungs and the diaphragm. However, for the displacement fields generated by deformable registration, other than the lung/diaphragm interface, the magnitude of the displacements inside the lung was quite small and the displacement vectors seem random. On the other hand, it is obvious to see a much smoother change of magnitude gradually from small to large, from cranial to caudal, in the displacement fields generated by the FEM approach.

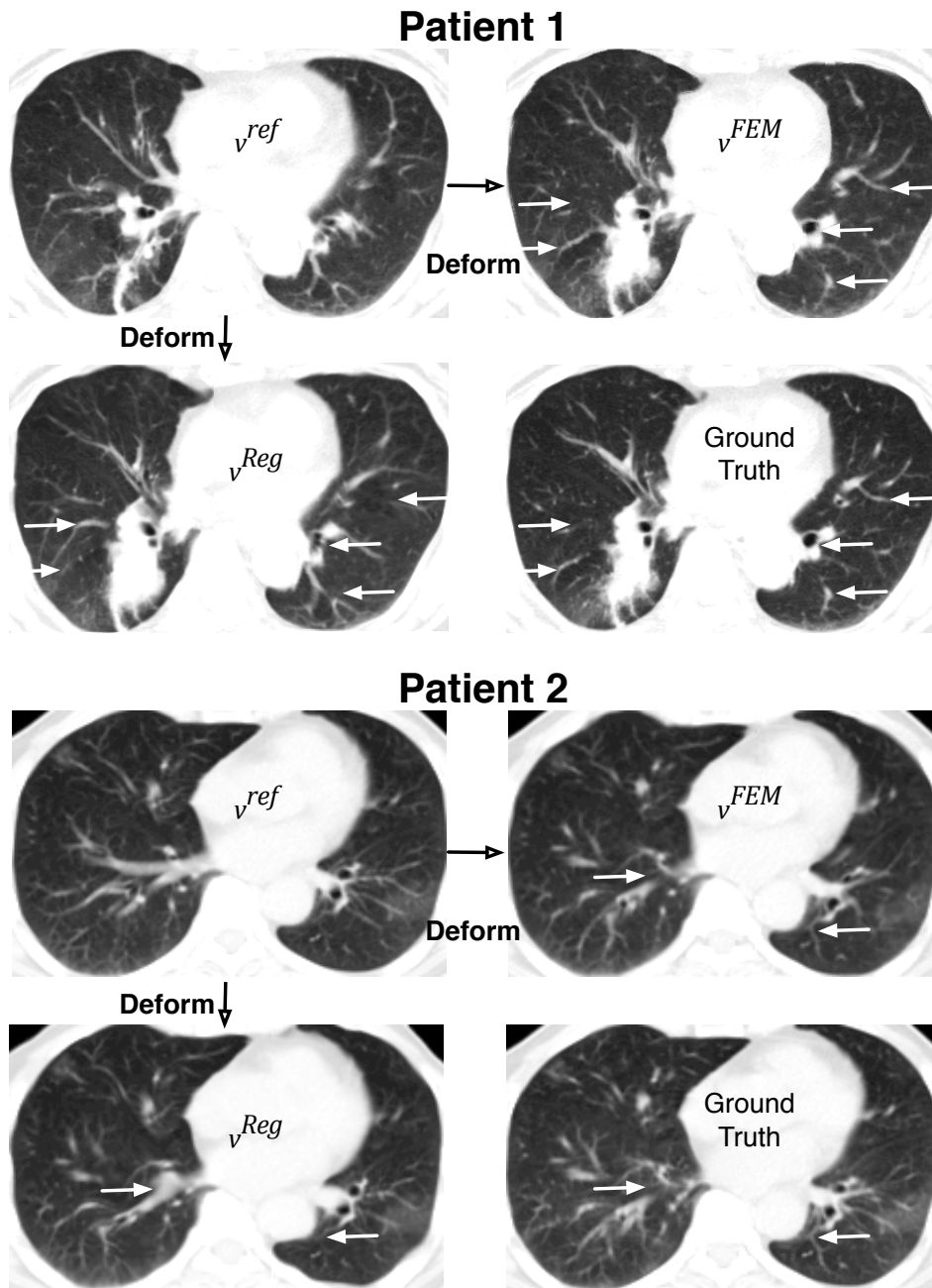


Figure 5-6 A comparison between the ground truth volume and simulated volumes deformed from the reference volume (v^{ref}) with the FEM method (v^{FEM}) and with the displacement fields generated from registration (v^{Reg}) of two patients. The window and level of the images are adjusted to enhance the visualization of small structures inside the lungs. The visible differences are marked by white arrows.

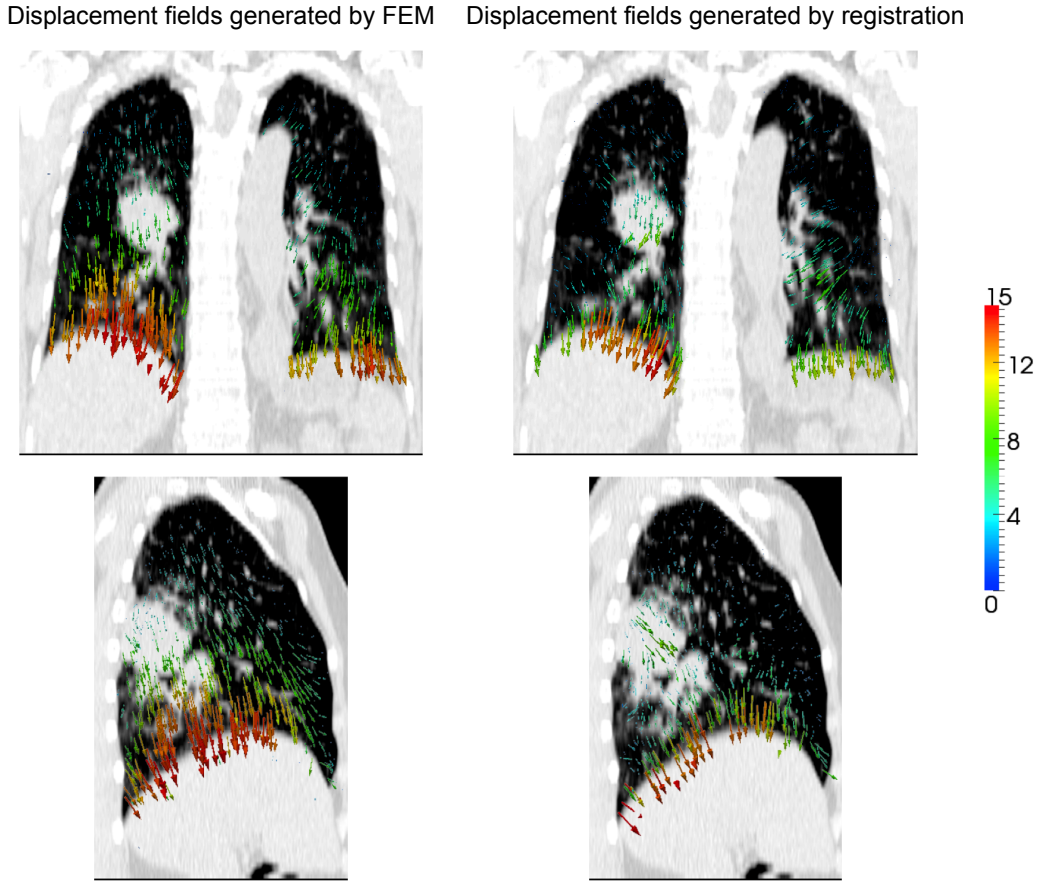


Figure 5-7 A comparison between the displacement fields generated by FEM and registration approaches. Magnitude of the displacements is color-coded: blue: small displacement; red: large displacement up to 15 mm.

A total of 420 landmarks were used to evaluate the accuracy of the proposed FEM approach to simulate the 4D-CT volumes. An example of landmark positions is shown in Figure 5-8. For target volumes at EI/EE, the averaged landmark displacement of all patients from v_{CT}^{ref} to v_{CT}^t is $\|P\| = 4.22 \pm 3.12$ mm for reference. The simulation error using proposed FEM approach was $\|E_{FEM}\| = 1.93 \pm 1.23$ mm while simulation error using displacement fields directly from deformable registration was $\|E_{Reg}\| = 3.28 \pm 2.07$ mm. The landmark distances for target volumes at EI/EE are listed in Table 5-1. Table 5-2 summarizes the landmark distances for target volumes at MI/ME. As

expected, the landmark motion from v_{CT}^{ref} to v_{CT}^t is smaller, with a value of $\|P\| = 2.72 \pm 2.22$ mm. The error of landmark position using proposed FEM approach was $\|E_{FEM}\| = 1.47 \pm 1.07$ mm while using displacement fields directly from deformable registration was $\|E_{Reg}\| = 2.27 \pm 1.57$ mm.

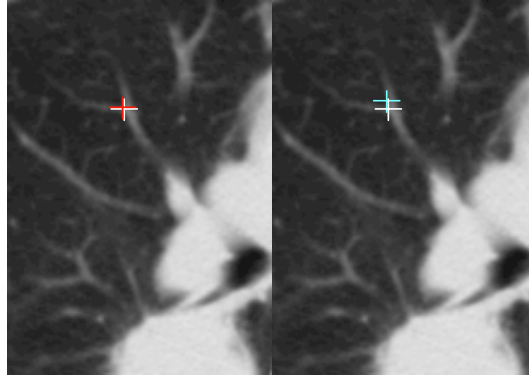


Figure 5-8 An example of a landmark in ground truth (white), CT volume simulated by proposed FEM approach (red), and CT volume simulated by directly applying displacement field generated from registration between MRI volumes (blue).

Table 5-1 Magnitude of the landmark displacement from v_{CT}^{ref} to $v_{CT}^t(\|P\|)$, and simulation errors using FEM approach ($\|E_{FEM}\|$) and registration method ($\|E_{Reg}\|$) for v_{CT}^t at EI/EE. Values are averaged over all the landmarks with standard deviation shown in bracket.

	$\ P\ $	$\ E_{Reg}\ $	$\ E_{FEM}\ $
Patient 1	4.39 (2.26)	3.29 (1.74)	1.85 (0.89)
Patient 2	3.09 (2.49)	2.67 (1.59)	2.09 (1.38)
Patient 3	4.44 (3.88)	3.39 (1.86)	1.96 (1.00)
Patient 4	3.42 (2.76)	2.29 (1.54)	1.42 (1.12)
Patient 5	5.31 (3.82)	4.54 (2.82)	2.50 (1.67)
Patient 6	4.52 (3.10)	3.65 (2.36)	1.97 (1.38)
Average	4.22 (3.12)	3.28 (2.07)	1.93 (1.23)

Table 5-2 Magnitude of the landmark displacement from v_{CT}^{ref} to $v_{CT}^t(\|P\|)$, and simulation errors using FEM approach ($\|E_{FEM}\|$) and registration method ($\|E_{Reg}\|$) for v_{CT}^t at MI/ME. Values are averaged over all the landmarks with standard deviation shown in bracket.

	$\ P\ $	$\ E_{Reg}\ $	$\ E_{FEM}\ $
Patient 1	2.16 (1.30)	1.98 (1.00)	1.25 (0.90)
Patient 2	2.23 (1.77)	2.09 (1.59)	1.38 (1.08)
Patient 3	2.64 (2.22)	2.44 (1.45)	1.49 (0.87)
Patient 4	2.86 (2.26)	1.77 (1.47)	1.51 (1.23)
Patient 5	4.91 (3.09)	3.58 (2.04)	2.16 (0.94)
Patient 6	2.24 (1.92)	2.20 (1.64)	1.31 (1.29)
Average	2.72 (2.22)	2.27 (1.57)	1.47 (1.07)

The simulation error in cranio-caudal (CC), lateral direction (RL), and antero-posterior (AP) were also calculated for FEM approach, with values of $\|E_{CC}\| = 1.03 \pm 1.50$ mm, $\|E_{RL}\| = 0.61 \pm 0.96$ mm, and $\|E_{AP}\| = 0.91 \pm 1.31$ mm respectively for target volumes at EI/EE (Table 5-3). For target volumes at MI/ME, the simulation error using FEM approach in CC, RL, and AP were $\|E_{CC}\| = 0.85 \pm 1.33$ mm, $\|E_{RL}\| = 0.47 \pm 0.79$ mm, and $\|E_{AP}\| = 0.56 \pm 0.84$ mm respectively (Table 5-4).

Table 5-3 Simulation errors using FEM approach at EI/EE in difference directions. Values are averaged over all the landmarks with standard deviation shown in bracket. Negative values of error in CC, RL, and AP direction mean the motion overestimation for the FEM approach in caudal direction, anterior direction, and leftwards respectively.

	E_{CC}	E_{RL}	E_{AP}	$\ E_{CC}\ $	$\ E_{RL}\ $	$\ E_{AP}\ $
Patient 1	0.38	-0.34	0.77	0.99 (1.21)	0.63 (0.87)	1.04 (1.09)
Patient 2	-0.08	0.04	-1.04	0.83 (1.38)	0.54 (0.92)	1.37 (1.59)
Patient 3	0.75	0.37	-0.25	1.47 (1.51)	0.67 (1.04)	0.60 (0.88)
Patient 4	0.77	-0.32	-0.24	0.82 (1.09)	0.62 (0.96)	0.35 (0.67)
Patient 5	0.12	-0.00	0.28	1.42 (2.29)	0.73 (1.04)	1.34 (1.68)
Patient 6	1.01	-0.32	-0.99	1.01 (1.42)	0.45 (0.74)	1.04 (1.06)
Average				1.03 (1.50)	0.61 (0.96)	0.91 (1.31)

Table 5-4 Simulation errors using FEM approach at MI/ME in difference directions. Values are averaged over all the landmarks with standard deviation shown in bracket. Negative values of error in CC, RL, and AP direction mean the motion overestimation for the FEM approach in caudal direction, anterior direction, and leftwards respectively.

	E_{CC}	E_{RL}	E_{AP}	$\ E_{CC}\ $	$\ E_{RL}\ $	$\ E_{AP}\ $
Patient 1	0.54	-0.03	-0.13	0.66 (0.90)	0.51 (0.80)	0.55 (0.79)
Patient 2	0.62	0.08	0.00	0.62 (1.12)	0.67 (1.00)	0.42 (0.71)
Patient 3	-0.02	-0.02	-0.32	0.97 (1.46)	0.22 (0.52)	0.52 (0.72)
Patient 4	0.77	-0.32	-0.24	0.82 (1.09)	0.62 (0.96)	0.35 (0.67)
Patient 5	0.25	-0.25	0.00	1.38 (1.85)	0.65 (0.87)	0.81 (1.20)
Patient 6	0.60	-0.21	-0.75	0.66 (1.26)	0.27 (0.52)	0.75 (0.76)
Average				0.85 (1.33)	0.47 (0.79)	0.56 (0.84)

Small differences are noticed in the accuracy of simulated volumes between landmarks in different regions (i.e. in the middle of the lung, near the boarder of the lung, and close to the tumor) (Table 5-5 and Table 5-6). For target volumes at EI/EE, the averaged errors are 1.99 ± 1.13 mm for landmarks in the middle of the lung, 1.95 ± 1.38 mm for landmarks near the boarder of the lung, and 1.73 ± 1.15 mm for landmarks near the tumor. For target volumes at MI/ME, the averaged errors were 1.60 ± 1.00 mm for landmarks in the middle of the lung, 1.56 ± 1.18 mm for landmarks near the boarder part of the lung, and 1.00 ± 0.82 mm for landmarks near the tumor.

The differences between landmark error of lungs with and without tumor are also very small (Table 5-5 and Table 5-6). For target volumes at EI/EE, the averaged errors were 1.78 ± 1.17 mm for lungs without tumor and 2.01 ± 1.26 mm for lungs with tumor. For target volumes at MI/ME, the average errors were 1.57 ± 1.08 mm and 1.42 ± 1.07 mm for lung without and with tumor respectively.

Table 5-5 Simulation errors using FEM approach for lungs with and without tumor for target volumes at EI/EE. Values are averaged over landmarks in different regions with standard deviation shown in bracket.

Landmarks	No tumor	With tumor	Average
Middle of the lung	1.69 (1.12)	2.22 (1.06)	1.99 (1.13)
Near the boarder	1.87 (1.20)	2.01 (1.48)	1.95 (1.38)
Close to the tumor	N.A.	1.73 (1.15)	1.73 (1.15)
Average	1.78 (1.16)	2.01 (1.26)	

Table 5-6 Simulation errors using FEM approach for lungs with and without tumor for target volumes at MI/ME. Values are averaged over landmarks in different regions with standard deviation shown in bracket.

Landmarks	No tumor	With tumor	Average
Middle of the lung	1.48 (0.87)	1.70 (1.09)	1.60 (1.00)
Near the boarder	1.66 (1.25)	1.46 (1.12)	1.56 (1.18)
Close to the tumor	N.A.	1.00 (0.82)	1.00 (0.82)
Average	1.57 (1.08)	1.42 (1.07)	

5.6 Discussion

The simulated 4D-CT dataset fused using 4D-MRI and 3D-CT combines the advantages of both modalities. The temporal information extracted from 4D-MRI enables studying of respiratory motion in ‘real-time’ instead of averaged breathing cycles. In addition, 4D-MRI provides realistic non-linear respiratory motion including hysteresis. The spatial information of 3D-CT contributes high image resolution and quality so that small structures inside the lung can be visualized and analyzed in details. Furthermore, electron density information is contained in the simulated 4D-CT dataset, which enables adaptive dose calculation for 4D-RT.

Overall accuracy was clearly better using the FEM approach than using displacement fields directly from deformable registration (1.93 vs 3.28 mm for target volumes at EI/EE and 1.47 vs 2.27 mm for target volumes at MI/ME). This result agrees well with *Zhong et al.* [189]. They proposed a FEM approach

that uses the displacements of the Demons registration in high-contrast regions to generate displacement fields over the entire image domain. They only focused on CT images and their method was successfully applied on prostate and lung CT images. In their study, the FEM correction method reduced the average error of the Demons registration by 6 mm. In our study, the larger errors produced by directly applying the displacement fields from registration can be attributed to the lack of visible structure inside the lung in MR images due to low proton density and low spatial resolution. Since the deformable registration applied between 4D-MRI volumes is based on image intensity, the displacement fields in the entire image domain depends on the intensity gradients between voxels. For low-contrast regions (i.e. inside the lungs), the difference in intensity between the adjacent voxels is small, resulting small displacements. This can be seen in Figure 5-7. In addition, the voxel intensity difference in the low-contrast regions derived using image registration may be due to noise instead of real differences in structures. Consequently, the displacement fields in the low-contrast regions may not be reliable. On the other hand, deformable registration in the high-contrast regions (i.e. interface between lungs and chest wall, diaphragm, and heart) has been proved to be accurate (see Chapter 4, the lung structure is well segmented using registration-based segmentation). It is reasonable to take displacements in those high-contrast regions as the input to the surface of the FE model. The FE method does not suffer from the disadvantage in the low-contrast regions as registration does because the internal displacement in FEM is totally based on the mechanical property and the final geometry of lungs. The FEM approach ensures a physically meaningful displacement. The displacement in the low-contrast regions can be estimated (Figure 5-7) and was shown to be reasonably accurate in our study.

There is no systematic over- or under-estimation noticed in the motion estimation in CC, RL, and AP directions in the simulated CT volumes (Table 5-3 and Table 5-4). The errors in CC direction are slightly larger than those in RL and AP direction. This is probably because the lung motion is most prominent in CC direction, which makes it harder for FEM to predict the motion. Further, one should note that the spatial resolution in CC direction is relatively low (3 – 5 mm). It is more difficult to achieve high simulation accuracy with such resolution. Nonetheless, the errors using proposed FEM approach are less than 0.4 mm in CC direction, which is quite acceptable.

With regards to the landmarks in different positions, the simulation accuracy in the middle of the lung is similar to that near the lung borders. This finding agrees well with *Werner et al.*'s results [194]. They proposed a biomechanical model extracted from thoracic 4D-CT dataset to estimate respiratory motion. In their work, tumor information was ignored in the biomechanical model. Our study further showed that it is reasonable to assume that the lung tissue is homogeneous. However, it is surprising to see that excluding tumor does not affect the simulation accuracy. The simulation accuracy close to the tumor is similar to that in other regions. The difference between lungs with and without tumor is also very small. This result is different from what *Werner et al.* [194] reported. In their work, overall modeling accuracy decreased for tumor bearing lungs. Such difference in results could be because the patients in this study did not suffer loss in lung mobility and change in the elasticity of lungs due to the tumor. The assumption on lung homogeneity is still valid for tumor bearing lungs. This further indicates that it is not possible to predict the effects of tumor only based on its size and location. Patient specific analysis is necessary.

In this study, the registration between v_{MRI}^B and v_{CT}^{ref} was performed by moving v_{MRI}^B to v_{CT}^{ref} . The resulting displacement field \mathbf{r}_{global} was then applied to $\mathbf{r}_{MRI}^{v_{MRI}^B \rightarrow v_{MRI}^t}$ so that it can be used to deform v_{CT}^{ref} . The reason the global registration was taken from MRI to CT volume is that 4D-CT volumes at other breathing phases can be used as ground truth to validate the simulation results. In fact, the global process can be performed in the opposite way, to move v_{CT}^{ref} to v_{MRI}^B . The displacement fields $\mathbf{r}_{MRI}^{v_{MRI}^B \rightarrow v_{MRI}^t}$ can then be directly used to deform the registered v_{CT}^{ref} . However, how to evaluate the accuracy this method remains an open question as the lack of ground truth.

This study showed that it is possible to fuse temporal information from MRI and spatial information of CT together. The concept in this study could potentially be used to fuse other imaging modalities, e.g. ventilation-weighted MRI with CT. The fused image could display dynamic change of gas that is contributed by ventilation-weighted MRI and details of structures inside the lung from CT. This could be potentially used to study other lung diseases such as chronic obstructive pulmonary disease (COPD) in which regional information of the lung in motion will be beneficial.

A limitation of this work could be the validation method. In this work, the accuracy of proposed method is validated by comparing the simulated CT volumes from 4D-MRI volumes with the 4D-CT volumes at the corresponding breathing phases. Though the lung height is matched between the 4D-MRI volumes and 4D-CT volumes, the matched MRI and CT volumes are not exactly the same. The global registration between MRI and CT volumes could not completely eliminate such differences. Thus, there exists a systematic error

due to the differences between MRI and C volumes. However, since currently it is not possible to acquire MRI and CT volumes at the same time, the validation method used in this study could still be the best way.

5.7 Conclusion

This chapter presented a novel method to generate simulated 4D-CT volumes from a static 3D-CT volume and 4D-MRI volumes. The proposed method extracts temporal information about lung movement from 4D-MRI volumes through deformable registration. Due to the lack of visible structures inside the lungs in MRI volumes, the displacements inside the lungs are not reliable. Consequently, only the lung surface displacements are used to serve as the boundary conditions in the FEM modeling to estimate the displacements inside the lung. The proposed method achieved accurate results, with an average error less than 2 mm based on landmark positions. This work successfully fused the advantages of 4D-MRI and 3D-CT such that the simulated 4D-CT dataset has high spatial resolution, can be used for direct dose calculation, and is able to show continuous movement of tumor and organs over multiple breathing cycles.

Chapter 6 Summary and future work

6.1 Chapter overview

In the earlier chapters of this thesis, we have presented the development of new methods for the use of 4D-MRI in different stages of 4D-RT. This includes determining suitable 4D-MRI sequence for imaging lung cancer for RT, developing automatic target structure delineation method, and the fusion of 4D-MRI and 3D-CT for dose calculation. In this chapter, the complete integrated system based on 4D-MRI dataset for 4D-RT planning is presented. The significance of this thesis is summarized. This chapter also provides the future work of this thesis.

6.2 Integration of the 4D-MRI based system for 4D-RT of lung cancer patients

In Chapter 1 introduction, we have discussed the importance of incorporating the temporal information into RT process for tumors with high mobility such as lung cancer. The development of advanced 4D-MRI imaging techniques offers enhanced dynamic imaging. Thanks to the nature of MRI, which does not involve any radiation, 4D-MRI is capable of providing the information about the 3D motion of organs and structures over tens of minutes. However, before 4D-MRI can be used in daily clinical practice of 4D-RT, there is a lack of validated, standardized planning tools, including accurate and automated multiple target structures segmentation, adaptive dose calculation, and motion control delivery mechanism. As a result, a complete system that is based on 4D-MRI for 4D-RT of lung cancer patients was developed in this thesis. The overall scheme of the proposed system is illustrated in Figure 6-1. The following sections detail on each step of the proposed system.

1) Image acquisition

For each lung cancer patient that is suitable for CT, MRI scanning and RT, a static 3D-CT volume and a 4D-MRI dataset are acquired. The total acquisition time of 4D-MRI is short (< 5 min). Consequently, using 4D-MRI does not increase the total scanning time as compared to 4D-CT. In Chapter 3, we have shown that the 4D-MRI sequence TWIST exhibited acceptable image quality while is sufficient to study the motion of tumor and diaphragm under controlled

breathing, owing to its high temporal resolution (0.9 volume/s). In addition, volumes acquired by TWIST MRI sequence correlated well with 4D-CT, the current gold standard modality of lung imaging, in terms of presenting tumor volume and describing tumor motion. Consequently, the MRI sequence TWIST is selected to scan the patient. The static 3D-CT acquired is to provide high spatial resolution images, detailed structures inside the lungs, and the electron density information that can be used for dose calculation. A limitation that 4D-MRI faced is that it is currently only suitable for slow breathing (6 s/cycle). However, with the rapid development, we expect the temporal resolution of 4D-MRI to improve in the near future which will make it suitable for fast free breathing.

2) Registration-based segmentation of 4D-MRI

After the 4D-MRI dataset is acquired, target structure will be segmented by using the spatio-temporal based scheme developed in Chapter 4 for efficient registration-based segmentation of thoracic 4D-MRI. This segmentation approach is fully automatic after the initial semi-automatic segmentation of the reference volume. This scheme utilizes the displacement of the diaphragm extracted from the 4D-MRI dataset to optimally select the reference volume and to classify the other volumes into sub-groups to perform deformable registration. The tolerance value for registration to stop is also adaptively adjusted based on spatio-temporal information in order to save the unnecessary computation time/amount introduced by excess iteration number of registrations without the loss of accuracy. The outputs of this process are the segmented volumes representing the geometry of tumor and organs at risk and the

displacement fields from the reference volume to the other volumes of the 4D-MRI dataset.

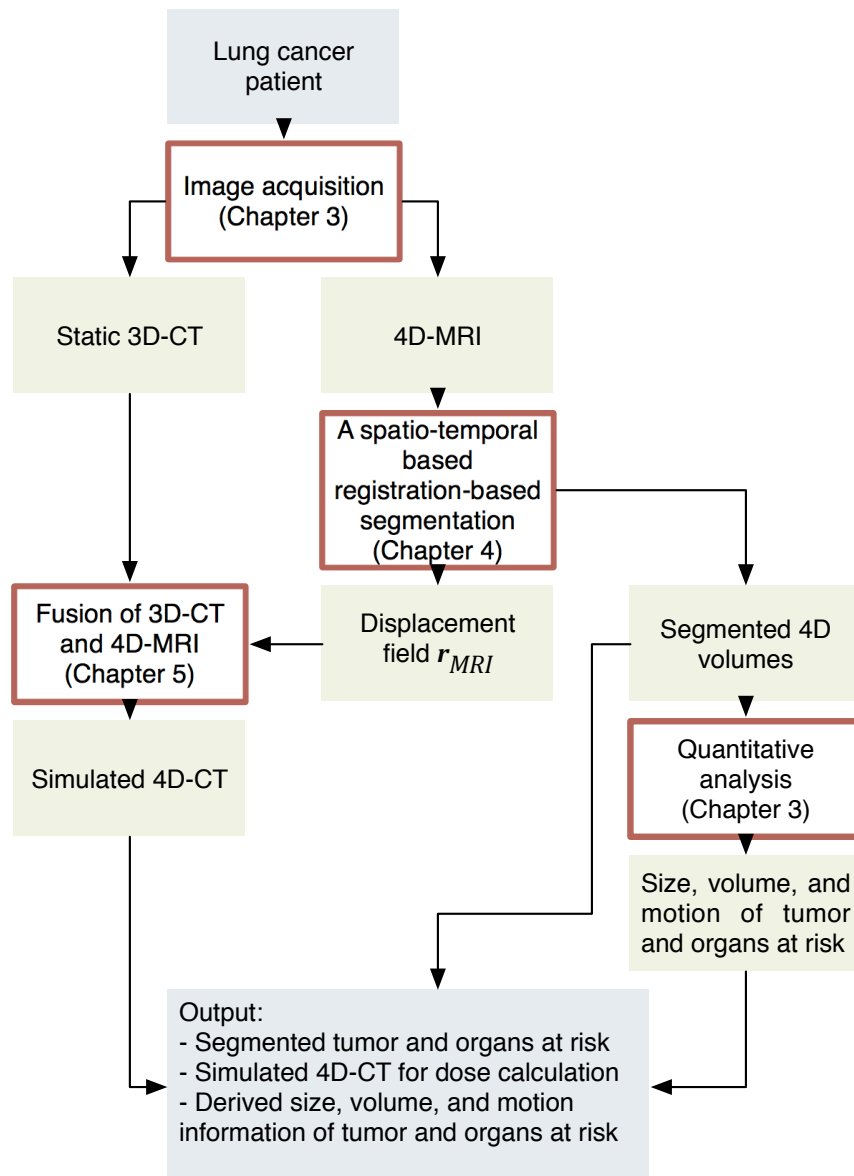


Figure 6-1 Overall schematic of the 4D-MRI based system proposed in this thesis

3) Fusion of 4D-MRI and 3D-CT to generate simulated 4D-CT dataset

A novel method to generate simulated 4D-CT dataset has been developed in Chapter 5. A simulated 4D-CT dataset is generated by fusing the spatial information of the static 3D-CT volume and the temporal information extracted from the 4D-MRI dataset. The spatial information refers to the spatial resolution and image intensity of the 3D-CT volume while the temporal information is displacement fields between MRI volumes generated in step 2. Due to the lack of visible structures inside the lungs in MRI volumes, the displacements inside the lungs are not reliable. Consequently, only the lung surface displacements are used. The FEM modeling is applied to estimate the displacements inside the lung taken the displacement fields of lung surface as the boundary condition. The final displacement fields generated by the FEM modeling are then used to deform the 3D-CT volume to form a simulated 4D-CT dataset. The simulated 4D-CT dataset has high spatial resolution, can be used for direct dose calculation, and is able to show continuous movement of tumor and organs over multiple breathing cycles.

4) Quantitative analysis of tumor and other organs at risk

With accurately segmented tumor and other organs at risk generated in step 2, quantitative analysis of these structures can be performed. The quantitative analysis includes calculation of the size, volume, and the motion pattern of the tumor and other organs at risk. Such quantitative analyses have already been employed in Chapter 3 to evaluate the performance of 4D-MRI sequences at 3T. Combined with the electron density information provided by the simulated

4D-CT dataset generated in step 3, a detailed therapy plan for 4D-RT can be made. This detailed plan can then be used during 4D-RT treatment.

6.3 Significance of this thesis

In order to improve the current 4D-RT process, a novel 4D-MRI based system for 4D radiotherapy of lung cancer patients is proposed in this thesis. This new system can be served as a complement to current CT based RT system that involves high ionizing radiation exposure during image scanning.

With the development of fast and high dimensional imaging techniques such as 4D-CT and 4D-MRI, there is increasing interest in understanding the uncertainties and variations of the tumor and other organs at risk during breathing. Recent development of fast acquisition techniques of MR imaging has enabled studying the respiratory motion of organs and tumors. With no radiation involved, 4D-MRI can be performed continuously in real-time which makes it possible to scan for a longer period of time and to cover individual changes of respiratory motion. Recently, the 3T high field MRI scanner has been available for clinic. However, the performance of 4D-MRI sequences for lung cancer imaging at 3T is still unclear. Hence, three commonly used 4D-MRI sequences for lung imaging were evaluated in this thesis. Our results showed that TWIST is the most suitable sequence among the three sequences studied for 4D lung imaging of lung cancer patients. This thesis also demonstrated that 4D-MRI exhibited comparable ability to present the tumor

volume and to describe the tumor motion as 4D-CT, which shows that 4D-MRI could be an alternative option of lung imaging. 4D-MRI fills the gap between the short-term and averaged representation of only a few regular breathing cycles (in 4DCT), and the long-term investigation of the tumor and organs at risk responses to the treatment (a few weeks/months). The ability of 4D-MRI to continuously scan over tens of minutes provides valuable 4D information about the respiratory motion.

To manually segment a 4D dataset for RT planning would be extremely tedious and time-consuming as a 4D dataset typically contains tens of 3D volumes. Manual segmentation could also result in high intra- and inter-user variability. In this thesis, a spatio-temporal based scheme for efficient registration-based segmentation was developed for the purpose of segmenting multiple structures of tens of 3D thoracic MRI volumes. Results showed that this novel registration-based segmentation scheme is capable of reducing the computation amount/time that is required by the basic scheme while maintaining the segmentation accuracy. The scheme is fully automatic after initial segmentation to obtain the template volume. Thus, the user intervention is kept to a minimum level. This scheme enables fast segmentation of the entire 4D dataset. As a result, the efficiency of target delineation of multiple structures is greatly improved and the manpower is saved.

The accurately segmented volumes serve as the basis for quantitative analysis. The basic information such as size and volume of structures of interests can be easily calculated with the segmented volumes. More importantly, individualized 4D information of structures of interests, such as variations of location, deformation, and rotation overtime, can be derived from tens of the segmented volumes overtime of each patient. Such 4D information

cannot be retrieved by external respiratory signal or through the population based estimation but can only be derived from segmented volumes. Well-studied respiratory motion of tumors and other structures of interests will provide the 4D-RT treatment with valuable prior knowledge to achieve better monitoring and handling of respiratory motion through either respiratory gating or tracking.

This thesis also presented a novel method to fuse the static 3D-CT volume and the 4D-MRI dataset of the same patient to generate simulated 4D-CT dataset. To the author's best knowledge, this is the first study that combines the temporal information from 4D-MRI and the spatial information from 3D-CT. The generated high-resolution 4D-CT enables detailed study of small structures within the lungs such as blood vessels and bronchus that are often not visible in MRI images while keeping the radiation exposed to patients to a minimum level, compared to the use of 4D-CT. Additionally, the simulated 4D-CT generated addresses the problem with 4D-MRI based RT planning, which is the lack of electron density of MRI images to perform direct dose calculation. With the simulated dataset, it is possible to calculate dose by using the information contained in the 3D-CT. Together with the segmented target structures, a 4D treatment plan including adaptive dose calculation and beam position optimization becomes possible.

Overall, the novel 4D-MRI based system proposed in this thesis can add benefits to different steps of the workflow of 4D-RT. Simulated high-resolution simulated 4D-CT dataset representing multiple 'real-time' breathing cycles can be generated. Automatic, efficient, and accurate multiple-targets delineation is achieved. Patient specific 4D-RT treatment planning can be generated through quantified 4D information of tumor and other organs at risk.

6.4 Future work

The motivation of this thesis comes from the field of RT of lung cancer patients. Further research in this area is necessary to achieve a fully integrated 4D-MRI based RT.

1) Development of a fully automatic segmentation method for tumor and organs at risk segmentation using 4D-MRI

The registration-based segmentation scheme developed in this thesis is fully automatic after the initial segmentation of the reference volume. However, the initial template of the reference volume is segmented semi-automatically, human intervention is still involved. One potential future work is to construct a statistical model based on the geometry of all the lung cancer patients. With the help of the spatio-temporal based registration-based segmentation scheme, the process of constructing statistical model of huge patient database becomes less tedious. The population-based statistical model can be further used to improve the proposed scheme by automate the segmentation of the reference volume.

2) Improving the temporal and spatial resolution of 4D-MRI using super-resolution techniques

Ideally, a 4D image dataset should have both high temporal and spatial resolution. However, a limitation of the current 4D-MRI is that, the high

temporal resolution required to correctly characterize the dynamics of the motion is reached at the expense of a poor spatial resolution, often resulting in highly elongated voxels. Consequently, a potential future work could be to use super-resolution techniques [31] to improve the spatial resolution of 4D-MRI images. One possible method is to acquire three 4D-MRI datasets of the same patient in orthogonal planes (i.e. axial, coronal, and sagittal) that have the same high temporal resolution, high in-plane resolution, but large slice thickness. After the image acquisition, the three orthogonal 4D anisotropic datasets are combined into a super-resolution framework to reconstruct a series of isotropic volumes with the spatial resolution equals to the in-plane resolution of the three orthogonal images. As a result, the reconstructed 4D-MRI dataset would have both high temporal and spatial resolution.

3) Development of patient specific 4D model for tumor tracking during treatment delivery

The 4D-MRI based system presented in this thesis is able to present a detailed therapy plan for 4D-RT, including segmented 3D structures of tumor and organs at risk over time, size, volume, and motion information of tumor, and the necessary dose to apply. However, how to effectively and adaptively deliver dose to the tumor in motion during treatment delivery remains a challenge. To further improve current 4D-RT, the dose delivery should be adaptively adjusted according to the variations of locations and shapes of tumor and organs at risk in real-time during treatment delivery. Based on the findings and methods developed in this thesis, one potential future work is to construct a 4D model for each patient using 4D-MRI that contains continuous shifting and

deformation of tumor and other organs over time. This 4D model could be constructed by using FEM modeling of several breathing cycles and considering all the possible locations and shapes of organs and tumors [205]. The 4D model could be related to some simple respiratory signals such as signals from respiratory belt or image similarity matrices that can be used to compare with on-board images. Such relationship could enable fast tumor tracking during treatment delivery in real-time.

Although this thesis is based on the RT of lung cancer, the methods proposed in this thesis, such as the spatio-temporal based registration-based segmentation scheme and the fusion of CT and 4D-MRI, are not limited to the lungs. The methods can potentially be extended for various other applications that involve organs with periodic motion such as liver and heart.

6.5 Thesis conclusion

In this thesis, a novel 4D-MRI based system for 4D-RT planning of lung cancer patients was presented. This system explored the use of 4D-MRI in different stages of 4D-RT as a radiation-free alternative option of the current standard image modality in RT: CT. 4D-MRI sequences were evaluated in this thesis to find suitable sequences for lung cancer imaging using an advanced high-field 3T scanner that has been available for clinical use recently. TWIST sequence has been selected as it showed good image quality at a faster temporal resolution, which is capable of showing the motion path of tumor. To address

the challenge of segmentation of 4D-MRI, a novel registration-based segmentation scheme that incorporates spatio-temporal information about diaphragm movement to efficiently segment multiple structures of thoracic 4D-MRI dataset has been successfully developed. The segmentation scheme developed reduced computation amounts by up to 95% while maintaining good accuracy. To address the problem of dose calculated due to the use of 4D-MRI, a novel method to fuse 4D-MRI and 3D-CT to generate simulated 4D-CT was developed. This method combines deformable image registration and FEM to extract temporal information from 4D-MRI and transfer it onto 3D-CT to generate simulated 4D-CT. Accurate results were achieved in terms of landmark positions. The simulated 4D-CT has high spatial resolution, represents respiratory motion of multiple breathing cycles, and can be used to calculate dose. Overall, the use 4D-MRI has great potential to being an alternative to 4D-CT, providing an alternative imaging modality for RT of lung cancer patients.

Bibliography

- [1] S. H. Ferlay J, Bray F, Forman D, Mathers C and Parkin DM., "GLOBOCAN 2008, Cancer Incidence and Mortality Worldwide: IARC CancerBase No. 10 " *Lyon, France: International Agency for Research on Cancer*;; 2010.
- [2] L. G. Collins, C. Haines, R. Perkel, and R. E. Enck, "Lung cancer: diagnosis and management," *Am Fam Physician*, vol. 75, pp. 56-63, 2007.
- [3] Intensity Modulated Radiation Therapy Working Group, "Intensity-modulated radiotherapy: current status and issues of interest," *International Journal of Radiation Oncology* Biology* Physics*, vol. 51, pp. 880-914, 2001.
- [4] T. Nyholm, "Verification of dose calculations in radiotherapy," Umeå University, 2008.
- [5] E. Eisenhauer, P. Therasse, J. Bogaerts, L. Schwartz, D. Sargent, R. Ford, J. Dancey, S. Arbuck, S. Gwyther, and M. Mooney, "New response evaluation criteria in solid tumours: revised RECIST guideline (version 1.1)," *European journal of cancer*, vol. 45, pp. 228-247, 2009.
- [6] M. K. Bucci, A. Bevan, and M. Roach, 3rd, "Advances in radiation therapy: conventional to 3D, to IMRT, to 4D, and beyond," *CA Cancer J Clin*, vol. 55, pp. 117-34, Mar-Apr 2005.
- [7] F. C. Su, C. Shi, P. Mavroidis, V. Goytia, R. Crownover, P. Rassiah-Szegedi, and N. Papanikolaou, "Assessing four-dimensional radiotherapy planning and respiratory motion-induced dose difference based on biologically effective uniform dose," *Technol Cancer Res Treat*, vol. 8, pp. 187-200, Jun 2009.
- [8] Y. Seppenwoolde, H. Shirato, K. Kitamura, S. Shimizu, M. van Herk, J. V. Lebesque, and K. Miyasaka, "Precise and real-time measurement of 3D tumor motion in lung due to breathing and heartbeat, measured during radiotherapy," *International Journal of Radiation Oncology* Biology* Physics*, vol. 53, pp. 822-834, 2002.
- [9] J. M. Balter, K. L. Lam, C. J. McGinn, T. S. Lawrence, and R. K. Ten Haken, "Improvement of CT-based treatment-planning models of abdominal targets using static exhale imaging," *International Journal of Radiation Oncology* Biology* Physics*, vol. 41, pp. 939-943, 1998.
- [10] E. Rietzel, G. T. Chen, N. C. Choi, and C. G. Willet, "Four-dimensional image-based treatment planning: Target volume segmentation and dose calculation in the presence of respiratory motion," *International Journal of Radiation Oncology* Biology* Physics*, vol. 61, pp. 1535-1550, 2005.
- [11] C. W. Stevens, R. F. Munden, K. M. Forster, J. F. Kelly, Z. Liao, G. Starkschall, S. Tucker, and R. Komaki, "Respiratory-driven lung tumor motion is independent of tumor size, tumor location, and

- pulmonary function," *International Journal of Radiation Oncology* Biology* Physics*, vol. 51, pp. 62-68, 2001.
- [12] S. L. Kwa, J. V. Lebesque, J. Theuws, L. B. Marks, M. T. Munley, G. Bentel, D. Oetzel, U. Spahn, M. V. Graham, and R. E. Drzymala, "Radiation pneumonitis as a function of mean lung dose: an analysis of pooled data of 540 patients," *International Journal of Radiation Oncology* Biology* Physics*, vol. 42, pp. 1-9, 1998.
- [13] L. Lin, C. Shi, Y. Liu, G. Swanson, and N. Papanikolaou, "Development of a novel post-processing treatment planning platform for 4D radiotherapy," *Technol Cancer Res Treat*, vol. 7, pp. 125-32, Apr 2008.
- [14] L. Ekberg, O. Holmberg, L. Wittgren, G. Bjelkengren, and T. Landberg, "What margins should be added to the clinical target volume in radiotherapy treatment planning for lung cancer?," *Radiotherapy and Oncology*, vol. 48, pp. 71-77, Jul 1998.
- [15] T. G. Purdie, D. J. Moseley, J. P. Bissonnette, M. B. Sharpe, K. Franks, A. Bezjak, and D. A. Jaffray, "Respiration correlated cone-beam computed tomography and 4DCT for evaluating target motion in Stereotactic Lung Radiation Therapy," *Acta Oncologica*, vol. 45, pp. 915-922, Sep 2006.
- [16] D. Verellen, M. D. Ridder, N. Linthout, K. Tournel, G. Soete, and G. Storme, "Innovations in image-guided radiotherapy," *Nat Rev Cancer*, vol. 7, pp. 949-960, 2007.
- [17] M. K. Martel, R. K. Ten Haken, M. B. Hazuka, M. L. Kessler, M. Strawderman, A. T. Turrisi, T. S. Lawrence, B. A. Fraass, and A. S. Lichter, "Estimation of tumor control probability model parameters from 3-D dose distributions of non-small cell lung cancer patients," *Lung cancer*, vol. 24, pp. 31-37, 1999.
- [18] P. Okunieff, D. Morgan, A. Niemierko, and H. D. Suit, "Radiation dose-response of human tumors," *International Journal of Radiation Oncology* Biology* Physics*, vol. 32, pp. 1227-1237, 1995.
- [19] N. C. Choi and J. A. Doucette, "Improved survival of patients with unresectable non - small - cell bronchogenic carcinoma by an innovated high - dose En - Bloc radiotherapeutic approach," *Cancer*, vol. 48, pp. 101-109, 1981.
- [20] C. Plathow, M. Schoebinger, C. Fink, H. Hof, J. Debus, H.-P. Meinzer, and H.-U. Kauczor, "Quantification of Lung Tumor Volume and Rotation at 3D Dynamic Parallel MR Imaging with View Sharing: Preliminary Results1," *Radiology*, vol. 240, pp. 537-545, 2006.
- [21] J. Wu, P. Lei, R. Shekhar, H. Li, M. Suntharalingam, and W. D. D'Souza, "Do tumors in the lung deform during normal respiration? An image registration investigation," *International Journal of Radiation Oncology* Biology* Physics*, vol. 75, pp. 268-275, 2009.
- [22] P. J. Keall, G. T. Y. Chen, S. Joshi, T. R. Mackie, and C. W. Stevens, "Time-The fourth dimension in radiotherapy (ASTRO Panel Discussion)," *International Journal of Radiation Oncology • Biology • Physics*, vol. 57, pp. S8-9, 2003.
- [23] V. R. Kini, S. S. Vedam, P. J. Keall, S. Patil, C. Chen, and R. Mohan, "Patient training in respiratory-gated radiotherapy," *Medical Dosimetry*, vol. 28, pp. 7-11, 2003.
- [24] C. J. Haasbeek, B. J. Slotman, and S. Senan, "Radiotherapy for lung cancer: clinical impact of recent technical advances," *Lung Cancer*, vol. 64, pp. 1-8, 2009.

- [25] G. C. Sharp, S. B. Jiang, S. Shimizu, and H. Shirato, "Prediction of respiratory tumour motion for real-time image-guided radiotherapy," *Physics in Medicine and Biology*, vol. 49, p. 425, 2004.
- [26] S. A. Leibel, Z. Fuks, M. J. Zelefsky, S. L. Wolden, K. E. Rosenzweig, K. M. Alektiar, M. A. Hunt, E. D. Yorke, L. X. Hong, and H. I. Amols, "Intensity-modulated radiotherapy," *The Cancer Journal*, vol. 8, pp. 164-176, 2002.
- [27] J. Lehmann, J. R. Adler, and J. Hai, "CyberKnife radiotherapy for localized prostate cancer: rationale and technical feasibility," *Technology in cancer research & treatment*, vol. 2, 2003.
- [28] J. M. Sanches, J. C. Nascimento, and J. S. Marques, "Medical image noise reduction using the Sylvester–Lyapunov equation," *Image Processing, IEEE Transactions on*, vol. 17, pp. 1522-1539, 2008.
- [29] P. Bao and L. Zhang, "Noise reduction for magnetic resonance images via adaptive multiscale products thresholding," *Medical Imaging, IEEE Transactions on*, vol. 22, pp. 1089-1099, 2003.
- [30] H. Greenspan, "Super-resolution in medical imaging," *The Computer Journal*, vol. 52, pp. 43-63, 2009.
- [31] E. Van Reeth, I. W. Tham, C. H. Tan, and C. L. Poh, "Super - resolution in magnetic resonance imaging: A review," *Concepts in Magnetic Resonance Part A*, vol. 40, pp. 306-325, 2012.
- [32] Y.-T. Kim, "Contrast enhancement using brightness preserving bi-histogram equalization," *Consumer Electronics, IEEE Transactions on*, vol. 43, pp. 1-8, 1997.
- [33] T.-L. Ji, M. Sundareshan, and H. Roehrig, "Adaptive image contrast enhancement based on human visual properties," *Medical Imaging, IEEE Transactions on*, vol. 13, pp. 573-586, 1994.
- [34] J. Lu, D. M. Healy Jr, and J. B. Weaver, "Contrast enhancement of medical images using multiscale edge representation," *Optical engineering*, vol. 33, pp. 2151-2161, 1994.
- [35] R. M. Haralick and L. G. Shapiro, "Image segmentation techniques," *Computer vision, graphics, and image processing*, vol. 29, pp. 100-132, 1985.
- [36] D. L. Pham, C. Xu, and J. L. Prince, "Current methods in medical image segmentation," *Annual review of biomedical engineering*, vol. 2, pp. 315-337, 2000.
- [37] Q. Duan, E. D. Angelini, and A. F. Laine, "Real-time segmentation by active geometric functions," *Computer methods and programs in biomedicine*, vol. 98, pp. 223-230, 2010.
- [38] J. Montagnat and H. Delingette, "4D deformable models with temporal constraints: application to 4D cardiac image segmentation," *Medical Image Analysis*, vol. 9, pp. 87-100, 2// 2005.
- [39] J. Peters, O. Ecabert, C. Meyer, H. Schramm, R. Kneser, A. Groth, and J. Weese, "Automatic whole heart segmentation in static magnetic resonance image volumes," in *Medical Image Computing and Computer-Assisted Intervention–MICCAI 2007*, ed: Springer, 2007, pp. 402-410.
- [40] L. G. Brown, "A survey of image registration techniques," *ACM computing surveys (CSUR)*, vol. 24, pp. 325-376, 1992.
- [41] D. W. Townsend and S. R. Cherry, "Combining anatomy and function: the path to true image fusion," *European radiology*, vol. 11, pp. 1968-1974, 2001.
- [42] K. Kagawa, W. R. Lee, T. E. Schultheiss, M. A. Hunt, A. H. Shaer, and G. E. Hanks, "Initial clinical assessment of CT-MRI image fusion software in localization of the prostate for 3D conformal

- radiation therapy," *International Journal of Radiation Oncology* Biology* Physics*, vol. 38, pp. 319-325, 1997.
- [43] C. A. Pelizzari, G. T. Chen, D. R. Spelbring, R. R. Weichselbaum, and C.-T. Chen, "Accurate three-dimensional registration of CT, PET, and/or MR images of the brain," *Journal of computer assisted tomography*, vol. 13, pp. 20-26, 1989.
 - [44] U. Pietrzyk, K. Herholz, and W. Heiss, "Three-dimensional alignment of functional and morphological tomograms," *Journal of computer assisted tomography*, vol. 14, pp. 51-59, 1989.
 - [45] F. J. Lagerwaard, M. R. J. Nijssen-Visser, W. J. Graveland, and S. Senan, "Tumor location cannot predict the mobility of lung tumors: a 3D analysis of data generated from multiple CT scans," *International Journal of Radiation Oncology* Biology* Physics*, vol. 56, pp. 348-354, 2003.
 - [46] J. Dinkel, C. Hintze, R. Tetzlaff, P. E. Huber, K. Herfarth, J. Debus, H. U. Kauczor, and C. Thieke, "4D-MRI analysis of lung tumor motion in patients with hemidiaphragmatic paralysis," *Radiotherapy and Oncology*, vol. 91, pp. 449-454, 2009.
 - [47] H. Kauczor and E. Beek, "MRI of the Chest," ed, 2006, pp. 447-467.
 - [48] D. J. Brenner and E. J. Hall, "Computed tomography—an increasing source of radiation exposure," *New England Journal of Medicine*, vol. 357, pp. 2277-2284, 2007.
 - [49] J. Biederer, C. Hintze, M. Fabel, and J. Dinkel, "Magnetic resonance imaging and computed tomography of respiratory mechanics," *Journal of Magnetic Resonance Imaging*, vol. 32, pp. 1388-1397, 2010.
 - [50] E. J. van Beek, J. M. Wild, H. U. Kauczor, W. Schreiber, J. P. Mugler, and E. E. de Lange, "Functional MRI of the lung using hyperpolarized 3 - helium gas," *Journal of Magnetic Resonance Imaging*, vol. 20, pp. 540-554, 2004.
 - [51] H. E. Möller, X. J. Chen, B. Saam, K. D. Hagspiel, G. A. Johnson, T. A. Altes, E. E. de Lange, and H. U. Kauczor, "MRI of the lungs using hyperpolarized noble gases," *Magnetic Resonance in Medicine*, vol. 47, pp. 1029-1051, 2002.
 - [52] M. von Siebenthal, G. Szekely, U. Gamper, P. Boesiger, A. Lomax, and P. Cattin, "4D MR imaging of respiratory organ motion and its variability," *Phys Med Biol*, vol. 52, pp. 1547-64, Mar 21 2007.
 - [53] B. Raaymakers, J. Lagendijk, J. Overweg, J. Kok, A. Raaijmakers, E. Kerkhof, R. van der Put, I. Meijsing, S. Crijns, and F. Benedosso, "Integrating a 1.5 T MRI scanner with a 6 MV accelerator: proof of concept," *Physics in medicine and biology*, vol. 54, p. N229, 2009.
 - [54] G. Li, D. Citrin, K. Camphausen, B. Mueller, C. Burman, B. Mychalczak, R. W. Miller, and Y. Song, "Advances in 4D medical imaging and 4D radiation therapy," *Technology in cancer research & treatment*, vol. 7, p. 67, 2008.
 - [55] K. L. Moore, A. F. Dalley, and A. M. Agur, *Clinically oriented anatomy*: Wolters Kluwer Health, 2013.
 - [56] G. J. Tortora and B. Derrickson, *Principles of Anatomy and Physiology [With A Brief Atlas of the Skeleton, Surface Anatomy,]*: John Wiley & Sons, 2008.
 - [57] S. Davies, A. Hill, R. Holmes, M. Halliwell, and P. Jackson, "Ultrasound quantitation of respiratory organ motion in the upper abdomen," *British journal of radiology*, vol. 67, p. 1096, 1994.

- [58] B. Gagel, C. Demirel, A. Kientopf, M. Pinkawa, M. Piroth, S. Stanzel, C. Breuer, B. Asadpour, T. Jansen, and R. Holy, "Active breathing control (ABC): Determination and reduction of breathing-induced organ motion in the chest," *International Journal of Radiation Oncology* Biology* Physics*, vol. 67, pp. 742-749, 2007.
- [59] A. E. Lujan, E. W. Larsen, J. M. Balter, and R. K. Ten Haken, "A method for incorporating organ motion due to breathing into 3D dose calculations," *Medical physics*, vol. 26, p. 715, 1999.
- [60] LalyofHats, "Respiratory system complete en," Wikimedia Commons, 2007.
- [61] RobinH, "Gcsebiobreath2," Wikibooks, 2006.
- [62] E. T. Fontham, P. Correa, P. Reynolds, A. Wu-Williams, P. A. Buffler, R. S. Greenberg, V. W. Chen, T. Alterman, P. Boyd, and D. F. Austin, "Environmental tobacco smoke and lung cancer in nonsmoking women," *Jama*, vol. 271, pp. 1752-1759, 1994.
- [63] M. J. Thun, L. M. Hannan, L. L. Adams-Campbell, P. Boffetta, J. E. Buring, D. Feskanich, W. D. Flanders, S. H. Jee, K. Katanoda, and L. N. Kolonel, "Lung cancer occurrence in never-smokers: an analysis of 13 cohorts and 22 cancer registry studies," *PLoS medicine*, vol. 5, p. e185, 2008.
- [64] V. Kumar, A. K. Abbas, and J. C. Aster, *Robbins basic pathology*: Elsevier Health Sciences, 2012.
- [65] N. Girard and F. Mornex, "Stereotactic radiotherapy for non-small cell lung cancer: From concept to clinical reality. 2011 update," *Cancer radiotherapie: journal de la Societe francaise de radiotherapie oncologique*, vol. 15, pp. 522-526, 2011.
- [66] J. L. Prince and J. M. Links, *Medical imaging signals and systems*: Pearson Prentice Hall Upper Saddle River, NJ, 2006.
- [67] S. R. Deans, *The Radon transform and some of its applications*: DoverPublications. com, 2007.
- [68] E. Rietzel, T. Pan, and G. T. Chen, "Four-dimensional computed tomography: image formation and clinical protocol," *Medical physics*, vol. 32, p. 874, 2005.
- [69] U. Langner and P. Keall, "Prospective displacement and velocity-based cine 4D CT," *Medical physics*, vol. 35, p. 4501, 2008.
- [70] S. Shen, J. Duan, J. B. Fiveash, I. A. Brezovich, B. A. Plant, S. A. Spencer, R. A. Popple, P. N. Pareek, and J. A. Bonner, "Validation of target volume and position in respiratory gated CT planning and treatment," *Medical physics*, vol. 30, p. 3196, 2003.
- [71] P. Keall, G. Starkschall, H. e. e. Shukla, K. Forster, V. Ortiz, C. Stevens, S. Vedam, R. George, T. Guerrero, and R. Mohan, "Acquiring 4D thoracic CT scans using a multislice helical method," *Physics in medicine and biology*, vol. 49, p. 2053, 2004.
- [72] E. D. Brandner, A. Wu, H. Chen, D. Heron, S. Kalnicki, K. Komanduri, K. Gerszten, S. Burton, I. Ahmed, and Z. Shou, "Abdominal organ motion measured using 4D CT," *International Journal of Radiation Oncology* Biology* Physics*, vol. 65, pp. 554-560, 2006.
- [73] L. Dietrich, S. Jetter, T. Tucking, S. Nill, and U. Oelfke, "Linac-integrated 4D cone beam CT: first experimental results," *Physics in Medicine and Biology*, vol. 51, pp. 2939-2952, Jun 7 2006.
- [74] K. Taguchi, "Temporal resolution and the evaluation of candidate algorithms for four-dimensional CT," *Medical Physics*, vol. 30, pp. 640-650, Apr 2003.
- [75] J. Sonke, P. Remeijer, and M. van Herk, "Respiration-correlated cone-beam CT: Obtaining a four-dimensional data set (WIP)," *Medical Physics*, vol. 30, pp. 1415-1415, Jun 2003.

- [76] U. Schneider, E. Pedroni, and A. Lomax, "The calibration of CT Hounsfield units for radiotherapy treatment planning," *Physics in medicine and biology*, vol. 41, p. 111, 1996.
- [77] T. Knöös, M. Nilsson, and L. Ahlgren, "A method for conversion of Hounsfield number to electron density and prediction of macroscopic pair production cross-sections," *Radiotherapy and Oncology*, vol. 5, pp. 337-345, 1986.
- [78] J. Hornak. (1996). *The Basics of MRI*.
- [79] S. M. Rocklage, J. Kucharczyk, and M. E. Moseley, "Magnetic resonance imaging," ed: Google Patents, 1998.
- [80] T. C. Farrar and E. D. Becker, *Pulse and Fourier transform NMR: introduction to theory and methods*: Access Online via Elsevier, 1971.
- [81] A. Webb and G. C. Kagadis, "Introduction to biomedical imaging," *Medical Physics*, vol. 30, p. 2267, 2003.
- [82] J. Carlson and T. Minemura, "Imaging time reduction through multiple receiver coil data acquisition and image reconstruction," *Magnetic Resonance in Medicine*, vol. 29, pp. 681-687, 1993.
- [83] J. Bogaert, S. Dymarkowski, and A. M. Taylor, *Clinical cardiac MRI: with interactive CD-ROM*: Springer Verlag, 2005.
- [84] M. Fabel, B. J. Wintersperger, O. Dietrich, M. Eichinger, C. Fink, M. Puderbach, H. U. Kauczor, S. O. Schoenberg, and J. Biederer, "MRI of respiratory dynamics with 2D steady-state free-precession and 2D gradient echo sequences at 1.5 and 3 Tesla: an observer preference study," *European radiology*, vol. 19, pp. 391-9, Feb 2009.
- [85] M. Lustig, D. L. Donoho, J. M. Santos, and J. M. Pauly, "Compressed sensing MRI," *Signal Processing Magazine, IEEE*, vol. 25, pp. 72-82, 2008.
- [86] J. Biederer, J. Dinkel, G. Remmert, S. Jetter, S. Nill, T. Moser, R. Bendl, C. Thierfelder, M. Fabel, and U. Oelfke, "4D-Imaging of the Lung: Reproducibility of Lesion Size and Displacement on Helical CT, MRI, and Cone Beam CT in a Ventilated Ex Vivo System," *International Journal of Radiation Oncology* Biology* Physics*, vol. 73, pp. 919-926, 2009.
- [87] J. Dinkel, C. Hintze, R. Tetzlaff, P. E. Huber, K. Herfarth, J. Debus, H. U. Kauczor, and C. Thieke, "4D-MRI analysis of lung tumor motion in patients with hemidiaphragmatic paralysis," *Radiother Oncol*, vol. 91, pp. 449-54, Jun 2009.
- [88] C. Plathow, M. Schoebinger, F. Herth, S. Tuengerthal, H.-P. Meinzer, and H.-U. Kauczor, "Estimation of pulmonary motion in healthy subjects and patients with intrathoracic tumors using 3D-dynamic MRI: initial results," *Korean Journal of Radiology*, vol. 10, pp. 559-567, 2009.
- [89] G. Remmert, J. Biederer, F. Lohberger, M. Fabel, and G. H. Hartmann, "Four-dimensional magnetic resonance imaging for the determination of tumour movement and its evaluation using a dynamic porcine lung phantom," *Physics in Medicine and Biology*, vol. 52, pp. N401-N415, Sep 21 2007.
- [90] G. F. Gibbs, J. Huston, M. A. Bernstein, S. J. Riederer, and R. D. Brown, "Improved image quality of intracranial aneurysms: 3.0-T versus 1.5-T time-of-flight MR angiography," *American journal of neuroradiology*, vol. 25, pp. 84-87, 2004.
- [91] L. N. Tanenbaum, "Clinical 3T MR imaging: mastering the challenges," *Magnetic resonance imaging clinics of North America*, vol. 14, p. 1, 2006.

- [92] C. A. Yi, T. Y. Jeon, K. S. Lee, J. H. Lee, J. B. Seo, Y. K. Kim, and M. J. Chung, "3-T MRI: usefulness for evaluating primary lung cancer and small nodules in lobes not containing primary tumors," *American Journal of Roentgenology*, vol. 189, pp. 386-392, 2007.
- [93] H. Y. Kim, A. Y. Chin, K. S. Lee, M. J. Chung, Y. K. Kim, B. K. Choi, H. Kim, and O. J. Kwon, "Nodal Metastasis in Non-Small Cell Lung Cancer: Accuracy of 3.0-T MR Imaging1," *Radiology*, vol. 246, pp. 596-604, 2008.
- [94] R. C. Gonzalez and R. E. Woods, "Digital image processing," *Addison-Wesley Publishing Company*, vol. 503, pp. 0-201.
- [95] J. Rogowska, "Overview and fundamentals of medical image segmentation," *Handbook of Medical Imaging, Processing and Analysis*, pp. 69-85, 2000.
- [96] D. L. Pham, C. Xu, and J. L. Prince, "CURRENT METHODS IN MEDICAL IMAGE SEGMENTATION," *Biomedical Engineering*, vol. 2, p. 315, 2000.
- [97] T. Heimann and H. Delingette, "Model-Based Segmentation," in *Biomedical Image Processing*, T. M. Deserno, Ed., ed: Springer Berlin Heidelberg, 2011, pp. 279-303.
- [98] M. Kass, A. Witkin, and D. Terzopoulos, "Snakes: Active contour models," *International journal of computer vision*, vol. 1, pp. 321-331, 1988.
- [99] F. Zhao, H. Zhang, A. Wahle, T. D. Scholz, and M. Sonka, "Automated 4D segmentation of aortic magnetic resonance images," in *British Machine Vision Conference (BMVA)*, 2006, pp. 247-256.
- [100] K. D. Fritscher, R. Pilgram, and R. Schubert, "Automatic cardiac 4D segmentation using level sets," in *Functional Imaging and Modeling of the Heart*, ed: Springer, 2005, pp. 113-122.
- [101] S. P. O'Brien, O. Ghita, and P. F. Whelan, "A Novel Model-Based 3D+Time Left Ventricular Segmentation Technique," *Medical Imaging, IEEE Transactions on*, vol. 30, pp. 461-474, 2011.
- [102] B.-J. Leiner, J. Olveres, B. Escalante-Ramírez, F. Arámbula, and E. Vallejo, "Segmentation of 4D cardiac computer tomography images using active shape models," in *Proc. SPIE 8436, Optics, Photonics, and Digital Technologies for Multimedia Applications II*, 2012.
- [103] H. Lombaert, Y. Sun, and F. Cheriet, "Fast 4D segmentation of large datasets using graph cuts," in *Proc. SPIE 7962, Medical Imaging 2011: Image Processing*, 2011.
- [104] J. Cousty, L. Najman, M. Couprie, S. Clément-Guinaudeau, T. Goissen, and J. Garot, "Segmentation of 4D cardiac MRI: Automated method based on spatio-temporal watershed cuts," *Image and Vision Computing*, vol. 28, pp. 1229-1243, 2010.
- [105] M. Lorenzo-Valdes, G. Sanchez-Ortiz, R. Mohiaddin, and D. Rueckert, "Atlas-based segmentation and tracking of 3D cardiac MR images using non-rigid registration," *Medical Image Computing and Computer-Assisted Intervention—MICCAI 2002*, pp. 642-650, 2002.
- [106] D. L. Collins and A. C. Evans, "Animal: validation and applications of nonlinear registration-based segmentation," *International Journal of Pattern Recognition and Artificial Intelligence*, vol. 11, pp. 1271-1294, 1997.
- [107] B. Fischl, D. H. Salat, E. Busa, M. Albert, M. Dieterich, C. Haselgrove, A. van der Kouwe, R. Killiany, D. Kennedy, and S. Klaveness, "Whole brain segmentation: automated labeling of neuroanatomical structures in the human brain," *Neuron*, vol. 33, pp. 341-355, 2002.

- [108] N. C. Andreasen, R. Rajarethinam, T. Cizadlo, S. Arndt, V. W. Swayze, L. A. Flashman, D. S. O'Leary, J. C. Ehrhardt, and W. T. Yuh, "Automatic atlas-based volume estimation of human brain regions from MR images," *Journal of computer assisted tomography*, vol. 20, pp. 98-106, 1996.
- [109] W. G. Lu, G. H. Olivera, Q. Chen, M. L. Chen, and K. J. Ruchala, "Automatic re-contouring in 4D radiotherapy," *Physics in Medicine and Biology*, vol. 51, pp. 1077-1099, Mar 7 2006.
- [110] X. Zhuang, C. Yao, Y. L. Ma, D. Hawkes, G. Penney, and S. Ourselin, "Registration-based propagation for whole heart segmentation from compounded 3D echocardiography," in *Biomedical Imaging: From Nano to Macro, 2010 IEEE International Symposium on*, 2010, pp. 1093-1096.
- [111] M. R. Kaus, T. Netsch, S. Kabus, V. Pekar, T. McNutt, and B. Fischer, "Estimation of organ motion from 4D CT for 4D radiation therapy planning of lung cancer," *Medical Image Computing and Computer-Assisted Intervention-MICCAI 2004*, pp. 1017-1024, 2004.
- [112] I. E. van Dam, J. R. van Sörnsen de Koste, G. G. Hanna, R. Muirhead, B. J. Slotman, and S. Senan, "Improving target delineation on 4-dimensional CT scans in stage I NSCLC using a deformable registration tool," *Radiotherapy and Oncology*, vol. 96, pp. 67-72, 2010.
- [113] M. Peroni, M. Spadea, M. Riboldi, G. Baroni, G. Chen, and G. Sharp, "Validation of an automatic contour propagation method for lung cancer 4D adaptive radiation therapy," 2009, pp. 1071-1074.
- [114] W. Lu, G. H. Olivera, Q. Chen, M. L. Chen, and K. J. Ruchala, "Automatic re-contouring in 4D radiotherapy," *Physics in Medicine and Biology*, vol. 51, p. 1077, 2006.
- [115] J. Ehrhardt, R. Werner, T. Frenzel, W. Lu, D. Low, and H. Handels, "Analysis of free breathing motion using artifact reduced 4D CT image data," in *Medical Imaging*, 2007, pp. 65121N-65121N-11.
- [116] R. Werner, J. Ehrhardt, A. Schmidt-Richberg, A. Heiß, and H. Handels, "Estimation of motion fields by non-linear registration for local lung motion analysis in 4D CT image data," *International Journal of Computer Assisted Radiology and Surgery*, pp. 1-11.
- [117] A. Schmidt-Richberg, J. Ehrhardt, R. Werner, and H. Handels, "Evaluation and Comparison of Force Terms for the Estimation of Lung Motion by Non-linear Registration of 4D-CT Image Data," 2009, pp. 2128-2131.
- [118] S. Kabus, T. Klinder, K. Murphy, B. van Ginneken, C. Lorenz, and J. Pluim, "Evaluation of 4D-CT lung registration," *Medical Image Computing and Computer-Assisted Intervention-MICCAI 2009*, pp. 747-754, 2009.
- [119] R. Speight, J. Sykes, R. Lindsay, K. Franks, and D. Thwaites, "The evaluation of a deformable image registration segmentation technique for semi-automating internal target volume (ITV) production from 4DCT images of lung stereotactic body radiotherapy (SBRT) patients," *Radiotherapy and Oncology*, vol. 98, pp. 277-283, 2011.
- [120] H. P. Xuejun Gu, Yun Liang, Richard Castillo, Deshan Yang, Dongju Choi, Edward Castillo, Amitava Majumdar, Thomas Guerrero, Steve B Jiang, "Implementation and evaluation of various demons deformable image registration algorithms on a GPU," *Physics in Medicine and Biology*, pp. 207-219, 2010.
- [121] D. Rueckert, M. Lorenzo-Valdes, R. Chandrashekara, G. Sanchez-Ortiz, and R. Mohiaddin, "Non-rigid registration of cardiac MR: Application to motion modelling and atlas-based

- segmentation," in *Biomedical Imaging, 2002. Proceedings. 2002 IEEE International Symposium on*, 2002, pp. 481-484.
- [122] M.-P. Jolly, C. Guetter, X. Lu, H. Xue, and J. Guehring, "Automatic segmentation of the myocardium in cine MR images using deformable registration," in *Statistical Atlases and Computational Models of the Heart. Imaging and Modelling Challenges*, ed: Springer, 2012, pp. 98-108.
- [123] J. Dey, T. Pan, D. J. Choi, D. Robotis, M. S. Smyczynski, P. Hendrik Pretorius, and M. A. King, "Estimation of cardiac respiratory-motion by semi-automatic segmentation and registration of non-contrast-enhanced 4D-CT cardiac datasets," *Nuclear Science, IEEE Transactions on*, vol. 56, pp. 3662-3671, 2009.
- [124] K. Cai, X. Liang, R. Yang, and S. Ou, "Automatic Whole Heart Segmentation of 4D Dual Source Cardiac CT Based on the Deformation Field," *International Journal of Digital Content Technology and its Applications*, vol. 6, pp. 361-369, 2012.
- [125] M. G. Linguraru and R. M. Summers, "Multi-organ automatic segmentation in 4D contrast-enhanced abdominal CT," in *Biomedical Imaging: From Nano to Macro, 2008. ISBI 2008. 5th IEEE International Symposium on*, 2008, pp. 45-48.
- [126] L. G. Brown, "A Survey of Image Registration Techniques," *Computing Surveys*, vol. 24, pp. 325-376, Dec 1992.
- [127] D. A. Keim, "Efficient geometry-based similarity search of 3D spatial databases," 1999, pp. 419-430.
- [128] W. M. Wells, P. Viola, H. Atsumi, S. Nakajima, and R. Kikinis, "Multi-modal volume registration by maximization of mutual information," *Medical image analysis*, vol. 1, pp. 35-51, 1996.
- [129] J. P. Pluim, J. A. Maintz, and M. A. Viergever, "Mutual-information-based registration of medical images: a survey," *Medical Imaging, IEEE Transactions on*, vol. 22, pp. 986-1004, 2003.
- [130] F. Maes, A. Collignon, D. Vandermeulen, G. Marchal, and P. Suetens, "Multimodality image registration by maximization of mutual information," *Medical Imaging, IEEE Transactions on*, vol. 16, pp. 187-198, 1997.
- [131] M. Mellor and M. Brady, "Phase mutual information as a similarity measure for registration," *Medical image analysis*, vol. 9, pp. 330-343, 2005.
- [132] P. Cachier and X. Pennec, "3D non-rigid registration by gradient descent on a gaussian-windowed similarity measure using convolutions," in *Mathematical Methods in Biomedical Image Analysis, 2000. Proceedings. IEEE Workshop on*, 2000, pp. 182-189.
- [133] M. A. Audette, F. P. Ferrie, and T. M. Peters, "An algorithmic overview of surface registration techniques for medical imaging," *Medical Image Analysis*, vol. 4, pp. 201-217, Sep 2000.
- [134] F. L. Bookstein, "Principal Warps - Thin-Plate Splines and the Decomposition of Deformations," *Ieee Transactions on Pattern Analysis and Machine Intelligence*, vol. 11, pp. 567-585, Jun 1989.
- [135] B. Pham, "Quadratic B-Splines for Automatic Curve and Surface Fitting," *Computers & Graphics*, vol. 13, pp. 471-475, 1989.
- [136] J. Modersitzki, *Numerical methods for image registration*: Oxford University Press, USA, 2004.
- [137] C. Broit, "Optimal registration of deformed images," 1981.

- [138] M. Bro-Nielsen and C. Gramkow, "Fast fluid registration of medical images," 1996, pp. 265-276.
- [139] J. P. Thirion, "Image matching as a diffusion process: an analogy with Maxwell's demons," *Medical Image Analysis*, vol. 2, pp. 243-260, 1998.
- [140] S. S. Beauchemin and J. L. Barron, "The computation of optical flow," *ACM Computing Surveys (CSUR)*, vol. 27, pp. 433-466, 1995.
- [141] H. Wang, L. Dong, J. O'Daniel, R. Mohan, A. S. Garden, K. K. Ang, D. A. Kuban, M. Bonnen, J. Y. Chang, and R. Cheung, "Validation of an accelerated 'demons' algorithm for deformable image registration in radiation therapy," *Physics in Medicine and Biology*, vol. 50, p. 2887, 2005.
- [142] P. Rogelj and S. Kovacic, "Symmetric image registration," *Medical Image Analysis*, vol. 10, pp. 484-493, 2006.
- [143] X. Pennec, P. Cachier, and N. Ayache, "Understanding the demon's algorithm: 3D non-rigid registration by gradient descent," 1999, pp. 597-605.
- [144] D. Yang, H. Li, D. A. Low, J. O. Deasy, and I. E. Naqa, "A fast inverse consistent deformable image registration method based on symmetric optical flow computation," *Physics in Medicine and Biology*, vol. 53, p. 6143, 2008.
- [145] B. Fischer and J. Modersitzki, "Curvature based image registration," *Journal of Mathematical Imaging and Vision*, vol. 18, pp. 81-85, 2003.
- [146] J. A. Nelder, *Practical mathematical optimization: an introduction to basic optimization theory and classical and new gradient-based algorithms* vol. 97: Springer Verlag, 2005.
- [147] M. von Siebenthal, G. Szekely, U. Gamper, P. Boesiger, A. Lomax, and P. Cattin, "4D MR imaging of respiratory organ motion and its variability," *Physics in Medicine and Biology*, vol. 52, pp. 1547-1564, Mar 21 2007.
- [148] C. Fink, M. Puderbach, J. Biederer, M. Fabel, O. Dietrich, H. U. Kauczor, M. F. Reiser, and S. O. Schönberg, "Lung MRI at 1.5 and 3 Tesla: observer preference study and lesion contrast using five different pulse sequences," *Investigative radiology*, vol. 42, pp. 377-383, 2007.
- [149] J. Biederer, C. Hintze, M. Fabel, and J. Dinkel, "Magnetic resonance imaging and computed tomography of respiratory mechanics," *J Magn Reson Imaging*, vol. 32, pp. 1388-97, Dec 2010.
- [150] J. J. Van Vaals, M. E. Brummer, W. Thomas Dixon, H. H. Tuithof, H. Engels, R. C. Nelson, B. M. Gerety, J. L. Chezmar, and J. A. Den Boer, "'Keyhole' method for accelerating imaging of contrast agent uptake," *Journal of Magnetic Resonance Imaging*, vol. 3, pp. 671-675, 1993.
- [151] G. Liney, *MRI from A to Z: a definitive guide for medical professionals*: Springer-Verlag London Limited, 2010.
- [152] Y. Ohno, H. Hatabu, D. Takenaka, T. Higashino, H. Watanabe, C. Ohbayashi, M. Yoshimura, M. Satouchi, Y. Nishimura, and K. Sugimura, "Metastases in Mediastinal and Hilar Lymph Nodes in Patients with Non-Small Cell Lung Cancer: Quantitative and Qualitative Assessment with STIR Turbo Spin-Echo MR Imaging," *Radiology*, vol. 231, pp. 872-879, 2004.
- [153] C. Plathow, S. Ley, C. Fink, M. Puderbach, M. Heilmann, I. Zuna, and H.-U. Kauczor, "Evaluation of chest motion and volumetry during the breathing cycle by dynamic MRI in healthy subjects: comparison with pulmonary function tests," *Investigative radiology*, vol. 39, pp. 202-209, 2004.

- [154] T. Schroeder, S. G. Ruehm, J. F. Debatin, M. E. Ladd, J. Barkhausen, and S. C. Goehde, "Detection of pulmonary nodules using a 2D HASTE MR sequence: comparison with MDCT," *American Journal of Roentgenology*, vol. 185, pp. 979-984, 2005.
- [155] C. A. Yi, K. M. Shin, K. S. Lee, B. T. Kim, H. Kim, O. J. Kwon, J. Y. Choi, and M. J. Chung, "Non-small cell lung cancer staging: efficacy comparison of integrated PET/CT versus 3.0-T whole-body MR imaging," *Radiology*, vol. 248, pp. 632-42, Aug 2008.
- [156] P. Landwehr, O. Schulte, and K. Lackner, "MR imaging of the chest: mediastinum and chest wall," *European radiology*, vol. 9, pp. 1737-44, 1999.
- [157] M. Suga, T. Matsuda, M. Komori, K. Minato, and T. Takahashi, "Keyhole method for high-speed human cardiac cine MR imaging," *Journal of Magnetic Resonance Imaging*, vol. 10, pp. 778-783, 1999.
- [158] J.-H. Gao, J. Xiong, S. Lai, E. M. Haacke, M. G. Woldorff, J. Li, and P. T. Fox, "Improving the temporal resolution of functional MR imaging using keyhole techniques," *Magnetic Resonance in Medicine*, vol. 35, pp. 854-860, 1996.
- [159] C. Plathow, M. Schoebinger, C. Fink, S. Ley, M. Puderbach, M. Eichinger, M. Bock, H.-P. Meinzer, and H.-U. Kauczor, "Evaluation of lung volumetry using dynamic three-dimensional magnetic resonance imaging," *Investigative radiology*, vol. 40, pp. 173-179, 2005.
- [160] A. K. Sato, N. A. Stevo, R. S. Tavares, M. S. G. Tsuzuki, E. Kadota, T. Gotoh, S. Kagei, and T. Iwasawa, "Registration of temporal sequences of coronal and sagittal MR images through respiratory patterns," *Biomedical Signal Processing and Control*, vol. 6, pp. 34-47, Jan 2011.
- [161] C. Plathow, M. Klopp, C. Fink, A. Sandner, H. Hof, M. Puderbach, F. Herth, A. Schmähl, and H. Kauczor, "Quantitative analysis of lung and tumour mobility: comparison of two time-resolved MRI sequences," *British journal of radiology*, vol. 78, pp. 836-840, 2005.
- [162] "PASW Statistics for Windows," Version 18.0 ed. Chicago: SPSS Inc., 2009.
- [163] D. Rueckert, L. I. Sonoda, C. Hayes, D. L. G. Hill, M. O. Leach, and D. J. Hawkes, "Nonrigid registration using free-form deformations: application to breast MR images," *Medical Imaging, IEEE Transactions on*, vol. 18, pp. 712-721, 1999.
- [164] T. S. Yoo, M. J. Ackerman, W. E. Lorensen, W. Schroeder, V. Chalana, S. Aylward, D. Metaxas, and R. Whitaker, "Engineering and algorithm design for an image processing api: a technical report on itk-the insight toolkit," *Studies in health technology and informatics*, pp. 586-592, 2002.
- [165] L. R. Dice, "Measures of the amount of ecologic association between species," *Ecology*, vol. 26, pp. 297-302, 1945.
- [166] W. E. Lorensen and H. E. Cline, "Marching cubes: A high resolution 3D surface construction algorithm," *ACM Siggraph Computer Graphics*, vol. 21, pp. 163-169, 1987.
- [167] W. Schroeder, K. Martin, K. W. Martin, and B. Lorensen, *The visualization toolkit*: Prentice Hall PTR, 1998.
- [168] A. H. Squillacote and J. Ahrens, *The paraview guide*: Kitware, 2006.
- [169] S. Nithiananthan, K. Brock, M. Daly, H. Chan, J. Irish, and J. Siewerdsen, "Demons deformable registration for CBCT-guided procedures in the head and neck: convergence and accuracy," *Medical Physics*, vol. 36, p. 4755, 2009.

- [170] X. Gu, H. Pan, Y. Liang, R. Castillo, D. Yang, D. Choi, E. Castillo, A. Majumdar, T. Guerrero, and S. B. Jiang, "Implementation and evaluation of various demons deformable image registration algorithms on a GPU," *Physics in medicine and biology*, vol. 55, p. 207, 2009.
- [171] G. Wahba, *Spline models for observational data* vol. 59: Society for Industrial Mathematics, 1990.
- [172] R. Benjemaa and F. Schmitt, "Fast global registration of 3D sampled surfaces using a multi-z-buffer technique," *Image and Vision Computing*, vol. 17, pp. 113-123, 1999.
- [173] P. A. Yushkevich, J. Piven, H. C. Hazlett, R. G. Smith, S. Ho, J. C. Gee, and G. Gerig, "User-guided 3D active contour segmentation of anatomical structures: significantly improved efficiency and reliability," *Neuroimage*, vol. 31, pp. 1116-1128, 2006.
- [174] W. J. Conover, "Practical nonparametric statistics," 1998.
- [175] "MATLAB," Version 7.11.1 ed. Natick, Massachusetts: The MathWorks Inc., 2010.
- [176] D. A. Rajon, D. W. Jokisch, P. W. Patton, A. P. Shah, C. J. Watchman, and W. E. Bolch, "Voxel effects within digital images of trabecular bone and their consequences on chord-length distribution measurements," *Physics in Medicine and Biology*, vol. 47, p. 1741, 2002.
- [177] C. Shangli, H. Junmin, and L. Zhongwei, "Medical image of PET/CT weighted fusion based on wavelet transform," in *Bioinformatics and Biomedical Engineering, 2008. ICBBE 2008. The 2nd International Conference on*, 2008, pp. 2523-2525.
- [178] R. L. Wahl, L. E. Quint, R. L. Greenough, C. R. Meyer, R. I. White, and M. B. Orringer, "Staging of mediastinal non-small cell lung cancer with FDG PET, CT, and fusion images: preliminary prospective evaluation," *Radiology*, vol. 191, pp. 371-377, 1994.
- [179] R. Bar-Shalom, N. Yefremov, L. Guralnik, D. Gaitini, A. Frenkel, A. Kuten, H. Altman, Z. Keidar, and O. Israel, "Clinical performance of PET/CT in evaluation of cancer: additional value for diagnostic imaging and patient management," *Journal of nuclear medicine*, vol. 44, pp. 1200-1209, 2003.
- [180] B. Hentschel, W. Oehler, D. Strauß, A. Ulrich, and A. Malich, "Definition of the CTV prostate in CT and MRI by using CT-MRI image fusion in IMRT planning for prostate cancer," *Strahlentherapie und Onkologie*, vol. 187, pp. 183-190, 2011.
- [181] G. Sannazzari, R. Ragona, M. R. Redda, F. Giglioli, G. Isolato, and A. Guarneri, "CT-MRI image fusion for delineation of volumes in three-dimensional conformal radiation therapy in the treatment of localized prostate cancer," *British journal of radiology*, vol. 75, pp. 603-607, 2002.
- [182] Y. Miyabe, Y. Narita, T. Mizowaki, Y. Matsuo, K. Takayama, K. Takahashi, S. Kaneko, N. Kawada, A. Maruhashi, and M. Hiraoka, "New algorithm to simulate organ movement and deformation for four-dimensional dose calculation based on a three-dimensional CT and fluoroscopy of the thorax," *Medical physics*, vol. 36, p. 4328, 2009.
- [183] L. Wagner, "Radiation injury is a potentially serious complication to fluoroscopically-guided complex interventions," *Biomed Imaging Interv J*, vol. 3, p. e22, 2007.
- [184] T. Guerrero, G. Zhang, T.-C. Huang, and K.-P. Lin, "Intrathoracic tumour motion estimation from CT imaging using the 3D optical flow method," *Physics in Medicine and Biology*, vol. 49, p. 4147, 2004.

- [185] D. Sarrut, V. Boldea, S. Miguet, and C. Ginestet, "Simulation of four-dimensional CT images from deformable registration between inhale and exhale breath-hold CT scans," *Medical physics*, vol. 33, p. 605, 2006.
- [186] M. R. Kaus, T. Netsch, S. Kabus, V. Pekar, T. McNutt, and B. Fischer, "Estimation of organ motion from 4D CT for 4D radiation therapy planning of lung cancer," in *Medical Image Computing and Computer-Assisted Intervention-MICCAI 2004*, ed: Springer, 2004, pp. 1017-1024.
- [187] V. Boldea, G. C. Sharp, S. B. Jiang, and D. Sarrut, "4D-CT lung motion estimation with deformable registration: quantification of motion nonlinearity and hysteresis," *Medical physics*, vol. 35, p. 1008, 2008.
- [188] D. Yang, W. Lu, D. A. Low, J. O. Deasy, A. J. Hope, and I. El Naqa, "4D-CT motion estimation using deformable image registration and 5D respiratory motion modeling," *Medical physics*, vol. 35, p. 4577, 2008.
- [189] H. Zhong, J. Kim, H. Li, T. Nurushev, B. Movsas, and I. J. Chetty, "A finite element method to correct deformable image registration errors in low-contrast regions," *Physics in medicine and biology*, vol. 57, p. 3499, 2012.
- [190] J. Escolar and A. Escolar, "Lung hysteresis: a morphological view," *Histology and histopathology*, vol. 19, p. 159, 2004.
- [191] T. Klinder, C. Lorenz, J. von Berg, S. Renisch, T. Blaffert, and J. Ostermann, "4DCT image-based lung motion field extraction and analysis," in *Proc. SPIE*, 2008, p. 69141L.
- [192] P.-F. Villard, M. Beuve, B. Shariat, V. Baudet, and F. Jaillet, "Simulation of lung behaviour with finite elements: Influence of bio-mechanical parameters," in *Medical Information Visualisation-Biomedical Visualisation, 2005.(MediVis 2005). Proceedings. Third International Conference on*, 2005, pp. 9-14.
- [193] A. Al-Mayah, J. Moseley, and K. Brock, "Contact surface and material nonlinearity modeling of human lungs," *Physics in medicine and biology*, vol. 53, p. 305, 2008.
- [194] R. Werner, J. Ehrhardt, R. Schmidt, and H. Handels, "Patient-specific finite element modeling of respiratory lung motion using 4D CT image data," *Medical physics*, vol. 36, p. 1500, 2009.
- [195] P. J. Besl and N. D. McKay, "Method for registration of 3-D shapes," in *Robotics-DL tentative*, 1992, pp. 586-606.
- [196] J. Meek, "A brief history of the beginning of the finite element method," *International journal for numerical methods in engineering*, vol. 39, pp. 3761-3774, 1996.
- [197] D. L. Logan, *A first course in the finite element method*: Cengage Learning, 2007.
- [198] S. S. Rao, *The finite element method in engineering*: Butterworth-heinemann, 2005.
- [199] J. T. Oden, *Mechanics of elastic structures*: McGraw-Hill, 1967.
- [200] S. C. Chapra and R. Canale, *Numerical methods for engineers*: McGraw-Hill, Inc., 2005.
- [201] P. Cignoni. *MeshLab*. Available: <http://meshlab.sourceforge.net/>
- [202] Q. Fang and D. A. Boas, "Tetrahedral mesh generation from volumetric binary and grayscale images," in *Biomedical Imaging: From Nano to Macro, 2009. ISBI'09. IEEE International Symposium on*, 2009, pp. 1142-1145.

- [203] M. Mooney, "A theory of large elastic deformation," *Journal of applied physics*, vol. 11, pp. 582-592, 1940.
- [204] J. B. West and F. L. Matthews, "Stresses, strains, and surface pressures in the lung caused by its weight," *J Appl Physiol*, vol. 32, pp. 332-45, Mar 1972.
- [205] S.-K. Teo, Y. Yang, E. Van Reeth, S. He, P. Chua, and C. L. Poh, "Tracking of tumor motion in lung cancer using patient specific finite element modeling and 4d-MRI image data," in *Biomedical Engineering (BioMed 2013)*, 2013.